THE UNIVERSITY *of* EDINBURGH

The Use of Chelating Ligands in the Synthesis of Paramagnetic Frameworks

Priyanka Comar

A Thesis Submitted for the degree of Doctor of Philosophy

School of Chemistry

Faculty of Science and Engineering

University of Edinburgh

Edinburgh- August 2016

Lay Summary

This thesis explores the properties of paramagnetic frameworks, which are metal ions with unpaired electrons linked together by bridging species (known as ligands). Due to the unpaired electrons present, these materials exhibit magnetic properties. In order to study the nature of these magnetic properties, studies have been undertaken to determine which structural parameters are the most important, specifically the nature of the ligand present. A range of frameworks of different sizes have been synthesised, ranging from those containing just two metal ions, to those that form cages and even larger structures known as metal-organic frameworks (MOFs). The latter, not only possesses properties relevant to magnetism but also exhibits features that are interesting to study under an applied high pressure. A total of 14 new frameworks have been synthesised and discussed in this thesis to give an in-depth perspective on what determines their structural and magnetic properties.

Abstract

Chapter 1 of this thesis contains an extensive literature review of magneto-structural correlations (MSCs) of a range of transition metal dimers. Different structural parameters are considered and a critical assessment is given of the principal factors influencing the exchange interactions in each case. Following this, two different synthetic strategies for the synthesis of polymetallic systems are compared and contrasted. Their role in the formation of paramagnetic frameworks is also considered.

Chapter 2 describes the synthesis of a family of Mn^{III} dimers and highlights the importance of chelating ligands in their formation and magnetic properties. A family of Mn^{III} dimers of general formula of $[Mn^{III}_2(R\text{-}sao)_2(dpa)_2](ClO_4)_2$ (**1**-**5**) has been synthesised using derivatised phenolic oximes ($R\text{-}saoH_2$, where R=H, Me, Et, Ph) in combination with di-(2-picolyl)-amine (dpa). The structures reveal a double-oxime bridged $[Mn^{III}(NO)]_2$ magnetic core in which the Jahn-Teller axes lie perpendicular to the bridging plane, in contrast to two previously reported family members (**6** and **7**). The switch in the orientation of the Jahn-Teller axes is enforced through the use of the chelating ligand which is present in **1**-**5** and absent in **6**-**7**. Dc magnetic susceptibility measurements reveal that the exchange interactions between the Mn^{III} metal centres in **1**-**5** are antiferromagnetic in contrast to that observed for **6** and **7** which are ferromagnetic. DFT calculations have also been undertaken in order to confirm these findings.

Chapter 3 describes the synthesis of a family of novel cages from the metalloligand $[Fe^{III}L_3]$, where HL = 1-(4-pyridyl)butane-1,3-dione and metal salts $CuBr_2$, $Cu(NO_3)_2$, $NiCl_2$, $CoCl_2$ $Co(SCN)_2$, $ZnBr_2$ and $Pd(OTf)_2$ (where OTf = triflate anion). The flexibility in the design of these structures offers huge potential to tune their physical properties as the constituent parts of the cage can be altered without any change to the structure. Due to the large size of the internal cavity, it is possible that the cage could play host to different species, such as magnetic guests, which

would then exert control over the exchange interaction between the metal ions in the host framework and between the host and guest(s).

Chapter 4 presents the synthesis and crystallographic studies of two novel metal organic framework (MOF) $[Cu^{II}L_2]_n$ and HL = 1-(4-pyridyl)butane-1,3-dione. An in-depth high-pressure crystallographic study of structure shows that the framework undergoes a single-crystal phase transition as well as a switching of the orientation of the Jahn-Teller axis, which is dependent on the hydrostatic media and also the presence of negative linear compressibility (NLC) behaviour.

Acknowledgements

I would firstly like to thank Euan for allowing me to complete my PhD in his group and for his continued support through the past three years. You have given me the opportunity to travel to some fantastic places for conferences and collaborative work. Thank you for treating the group every year to fantastic Christmas lunches and for trying to, at least, increase my alcohol tolerance!

Thank you also to the past and current members of the Brechin (and Inglis) Group: Ross, Sergio, Julia, Maria, Anders, Helen, Hector and Robbie. Of course a special thank you to Jamie for being there and believing in me from day one and also for all the good times during the past three years.

A special thank you to my parents and my sister for their faith and encouragement. Mum and papa, you have made great sacrifices for both Eisha and I. I could not be more grateful for this. Eisha, thank you for understanding my journey more than anyone. Ranjan, thank you for your constant positivity and motivation and for being a great listener. Mama- losing you last year was very hard, but you will be forever in my heart and I hope I have made you proud. Another special thank you to Rebecca, Brianna and Shamani, for the great memories and constant support. Claire, Max, Fern, Emily and Amy, thank you for helping make Edinburgh home and for your support with my thesis.

I would also like to thank Dr Stephen Moggach and Charlie McMonagle for their time put into the work in Chapter 4. In addition, thank you to Dr Gary Nichol, and Dr Mateusz Pitak for solving the crystal structures that are in this thesis. Thank you to Dr Gopalan Rajaraman for the theoretical modelling in chapter 2 and also to Dr Stergios Pilikgos for the fitting of some of the magnetic data presented. I would also like to extend a thank you to Prof. Eric McInnes, for not only the EPR measurements in this thesis, but for being my inspiration to pursue a PhD!

Declaration

I hereby declare that except where specific reference is made to other sources, the work contained in this thesis is the original work of the author. It has been composed by the candidate and has not been submitted, in whole or in part, for any other degree, diploma, or other qualification.

Priyanka Comar

Format of the Thesis

Each chapter of this thesis, with the exception of Chapter 1, is made up of my contributions to peer-reviewed papers, which have already been published or submitted for publication. To fulfil the requirements of the University of Edinburgh regarding the preparation and submission of a thesis for the degree of PhD, they have been reformatted accordingly.

Chapter 2

- P. Comar, T. Rajeshkumar, G. S. Nichol, M. B. Pitak, S. J. Coles, G. Rajaraman and E. K. Brechin, *Dalton Trans*., 2015, **44**, 19805.

Chapter 3

- P. Comar, S. Sanz, S. Piligkos, E. L. J. McInnes, E. K. Brechin, *Chem. Sci., Submitted Manuscript.*
- S. Sanz, H. M. O'Connor, V. Marti-Cerntelles, P. Comar, S. J. Coles, G. S. Nichol, E. Palacios, M. Evangelisti, A. Baldansuren, N. F. Chilton, E.J L. Mcinnes, H. Weihe, S. Piligkos, P. L. Lusby and E. K. Brechin, *Submitted Manuscript.*

Chapter 4

- C. McMonagle, P. Comar, G. S. Nichol, D. Allan, E. K. Brechin and S. A. Moggach, *Submitted Manuscript*.

Work carried out by other people:

DFT calculations: Dr Gopalan Rajaraman

Magnetic simulations in Chapter 3: Dr Stergios Piligkos

EPR measurements and simulations: Prof. Eric McInnes and Dr Nicholas Chilton

Publications

1. E. Houton, P. Comar, M. B. Pitak, S. J. Coles, A. G. Ryder, S. Piligkos, E. K. Brechin and L. F. Jones, *RSC Adv.*, 2016.
2. P. Comar, T. Rajeshkumar, G. S. Nichol, M. B. Pitak, S. J. Coles, G. Rajaraman and E. K. Brechin, *Dalton Trans*., 2015, **44**, 19805.
3. C. McDonald, D. W. Williams, P. Comar, S. J. Coles, T. D. Keene, M. B. Pitak, E. K. Brechin, L. F. Jones, *Dalton Trans*., 2015, **44**, 13359.
4. R. J. Blagg, L. Ungur, F. Tuna, J. Speak, P. Comar, D. Collison, W. Wernsdorfer, E. J. L. McInnes, L. F. Chibotaru and R. E. P. Winpenny, *Nature Chemistry*, 2013, **5**, 673.

Conferences Attended

2013 RSC Macrocyclic and Supramolecular Chemistry Meeting, Glasgow University (UK).

2014 14th International Conference on Molecule Based Magnets, Saint Petersburg, Russian Federation. Poster presented.

RSC Dalton Discussion 14/ Advancing the Chemistry of the f-elements, University of Edinburgh (UK).

9th International Anglo German Conference on Inorganic Chemistry, University of Edinburgh (UK). Poster presented.

Universities of Scotland Inorganic Conference, Glasgow University (UK). Poster presented.

2015 5th European Conference of Molecular Magnetism, Zaragoza, Spain. Poster presented.

2016 University of Edinburgh Joseph Black Conference, Edinburgh (UK). Oral Presentation.

Contents

List of Complexes

Complex	Chapter	Complex Number
$[Mn^{III}_2(Et\text{-}sao)_2(dpa)_2](ClO_4)_2$	2	1
$[Mn^{III}_2(Me\text{-}sao)_2(dpa)_2](ClO_4)_2$	2	2
$[Mn^{III}_2(Me_2\text{-}sao)_2(dpa)_2](ClO_4)_2$	2	3
$[Mn^{III}_2(sao)_2(dpa)_2](ClO_4)_2$	2	4
$[Mn^{III}_2(Ph\text{-}sao)_2(dpa)_2](ClO_4)_2$	2	5
$[Fe^{III}_8Cu^{II}_6L_{24}Br_6]Br_6$	3	1
$[Fe^{III}_8Cu^{II}_6L_{24}](NO_3)_{12}$	3	2
$[Fe^{III}_8Ni^{II}_6L_{24}(SCN)_{11}Cl]$	3	3
$[Fe^{III}_8Co^{II}_6L_{24}(SCN)_{10}(H_2O)_2](SCN)_2$	3	4
$[Fe_2Co_3L_6Cl_6]$	3	5
$[Fe_2Zn_3L_6Br_6]$	3	6
bis[1-(4-pyridyl)butane-1,3-dione]copper(II) (ambient pressure)	4	CuPyr-1
bis[1-(4-pyridyl)butane-1,3-dione]copper(II) (high pressure)	4	Cu-Pyr-II

Chapter 1
Introduction

In coordination chemistry the role of chelating ligands relies heavily on the donor atoms present and the nature of the metal centres involved in the resulting framework. This can be extended to the influence the ligands have on the magnetic interactions between the paramagnetic metals present. A plethora of research has been directed towards studying the relationship between structure and magnetic properties in small systems containing just a few metal ions. Fewer studies have been published on large cages containing multiple paramagnetic centres, due to the increasing structural complexity and the typically low symmetry of such species, which can hinder both qualitative and quantitative analyses. One way to address these challenges qualitatively, is to assemble large cages in a modular fashion from small, pre-designed building blocks, often referred to as secondary building units (SBUs). The structural integrity of the SBU is conserved in full or in part, such that the magnetic behaviour is transferred to the cage. This thesis examines the use of chelating ligands to build such complexes, and examines how different ligand topologies and flexibilities affect cluster formation. Specifically it presents the syntheses, structures and magnetic behaviour of a variety of clusters of paramagnetic 3D metal ions ranging from small dimeric homometallic structures to large poly- and heterometallic cages, the latter of which may find application beyond magnetism. In each case a magneto-structural relationship is discussed.

1.1 Magneto-Structural Correlations

The term magneto-structural correlation (MSC), referring to the relationship between magnetism and structure as determined by parameters such as bond distances and bond angles, is best studied in simple molecules, at least initially, since this reduces the number of variable parameters contributing to the magnetic exchange interaction.[1] Fundamentally, the nature of the exchange interactions between more than one paramagnetic centre can be quantified by the parameter *J*. In the case of two metals, where the interacting spins are S_1 and S_2, a spin Hamiltonian $\widehat{H} = -2J_{1,2}\widehat{S_1}.\widehat{S_2}$ can be constructed.[2] Using this definition, when *J* < 0, the exchange interaction is antiferromagnetic; where the respective spins are

aligned antiparallel to each other. When $J > 0$ the exchange is ferromagnetic and the spins are aligned parallel to one another.

As the nuclearity of a complex increases the number of independent parameters also increases, often over-parameterizing any potential quantitative model.[3] This can be overcome if the large cluster is of high symmetry with the asymmetric unit containing a small number of metal ions, or where the cage is comprised of a series of identical building blocks. By making and studying these SBUs, it is possible to project exchange interactions onto larger species allowing a more in-depth understanding of the magnetic behaviour than would otherwise be possible. Hence, the most renowned and ground-breaking magneto-structural studies of 3*d* complexes that are pertinent to the new complexes presented in Chapters 2-4 have been summarised in this chapter.

Cu^{II} Dimers

The relationship between structure and magnetism in discrete molecules first became a focus of investigation with the work conducted by Hatfield and Hodgson on a family of bis-(μ-hydroxo) Cu^{II} dimers.[4,5] The primary factor in determining the nature of the exchange interaction is the Cu-O-Cu angle in which the complex exhibits ferromagnetic exchange below 96°. This is accounted for by the orthogonality of the magnetic orbitals on Cu^{II} and the 2*p* orbitals on the O-atoms when the Cu-O-Cu angle approaches 90°. In this scenario Hund's rule dictates that the two electrons in the oxygen p_x orbital must be aligned parallel to each other, hence resulting in a ferromagnetic interaction. When the Cu-O-Cu angle is above 96° the exchange becomes antiferromagnetic as there is now greater overlap between the O-atom p_z orbital and the unpaired Cu^{II} electron.[4] This is summarised in Figure 1.1.

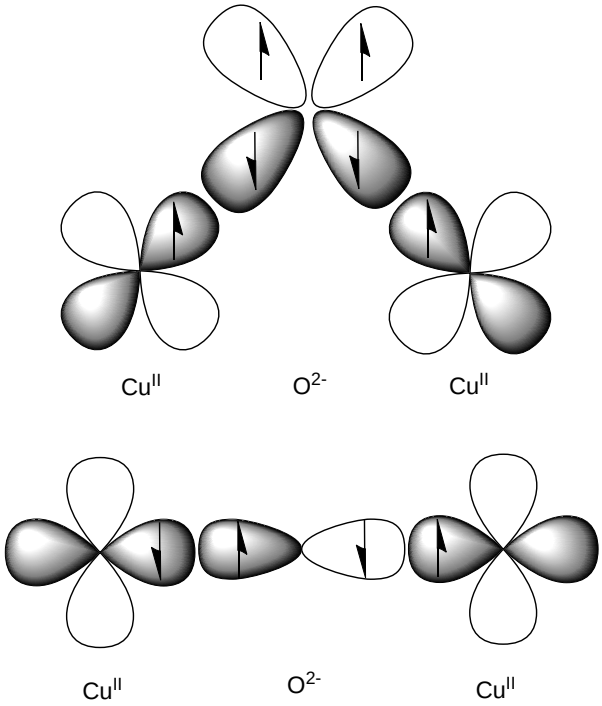

Figure 1.1. Schematic representing ferromagnetic and antiferromagnetic exchange interactions in Cu-O-Cu dimers.

Cr^{III} Dimers

Examples of ferromagnetically coupled Cr^{III} dimers are scarce in the literature. To date, there are three examples; dihydroxo- (J = -5.17 cm^{-1}),[6] malonato- (J = -2.16 cm^{-1})[7] and aqua-bridged (J = -10.0 cm^{-1}) complexes[8] (where $H = JS_A \cdot g(S_{Az} + S_{Bz})\mu_B B$). Two different models have been proposed to explain the nature and magnitude of the exchange interaction between the Cr^{III} centres in the aforementioned molecules and also the extensive literature of antiferromagnetically coupled systems. The first to be proposed was the Glerup-Hodgson-Pedersen (GHP) model (an extension of the Angular Overlap Model).[10]

This has been reconfirmed and expanded on by broken-symmetry density functional theory (DFT) calculations.[6,9] The two most influential factors are the Cr-O-Cr angle (ϕ) and the out of plane hydrogen angle (Θ), as shown in Figure 1.2. As Θ increases between 0 and 90°, the π overlap between the d orbitals on the metal centres and the lone pairs of electrons on the O atoms decreases, therefore resulting in a higher and more dominating contribution of J_F. Upon varying ϕ, it can

be seen up to 97.5°, antiferromagnetic exchange is prominent. However at 97.5° the exchange switches to ferromagnetic, which is maintained until 102°, at which the exchange decreases again and switches back to antiferromagnetic at 107°.

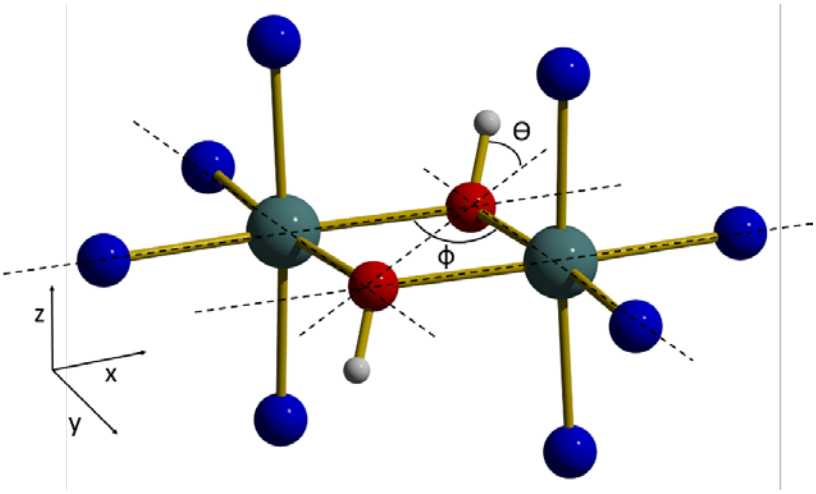

Figure 1.2. Coordinate system and defined angles in Cr^{III} dimers in the above described system.

When the DFT model is specifically applied to a complex, such as $(Ph_4P)_4[(SCN)_4\text{-}Cr(OH)_2Cr(NCS)_4.2CH_3CN$, referred to as 'diol' due to its bridging group, it predicts the nature of the exchange interaction correctly to be ferromagnetic however the difference in magnitude is fairly significant where J_{EXP} = -5.15 cm^{-1} and J_{DFT} = -12.9 cm^{-1}.[10] However, the GHP model wrongly predicts an antiferromagnetic exchange interaction, where J_{GHP} = 4.34 cm^{-1}. Even with variations of Θ, the GHP model does not correctly match J_{EXP}.

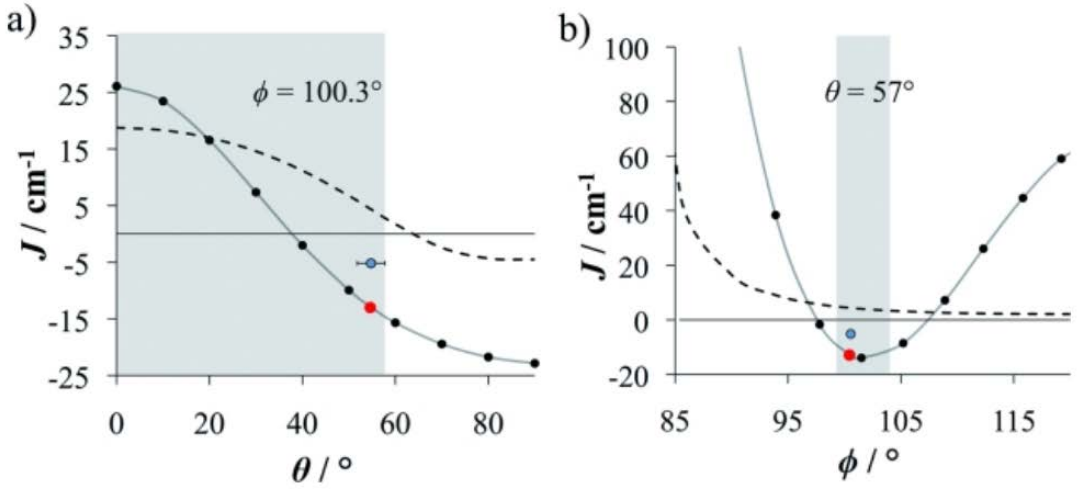

Figure 1.3. DFT studies performed to show the effect of varying a) Θ and b) ϕ. The blue dot represents J_{exp}, the dashed line shows the trend by GHP model and the grey areas represent the experimentally accessible values for Θ and ϕ.[9]

Mn^{III} Dimers

There are several different families of Mn^{III} dimers that have been studied.[11,12] In 2012, Brechin and co-workers reported a family of asymmetrically oximato/ oxo-bridged Mn^{III} dimers.[11] Using different substituents on the derivatised phenolic oxime, the Mn-N-O-Mn torsion angle was deliberately changed from 8° to 13°. The experimental study showed that as the torsion angle increases the strength of the antiferromagnetic coupling decreased and eventually switched to ferromagnetic at 13.55°. These findings were confirmed through computational studies, which showed that upon a larger torsion angle the $d_{yz}|\pi^*|d_{yz}$ interaction diminishes.[11]

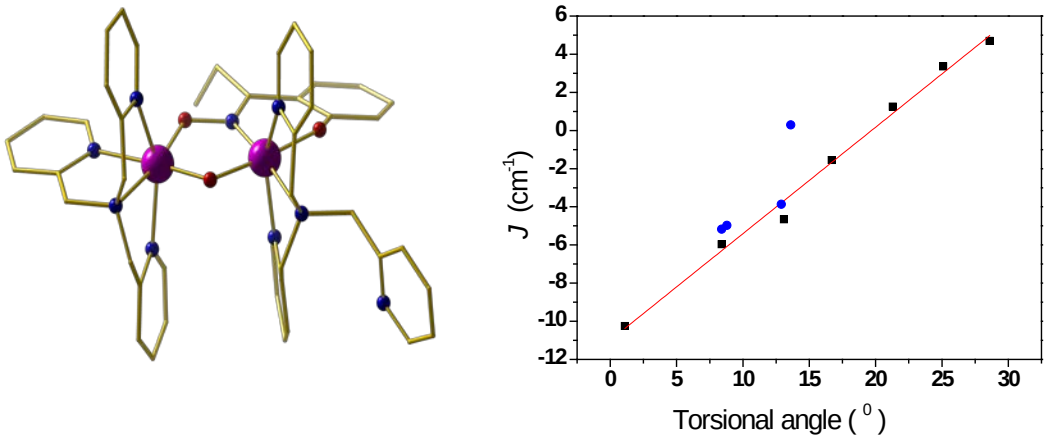

Figure 1.4. Left: Molecular structure of $[Mn^{III}_2O(Et\text{-}sao)(tpa)_2]$. Mn = pink, N = blue and O = red. H atoms removed for clarity. Right: MSC established by varying the Mn-N-O-Mn torsion angle of one member of the family of the dimers discussed above. The blue circles represent the J_{exp} for all members of the series.

Also in 2012, Jones and co-workers conducted an in-depth study on a family of bis-μ-alkoxide-bridged Mn^{III} dimers of general formula $[Mn^{III}_2(\mu\text{-}OR)_2(biphen)_2(ROH)_x(L)_y]$ where R = Me, Et; H_2biphen= 2,2'-biphenol and L = N-donor ligand.[12] The structures were categorised into three different groups according to the orientation of the Jahn-Teller (JT) axis. In type I the JT axes are parallel to each other but perpendicular to the bridging plane. Here all compounds exhibit weak antiferromagnetic exchange accounted for by the strong overlap of SOMOs and lack of $d_{x^2-y^2}$ interaction diminishing the ferromagnetic contribution. Type II, where the JT axes are parallel to each other and also parallel to the bridging plane, exhibit exchange interactions lying on the border between antiferromagnetic and ferromagnetic. In this case there are interactions between d_{yz}-d_{yz}, d_{xz}-d_{yz}, d_{yz}-d_{xz} and d_{xy}-d_{xy} orbitals and also significant cross-interactions. For type III the JT axes are perpendicular to each other, with one lying along the bridging plane and one perpendicular to the bridging plane. In this scenario weak ferromagnetic exchange was observed due to strong cross interactions of $d_{x^2-y^2}$ orbitals.[12]

Figure 1.5 below displays the experimental variation of J with the dihedral angle between the JT axes in the three different types of dimers. This parameter shows a large separation between the three different types of dimers which cannot

be seen through any other structural parameter, such as bond distances. The dihedral angles range from <10° for type I, 152-180° for type III and 71.9-117.1° for type II.

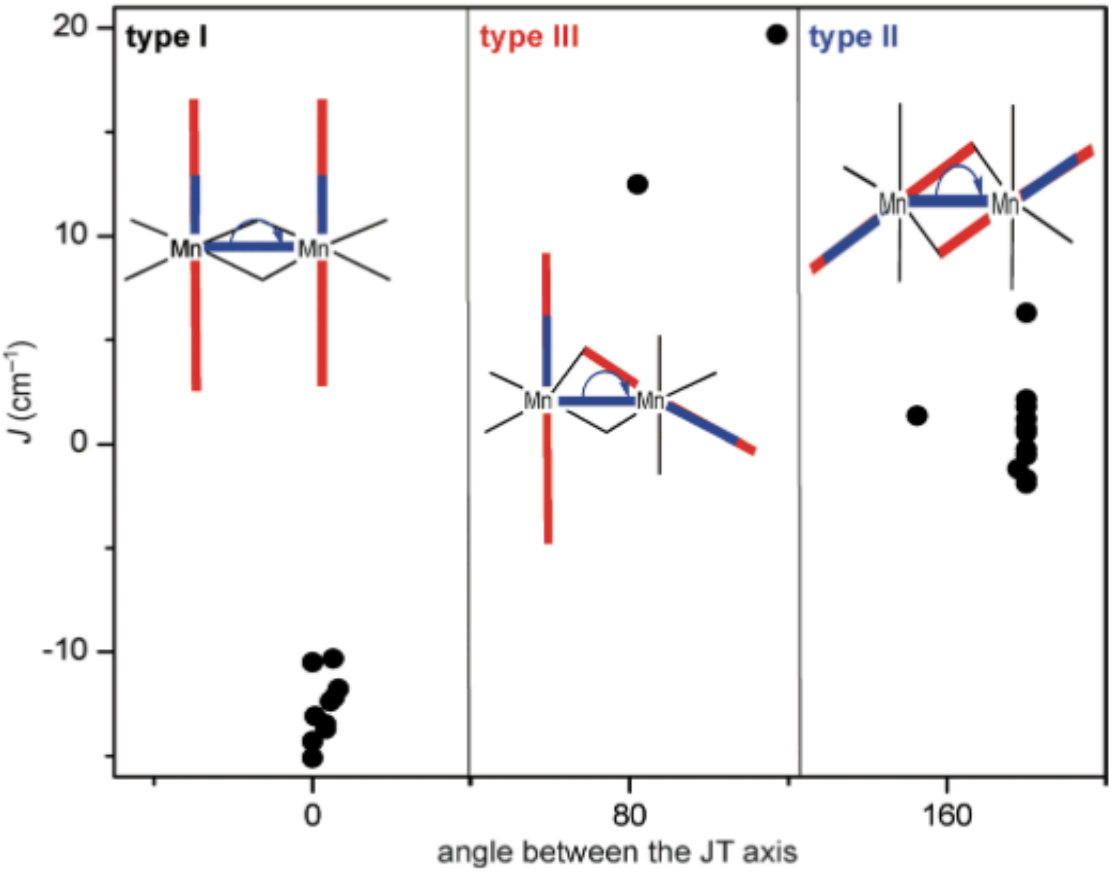

Figure 1.5. A plot of *J vs* angle between the JT axes in types I-III of Mn dimers discussed above.

Fe^{III} Dimers

The interpretation of magneto-structural data of Fe^{III} complexes can be a difficult task due to the five singly occupied *d* orbitals present in high-spin, octahedral Fe^{III} ions, and the involvement of ten magnetic orbitals in the exchange.[13] During the 1990s several MSCs were developed for alkoxide-bridged Fe^{III}-O(R)-Fe^{III} systems.[14,15] The first to be published was in 1991 by Gorun and Lippard, based on doubly and triply bridged Fe^{III}_2 complexes, with O^{2-}, OR^-, OPH^-,

OH^- and O_2X^-.[14] Results of their studies suggested that *J* is directly related to the parameter *P*; half of the length of the shortest Fe-O-Fe bridge, with *J* being quantified by the following equation:

Equation 1.1. The relationship between *J* and *P*.

$$\boldsymbol{J\ (cm^{-1}) = \ Ae^{BP}}$$

Where A = -8.763x10^{11} cm^{-1} and B = -12.663 $Å^{-1}$.[14] The exponential form of the equation represents the overlap between two *s* orbitals which reportedly can give the magnitude of the exchange coupling. The model also states that upon the presence of multiple bridges such as carboxylates, the average Fe-O bond lengths from the carboxylate bridges are used. At the time that the study was conducted it was also applied to trinuclear complexes, for which it appeared to be valid. However, since then this relationship proved to be of limited applicability since several complexes displayed experimental *J* values of different magnitude and sign to that predicted. For example, the complex $[Fe_3L_2](ClO_4)_3$ (where L = tris(6-hydroxymethyl-2-pyridylmethyl)amine), possessing alkoxide bridges, exhibits weak antiferromagnetic exchange not supported by DFT studies.[16] The strength of this MSC is also diminished by the deviations between experimental and calculated *J* values for the OH^-, OR^- and OPh^- bridged dimers. This can be exemplified in Figure 1.6 below; showing the MSC proposed by Gorun and Lippard and how hydroxy-, alkoxo- and phenoxo- bridged Fe dimers fit into this trend.

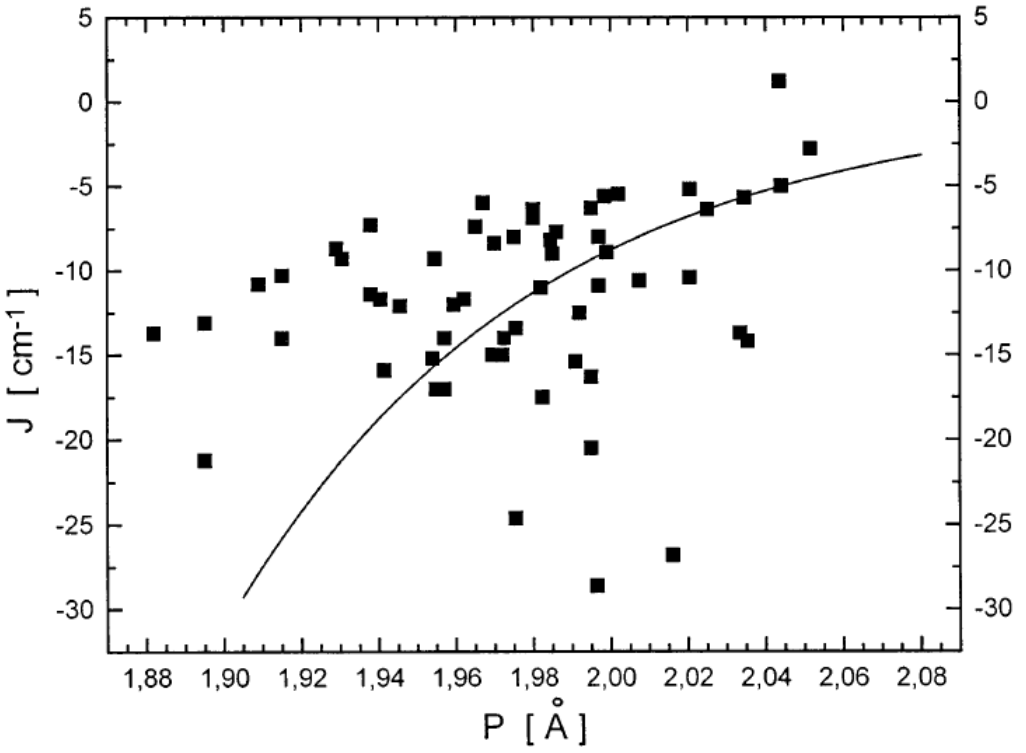

Figure 1.6. Plot of *J* vs *P* for hydroxy-, alkoxo- and phenoxo- bridged dimers and their correlation with the Gorun and Lippard model. The black line signifies the proposed MSC.[13]

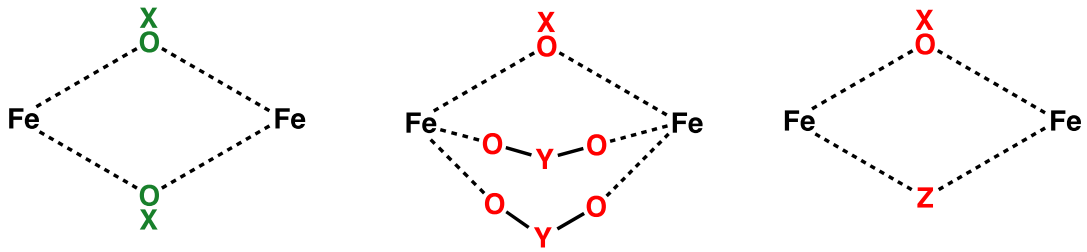

Figure 1.7. Different bridging moieties in Fe^{III} dimers.

In 1997, Weihe and Güdel further developed the MSC of singly oxo-bridged, linear and bent Fe^{III} dimers using an angular and radial overlap model, [15] where *J* is expressed in terms of the overlap between the Fe *d* orbitals and the bridging oxide *p* and *s* orbitals. Here, the important structural factors were determined to be the Fe-O-Fe bridging angles and the Fe-O bond distances, as shown in Figure 8. It is assumed that all interactions take place through the bridging O atom and not any other bridge. Upon keeping ϕ constant, it was shown that there is a strong

relationship between *J* and the distance *r*. At 180°, the antiferromagnetic contribution to *J* increases with decreasing value of *r*.

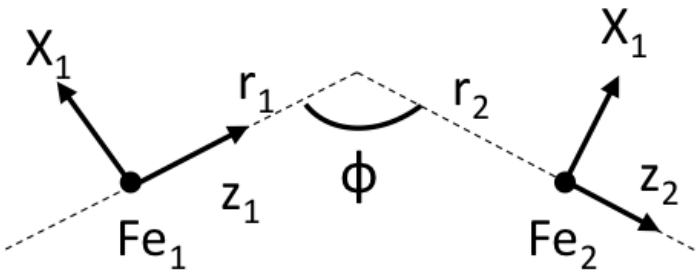

Figure 1.8. Defined angles, distances and axes in Fe dimers, as referenced to in the text.

Further analysis confirms that the shortest Fe-O bond length is a contributing factor to the antiferromagnetic exchange in Fe dimers.[13] This is because as the distance between the bridge and the Fe centre decreases, the overlap of the orbitals increases. Moreover, with the increasing inductive nature of Ph < H < R bonded to the O atom, the electron density on O also increases. This reflects in the correlation between *J* and the Fe-O bond length shown below in Figure 1.9.

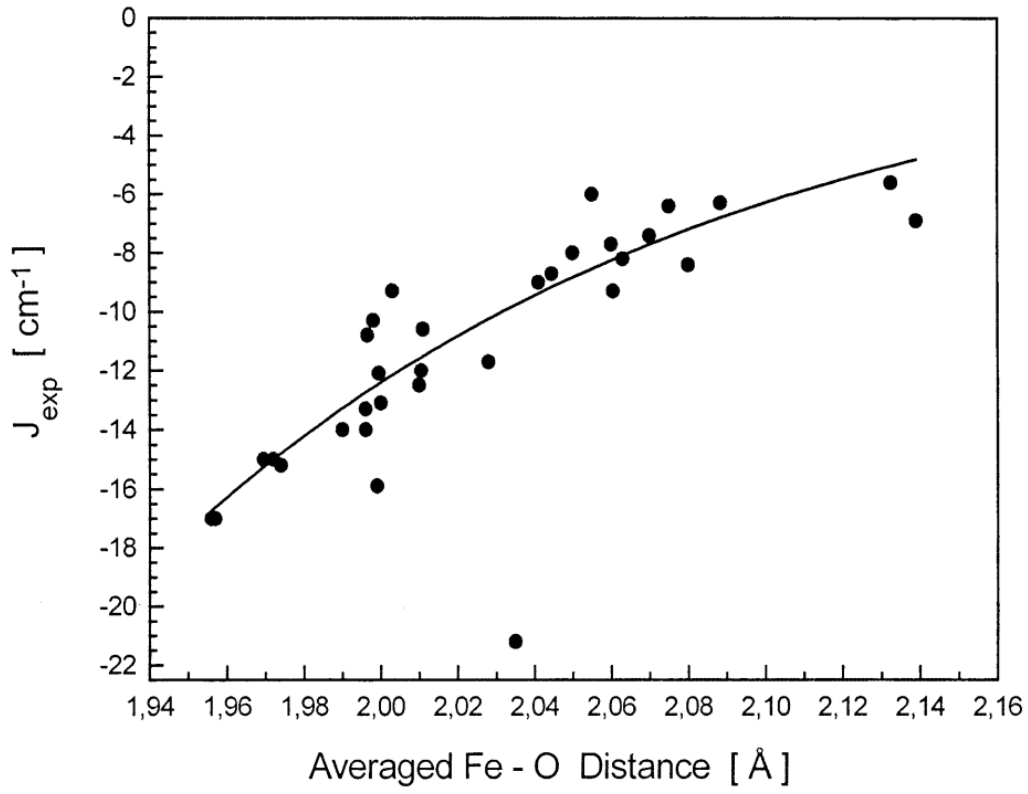

Figure 1.9. Improved MSC for OH^-, OR^- and OPh^- asymmetrical oxygen-bridged Fe^{III} dimers.[13]

1.2 Synthetic strategies to form Polymetallic Complexes

When seeking to build molecules containing multiple paramagnetic metal ions, one can approach the problem from two different perspectives; serendipitous self-assembly – where the outcome of the reaction is to some extent unknown, and rational design – where the reactants are designed to form a targeted and predicted structure. Both methods have been successful in producing a variety of aesthetically pleasing cages possessing interesting magnetic behaviour. In reality of course, this dichotomy between "serendipitous" and "rational" is somewhat illusory, as significant elements of both approaches can be used for the synthesis of libraries of structurally related compounds. However, a brief introduction to both methods will be discussed below.

Rational Design

The rational design approach involves examining several aspects when pre-designing a complex that, in principle, will possess the desired structure. These include the coordination number, the geometry of the complex, the shape/bonding directionality of the ligands and the symmetry in the coordination motif.[17] This technique can prove to be useful in molecular magnetism as it can be possible to predict the number of the exchange interactions present if the target complex is made, and therefore design a structure with desired properties.

The rational design of supramolecular complexes of diamagnetic metals, was initiated by Fujita and co-workers. His most pioneering work includes using molecular panelling as a strategy to form 3-D structures of varying shapes from cages to bowls, tubes and polyhedra. *Cis* protected (en)Pd^{2+} (en = ethylenediamine) building blocks were designed to be ideal systems to exploit the square planar, 90° bond angles to target specific geometries, the most famous example of which is the using 4,4-bipyridine (4,4-bipy) as a bridge to form a molecular square.[18,19] Two dimensional structures, such as these squares or triangles can be used as panels to construct 3-D structures, such as the octahedron shown in Figure 1.10 below. The

basic synthetic strategies for the formation of 2-D and 3-D complexes are also summarised in Figure 1.10:[20]

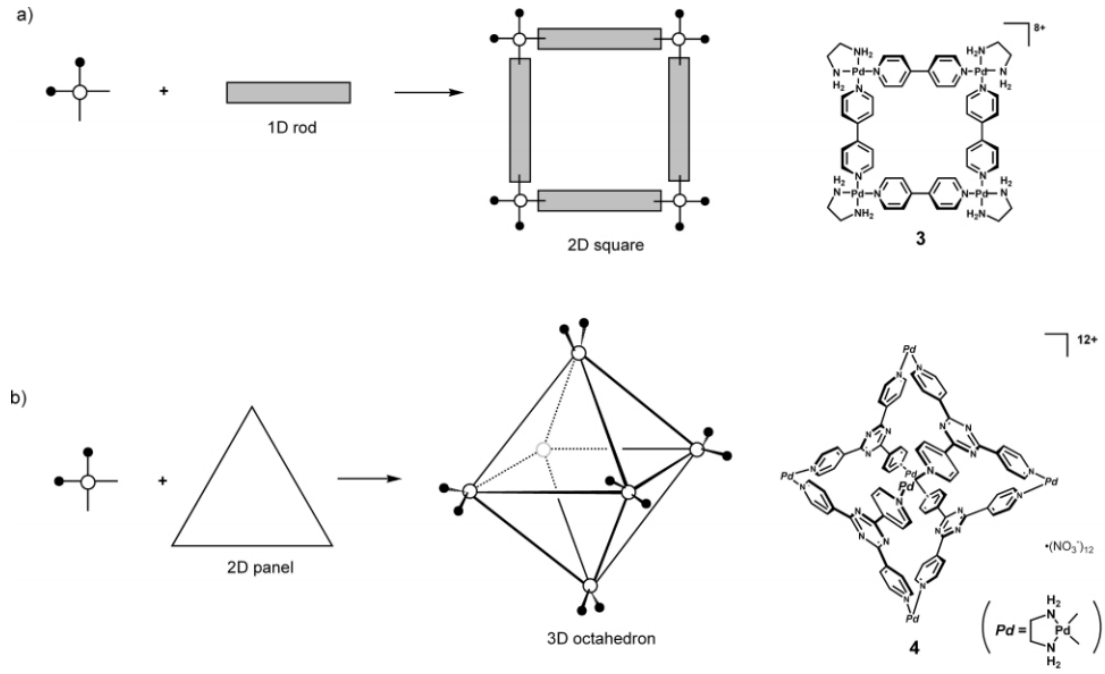

Figure 1.10. Molecular panelling representation of the formation of a) 2D-molecules from 1D-rods and b) 3d- molecules from 2D-panels.[20]

The systematic exploration of rational design approaches over the past several decades has resulted in the predictability of the resulting geometries. Stang and co-workers, suggest that two vital features are required for the self-assembly of three-dimensional structures: the use of complementary building blocks that provide rigidity and defined angles to the product and also the stoichiometric ratio of metal centres to ligands used.[21] The donor units generally possess more than two binding sites at angles varying between 0 and 180° to each other. The acceptor building block, containing metal atoms provide coordination sites at pre-defined and fixed angles. Figure 1.11 below shows how different complementary geometries can form various 3-D structures.

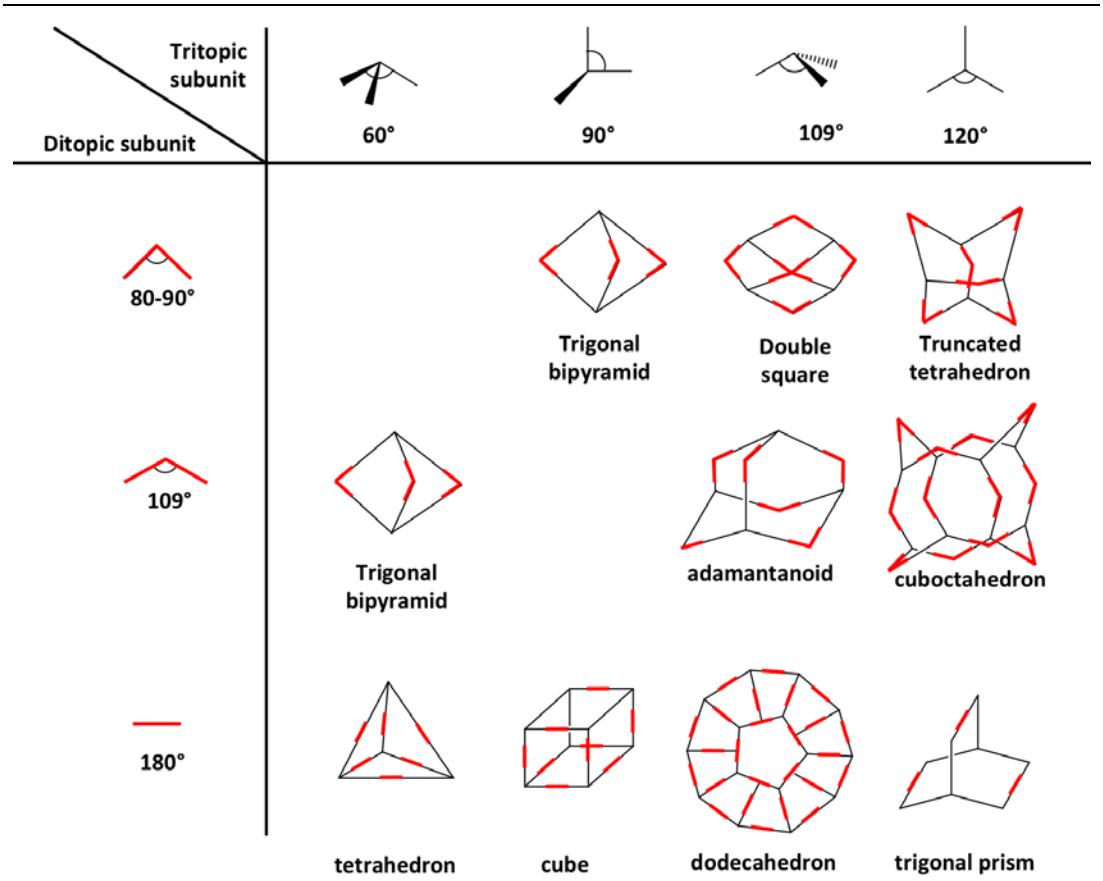

Figure 1.11. Schematic representation of possible geometries formed from complementary ligands.

The choice of ligand can be used as a tool to transform the physical properties of a compound by changing the identity or the number of donor atoms, the flexibility, the symmetry and also the length of the ligand. These factors are paramount in rational synthesis as they can be used to control the dimensionality of the resulting structure and can be used to exploit self-assembly.

Cyanometallates provide a well-established approach to the synthesis of two and three-dimensional frameworks, due to the inertness of the CN^- ligand once coordinated.[22,23] The bridging angles and also the identity of the metal can determine the nature of the exchange interaction through the cyanide bridge due to the overlap of π and σ orbitals of heterometallic complexes. Whilst the incorporation of Cu^{II} or Ni^{II} through coordination to the N atom of CN^- results in ferromagnetic interaction due to the orthogonality of the e_g orbitals (octahedral crystal field), Cr^{II}, Mn^{III}, Mn^{II}, Fe^{II} and Co^{II} all possess unpaired electrons in t_{2g}

orbitals, hence resulting in both antiferromagnetic and ferromagnetic contributions to the exchange. The dominant exchange can be experimentally determined by establishing the number of exchange pathways present.[22]

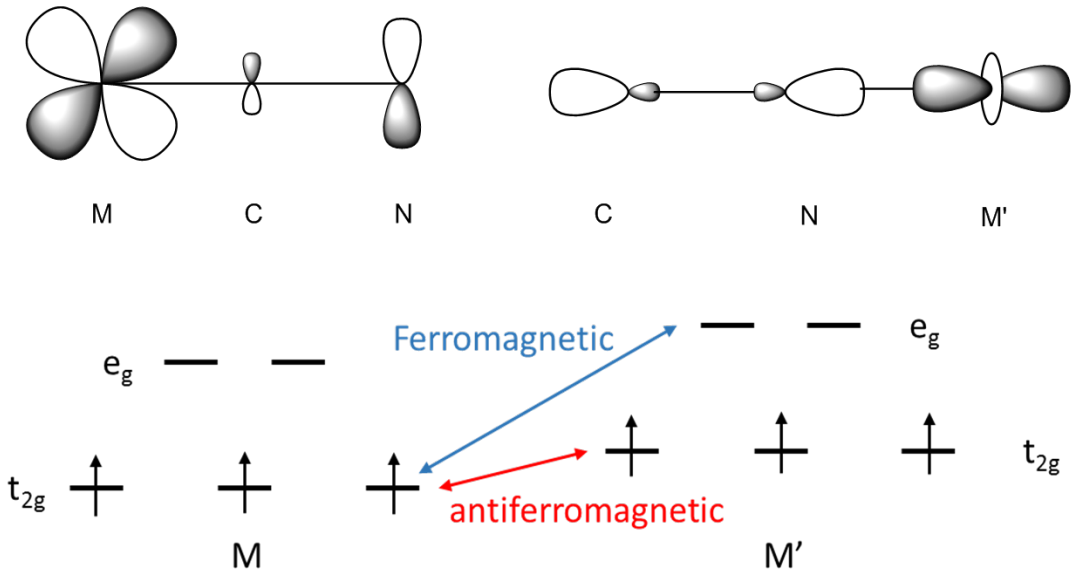

Figure 1.12. Top: Orthogonality of magnetic orbitals contributing to ferromagnetic exchange. Bottom: Contributing ferromagnetic and antiferromagnetic exchange due to orthogonality and overlap of *d* orbitals respectively.

A noteable method taken by Mallah and co-workers and Verdageur and co-workers involves using specific polydentate ligands which would block selected coordination sites and therefore impose a specific geometry on the resulting complex. The chelated complex is required to be stable enough that the ligand cannot be substituted by the N atom of the cyanide bridge. The complex $[Cr^{III}(CN)Ni(tetren))_6](ClO_4)_9$ was formed through the reaction of $K_3[Cr(CN)_6].2H_2O$ and $[Ni(tetren(H_2O)](ClO_4)_2$ (where tetren = tetraethylenepentamine).[24] The latter is coordinated to the pentadentate ligand, therefore leaving a vacant coordination site, which is occupied by water, until reaction with the former, in which then the resulting heptanuclear product is formed where the vacant site is occupied by the N atom of the CN^- ligand.[24]

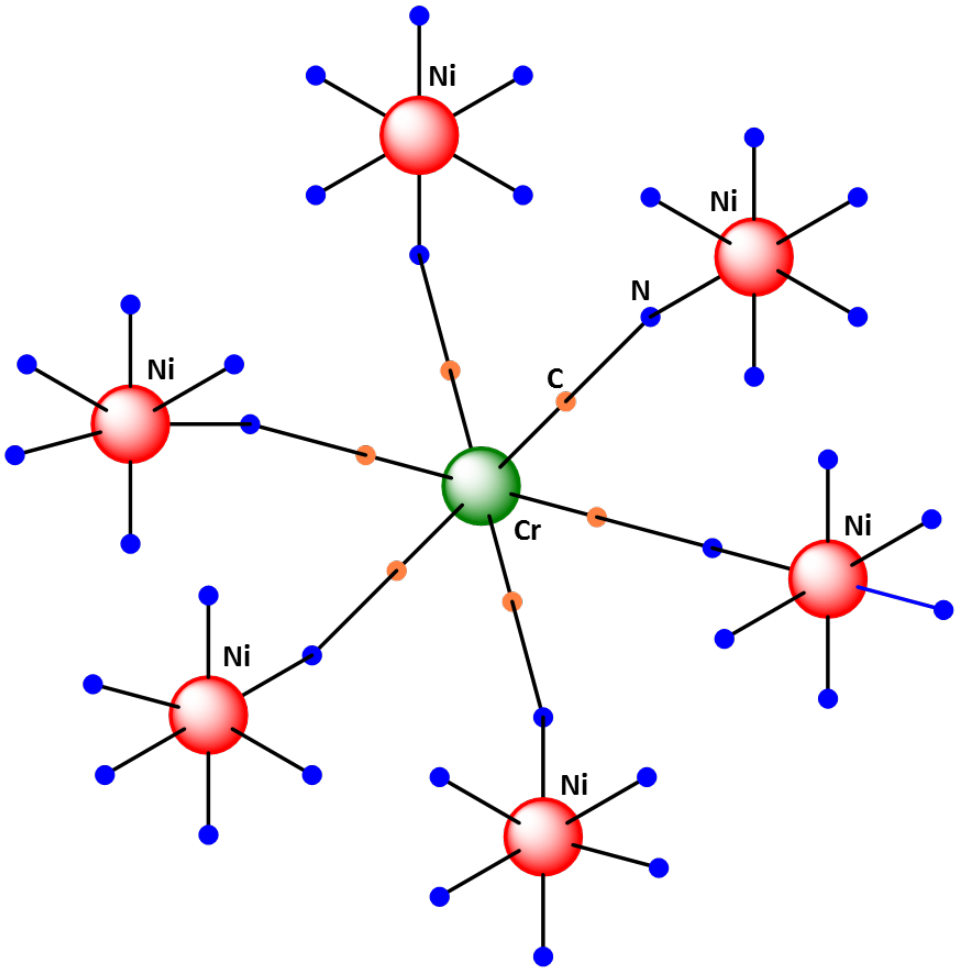

Figure 1.13. Schematic representation of $[Cr^{III}((CN)Ni(tetren))_6](ClO_4)_9$. ClO_4^- ions omitted for clarity.

The same approach was taken with the synthesis of $[Ni(cyclam)]_3[Cr(CN)_6]_2.20H_2O$ (where cyclam = 1,4,8,11-tetrazacyclotetradecane).[25] The complex forms a layered structure in which the *trans* positions on Ni(cyclam) are occupied by the $[Cr(CN)_6]$ precursor, resulting in three uncoordinated CN^- ligands. The structure exhibits ferromagnetic exchange between Ni^{II} and Cr^{III} through the CN^- bridges.[25]

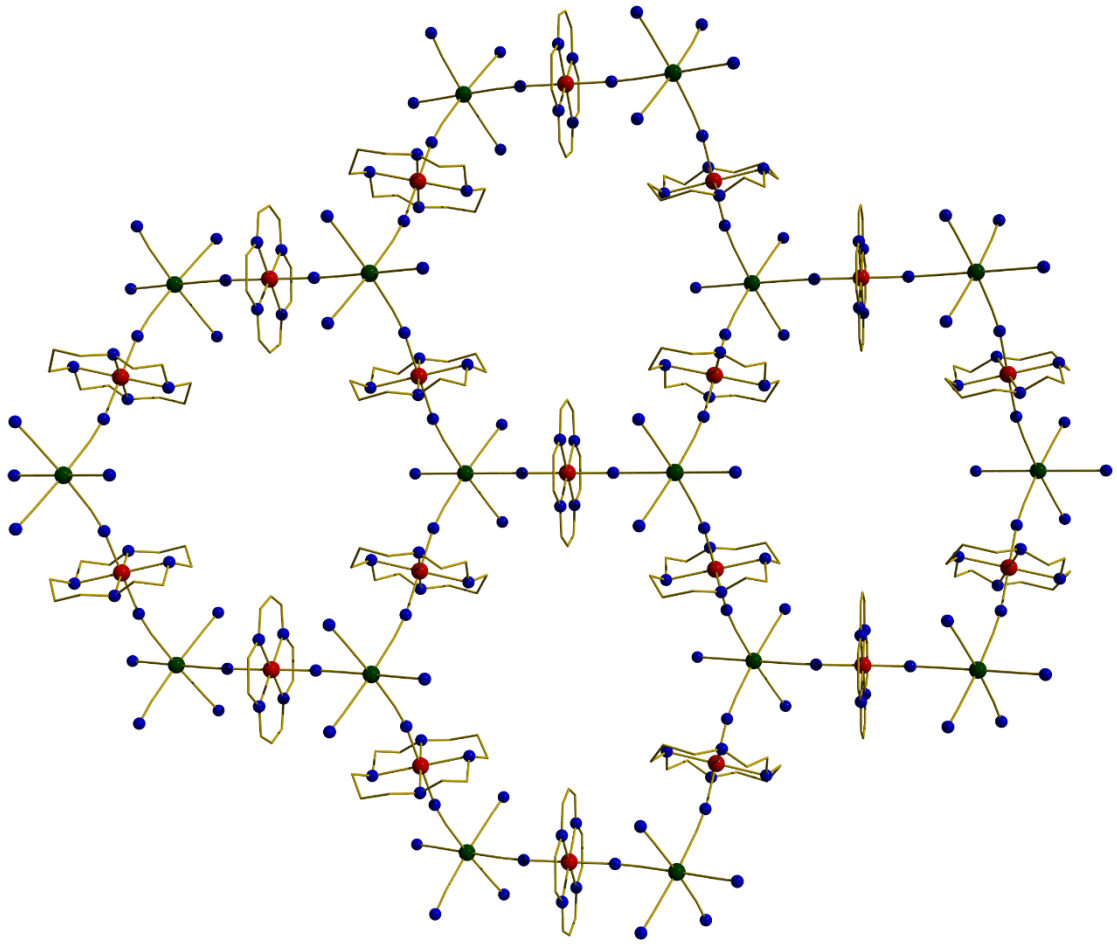

Figure 1.14. Molecular structure of $[Ni\text{-}(cyclam)]_3[Cr(CN)_6]_2$. Ni = red, Cr = green, O = red, N = blue. H atoms removed for clarity.

In 1999 the first paramagnetic molecular square was reported by Oshio and co-workers. [26] The complex $[Fe^{III}_2Cu^{II}_2(\mu\text{-}CN)_4(bipy)_6]^{6+}$ was synthesised using $[Fe(CN)_2(bpy)_2](PF_6)$ and $[Cu(bpy)(CH_3OH)_2](PF_6)$. The square consists of two six coordinate Fe^{III} metal centres and two square planar Cu^{II} centres. The Fe^{III} and Cu^{II} ions are bridged alternately through the CN^- ligands, where the cyanide C atom acts as a π acceptor and coordinates to the π donor Fe^{III} ions. The 4 remaining coordination sites on Fe are filled with the N atoms from two 2,2-bipyridine (2,2-bipy) ligands. The square geometry of the complex is confirmed by the C-Fe-C and N-Cu-N bond angles at 91.8° and 88.5° respectively. Magnetic susceptibility data confirmed antiferromagnetic coupling.[26]

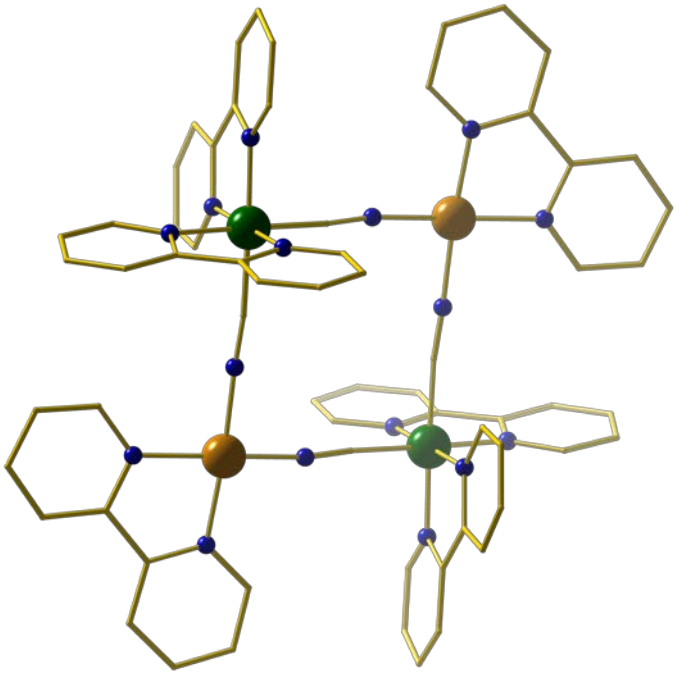

Figure 1.15. Molecular structure of $[Fe^{III}_2Cu^{II}_2(\mu\text{-}CN)_4(bipy)_6]^{6+}$. Cu = green, Fe = teal, N = blue. H-atoms removed for clarity.

Serendipitous Self-Assembly

One obvious disadvantage of systematically designing and predicting synthetic outcomes is that the possibility of products is limited. Serendipitous assembly relies on the coordinative flexibility of both the metal ions and ligands employed, whereby variable geometries and bridging modes can potentially afford a plethora of different structure types by exploiting the lack of control in the synthetic process.[27] This approach leads to a far more diverse and rich variety of structure types than that seen *via* rational design.

The literature contains examples of anything from small homo and hetero polymetallic systems to larger aggregates of nuclearity greater than 30, and in some cases surpassing 100. The serendipitous elements of their syntheses can be attributed to by the flexibility of the chelate and bridging ligands present. Examples of flexible chelating ligands used in the cases discussed below are shown in Figure 1.16:

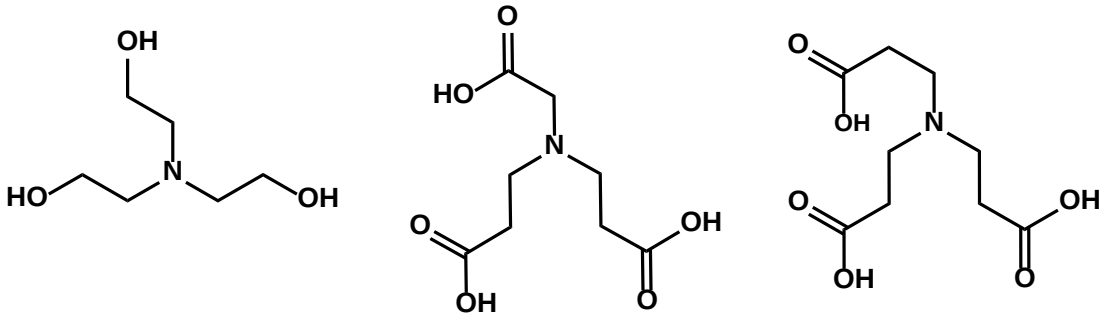

Figure 1.16. Structures of left: $TeaH_2$ (triethanolamine), centre: H_3ndpa ((nitrilodipropionic)acetic acid) and right: H_2ntp (nitrilotripropionic acid).

Traditionally the number of available oxidation states and the source of molecular anisotropy in the JT axis of octahedrally coordinated Mn^{III} results in Mn complexes being highly sought after and therefore they take up a large portion of the literature on paramagnetic species.[28] An excellent early example is the synthesis of the first single molecule magnet (SMM), $[Mn_{12}O_{12}(O_2CMe)_{16}(H_2O)_4]$ (referred to as $[Mn_{12}OAc]$) made *via* the oxidation of $Mn(OAc)_2.4H_2O$ with MnO_4^- in a mixture

of acetic acid and H_2O.[29] This complex has a spin ground state of S = 10 as a result of antiferromagnetic exchange between the Mn^{III} and Mn^{IV} ions present.[30] The first Mn complex of nuclearity 30 or greater was synthesised in 2001 in which $[Mn_{12}O_{12}((CH_3)_3\text{-}CCH_2CO_2)_{16}(H2O)_4]$ was recrystallized in solvents DCM and $MeNO_2$ to give the product $[Mn_{30}O_{23}(OH)_8((CH_3)_3CCH_2\text{-}CO_2)_{32}(H2O)_2(CH_3NO_2)_4]$.[31] This mixed-valent structure possesses Mn centres in the II, III and IV oxidation states. Although the complex displays antiferromagnetic exchange it also exhibits SMM behaviour. The reaction of $[Mn_{12}OAc]$ with MnO_4^- and acetic acid in MeOH leads to the formation of the torus shaped $[Mn_{84}O_{72}(O_2CMe)_{78}(OMe)_{24}(OH)_6(MeOH)_{12}(H_2O)_{48}]$, perhaps the most aesthetically pleasing SMM ever made (Figure 1.17).[32] The torus spans a diameter of 4.2 nm in which 1.9 nm consistutes the central hole.

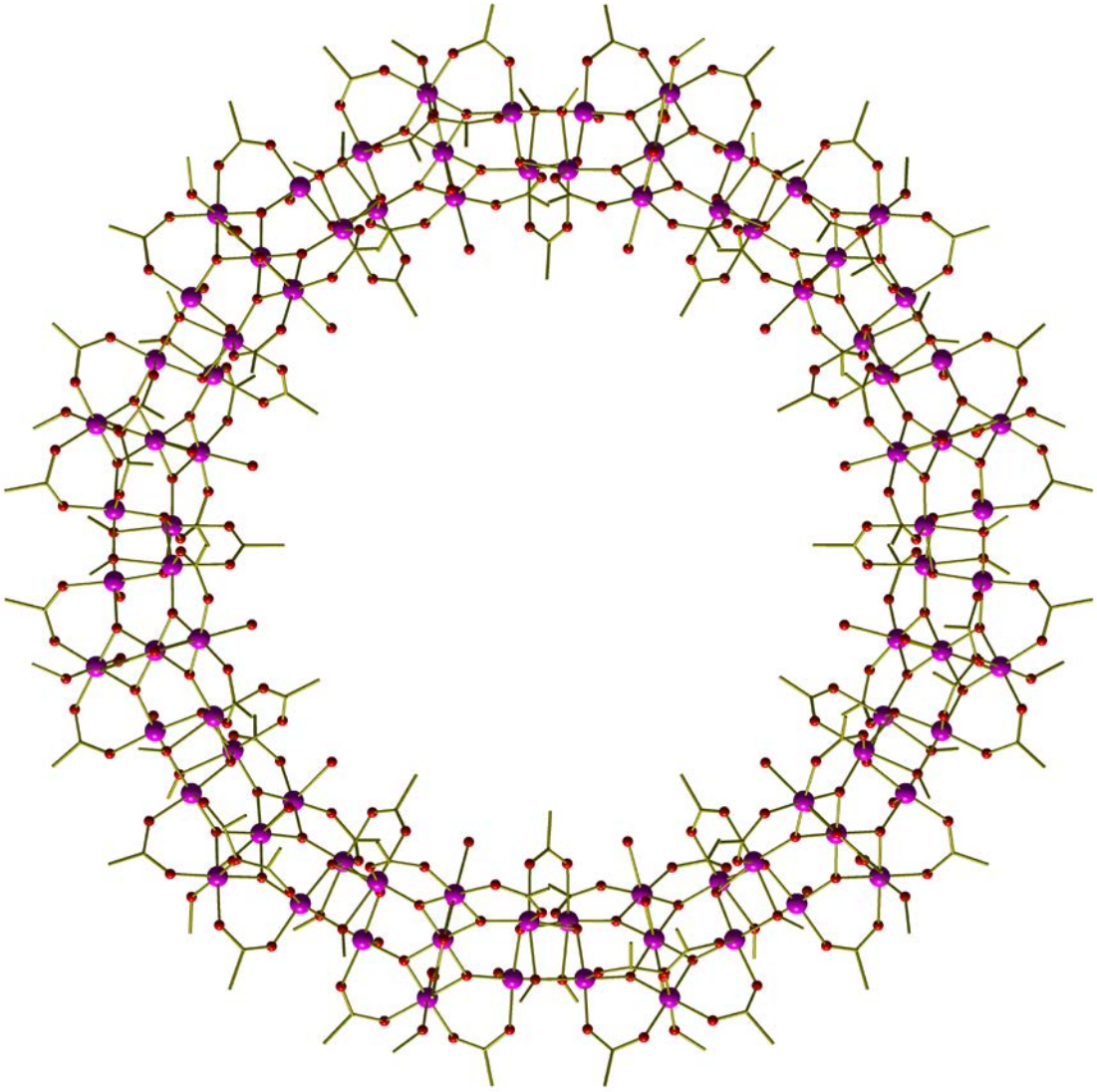

Figure 1.17. Molecular structure of $[Mn_{84}O_{72}(O_2CMe)_{78}(OMe)_{24}(OH)_6(MeOH)_{12}(H_2O)_{48}]$. Mn = pink, O = red. H atoms removed for clarity.

Amongst other large paramagnetic polymetallic clusters there are two examples of $[Cu^{II}_{36}]$ frameworks.[33] $[Cu^{II}_{36}(\mu_3\text{-}OH)_{32}(\mu\text{-}OR)_8Cl_6(ndpa)_8(H_2O)_5\{KCl\}]^{3-}$ was synthesised from the one pot reaction of H_3ndpa ((nitrilodipropionic)acetic acid), KOH and $CuCl_2.2H_2O$. The reaction conditions have been deemed as essential in the formation of the cluster, as in the solvent of reagent-grade MeOH, the product crystallised out in two weeks. However in absolute MeOH the product crystallised after two months and also contained two Cu^I centres attached to the aggregate.[33] The $[Cu_{28}]$ framework surrounds the $[KCl_6]^{5-}$ template. Furthermore

$[Cu(npda)Cl]^{2-}$ and $[Cu_2Cl(npda)_2]^{3-}$ moieties encapsulate the entire framework. The cuboidal $[Cu_{44}(\mu_8\text{-}Br)_2(\mu_3\text{-}OH)_{36}(\mu\text{-}OH)_4(ntp)_{12}Br_8$, was synthesised using $CuBr_2$, H_2ntp (nitrilotripropionic acid). The complex consists of bridging OH- and Br- ions.[34] The above $[Cu_{36}]$ and $[Cu_{44}]$ structures, reported by the same group, all exhibit antiferromagnetic interactions.[33,34]

The literature also presents heterometallic complexes with both a combination of *d*-*d*' metals and even *d*-Ln metals.[35,36,37,38] One example of the former by Hendrickson et al. is $[Cu_{17}Mn_{28}O_{40}]^{42+}$ (Figure 1.18), synthesised using Cu powder, $Mn(OAc)_2.4H_2O$ and the tetradentate chelate, $teaH_2$ (triethanolamine) in a 1:2:1 ratio in DMF.[39] The mixed-valent cluster consists of Cu^{I}, Cu^{II}, Mn^{II} and Mn^{III} ions.

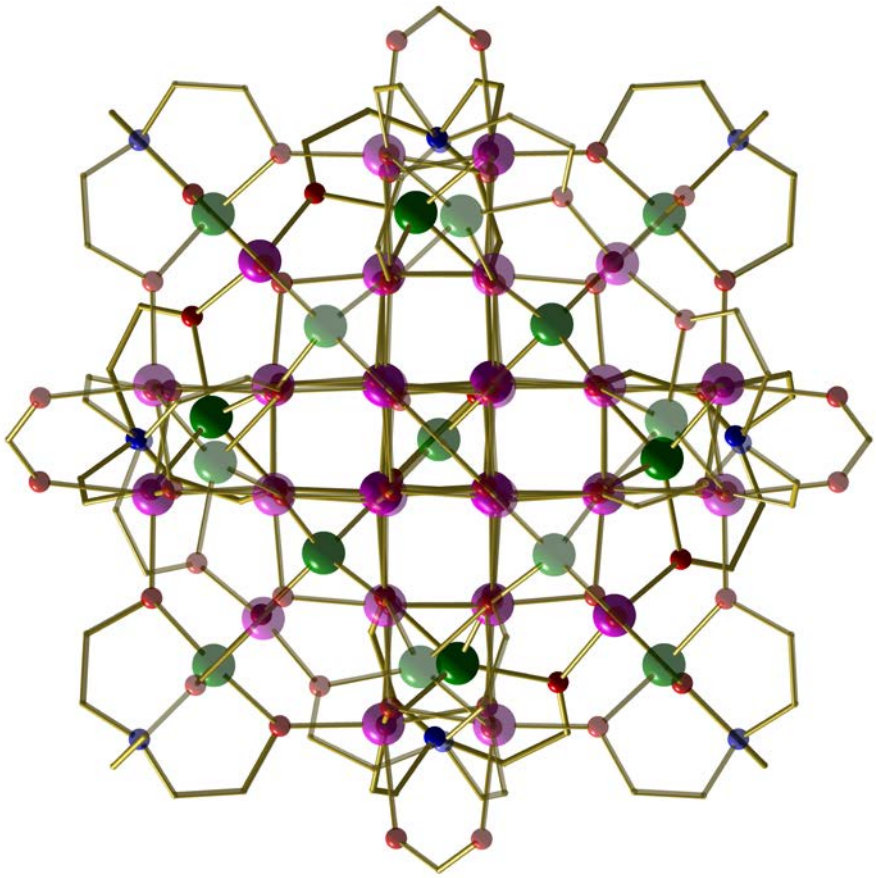

Figure 1.18. Molecular structure of $[Cu_{17}Mn_{28}O_{40}]^{42+}$. Mn = pink, Cu = green, N = blue, O = red. H atoms removed for clarity.

As mentioned above the synthesis of frameworks with nuclearity greater than 100 is also becoming more common for both paramagnetic and diamagnetic metals. Approaching protein-sized complexes, two chiral [Fe_{168}] complexes $Na_{96}[Na_{24}Fe_{168}(L\text{-}Tart)_{96}(\mu_3\text{-}O)_{48}(HCOO)_{144}]$ and $Na_{96}[Na_{24}Fe_{168}(D\text{-}Tart)_{96}(\mu_3\text{-}O)_{48}(HCOO)_{144}]$ were synthesised in 2009, through the reaction of $Fe(NO_3)_3$, (L-(+)-tartaric acid/ D-(-)-tartaric acid and Na_2CO_3.[40] The structure consists of six [Fe_{28}] units which take a wheel formation and also twelve [Na_4] cubanes which link the Fe building blocks. Both enantiomers exhibit strong antiferromagnetic coupling.[40] The synthesis of such large structures necessitate the consideration of steric effects of the bridging ligands, which has led to combining elements of predicting the possible outcome as well as relying on elements of serendipity for its formation.

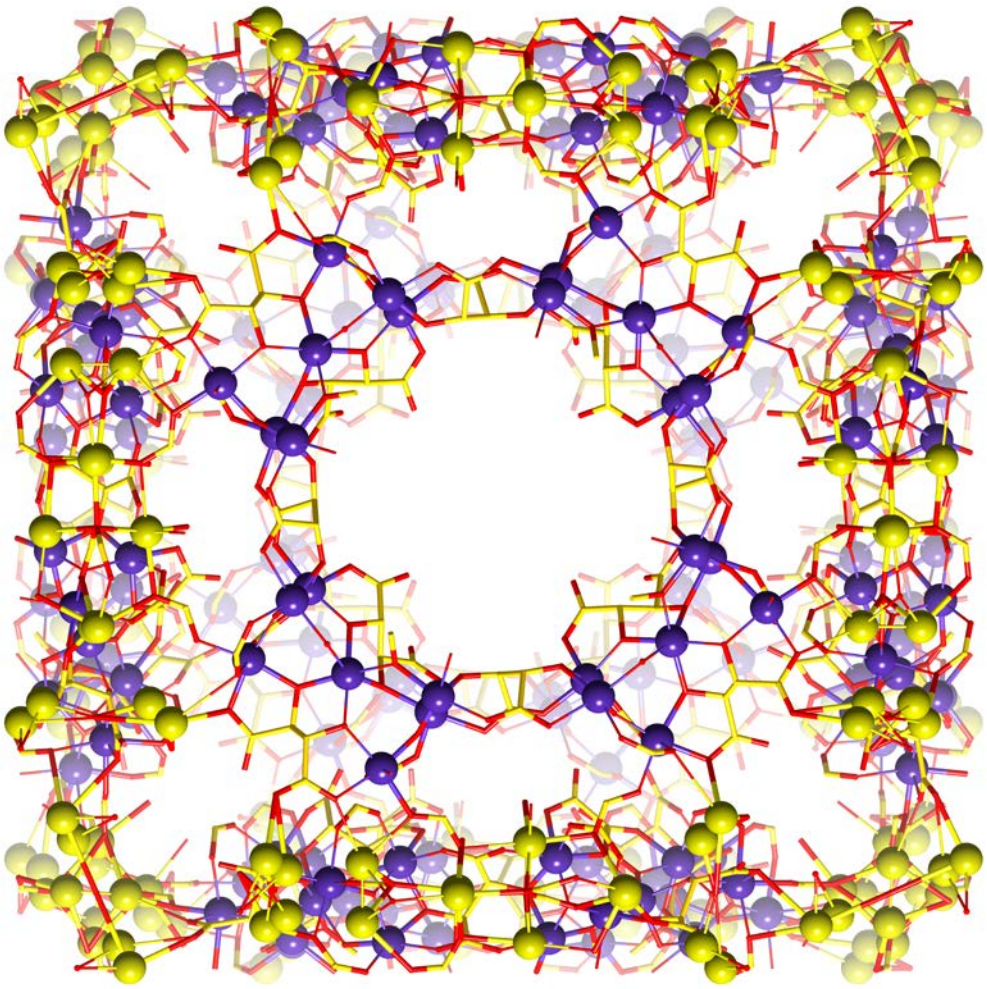

Figure 1.19. Molecular structure of [L-Fe_{168}]. Fe = purple, Na = yellow, O = red. H atoms removed for clarity.

The above complexes show the ability to use flexible ligands and unpredictably synthesise different complexes just by adjusting the reaction conditions. The outcomes of these reactions would not necessarily be known beforehand due to the possibility of different coordination modes from the ligands. Although the systematic nature of rational design can seem appealing, it can often be beneficial to take elements of both synthetic routes and combine them to target frameworks with fragments that could be predicted and other sub-units which are not so straight forward to anticipate.

Over the past decade there has been an increase in interest in molecular magnetism and also combining this with other areas of chemistry. The choice of metal ions used in the building of new structures can widen the scope of the possible properties and applications of newly reported clusters. For example, building larger 3-dimensional networks opens the possibility for application in host-guest chemistry and high-pressure studies, as well as combining each of these fields to see their effect on magnetic properties. In an attempt to build on this and to provoke new interest in pushing the limits of our understandings of these fields higher, the work in this thesis aims to emphasise bridging the gap between different scientific fields from across the spectrum, from purely magnetic studies, to behaviour of paramagnetic species under pressure. This work begins by attempting to understand the exchange interactions of paramagnetic metal centres in simple building blocks which would potentially be applied to larger, more complicated structures. Following this, larger, more complicated structures are built using simple precursors. The complexity of these structures originates from the size and presence of heterometallic units, showing the difficulty in probing and understanding the exchange interactions in structures of these types Finally, a metal-organic framework (MOF) is built in which high-pressure studies are performed. This highlights the applicability of paramagnetic structures to other fields of chemistry. A more specific explanation of the contents of each chapter is given below.

Chapter 2 entails work on experimental and theoretical magneto-structural studies on simple Mn^{II} dimers. Newly reported compounds have been combined with those already published to build a large family of double oxime bridged dimers which are structurally similar however have different exchange interactions due to the orientations of the JT axes.

Chapter 3 is aimed at building the gap between supramolecular chemistry and molecular magnetism. A family of coordination cages have reported along with their magnetic susceptibility and EPR studies. These novel compounds illustrate the

ability to build isostructural 3-dimensional clusters, however replacing the bridging metal centres.

Chapter 4 of this thesis contains the high-pressure study of a Cu^{II} MOF in which a number of interesting structural changes are observed, including a pressure-induced phase transition, NLC behaviour and also a pressure controlled Jahn-Teller switching.

1.3 References

1. D. Gatteschi, O. Kahn and R. D. Willett, *Magneto Structural Correlations in Exchange Coupled Systems*, D. Reidel, Dordrecht, 1985.
2. R. E. P. Winpenny and E. J. L. McInnes, *Molecular Materials,* 281.
3. C. J. Milios, R. Inglis, A. Vinslava, R. Bagai, W. Wernsdorfer, S. Parson, S. P. Perlepes, G. Christou and E. K. Brechin, *J. Am. Chem. Soc.*, 2007, **129**, 12505.
4. V. H. Crawford, H. W. Richardson, J. R. Wasson, D. J. Hodgson and W. E. Hatfield, *Inorg. Chem*., 1976, **15**, 2107.
5. W. E. Hatfield, *Comments on Inorganic Chemistry*, 1981, **1**, 105.
6. T. J. Morsing, H. Weihe and J. Bendix, *Eur. J. Inorg. Chem*., 2014, 5990.
7. E. D. Estes, R. P. Scaringe, W. E. Hatfield and D. J. Hodgson, *Inorg. Chem.*, 1977, **16**, 1600.
8. C. Reber, H. Gudel, L. Spiccia and W. Marty, *Inorg. Chem*., 1987, **26**, 3186.
9. T. J. Morsin, S. P A. Sauer, H. Weihe, J. Bendix and A. Døssing, *Inorg. Chim. Acta*, 2013, **396**, 72.
10. J. Glerup, D. J. Hodgon and E. Pedersen, *Acta Chemica Scandinavica*, 1983, 161.
11. W. P. Barros, R. Inglis, G. S. Nichol, T. Rajeshkumar, G. Rajaraman, S. Piligkos, H. O. Stumpf and E. K. Brechin, *Dalton Trans*., 2013, **42**, 16510.
12. N. Berg, T. Rajeshkumar, S. M. Taylor, E. K. Brechin, G. Rajaraman and L. F. Jones, *Chem. Eur. J.*, 2012, **18**, 5906.
13. R. Werner, S. Ostrovsky, K. Griesar and W. Haase, *Inorg. Chim. Acta.*, 2001, **326**, 78.
14. S. M. Gorun and S. J. Lippard, *Inorg. Chem.*, 1991, **30**, 1625.
15. H. Weihe and H. U. Gudel, *J. Am. Chem. Soc.*, 1997, **119**, 6539.
16. G. G.-Barros, Y. Li, A. M. Z. Slawin, D. T. Richens, I. A. Gass, P. R. Murray, L. J. Yellowlees and E. K. Brechin, *Dalton Trans*., 2008, 551.
17. P. J. Stang, *Chem. Eur. J.*, 1998, **4**, 20.
18. M. Fujita,D. Oguro, M. Miyazawa, H. Oka, K. Yamaguchi and K. Ogura, *Nature*, 1995, **378**, 469.
19. M. Fujita, M. Tominaga, A. Hori and B. Therrien, *Acc. Chem. Res.*, 2005, **38**, 371.
20. M. Fujita, K. Umemoto, M. Yoshizawa, N. Fujita, T. Kusakawa and K. Biradha, *Chem. Commun*., 2001, 509.
21. R. Chakrabarty, P. S. Mukherjee and P. J. Stang, *Chem. Rev*., 2011, **111**,6810.
22. J. N. Rebilly and T. Mallah, *Struct. Bond*., **122**. 103

23. V. Marvaud, C. Decroix, A. Scuiller, F. Tuyèras, C. Guyard-Duhayon, J. Vaissermann, J. Marrot, F. Gonnet and M. Verdaguer, *Chem. Eur. J*., 2003, **9**, 1692.
24. T. Mallah, C. Auberger, M. Verdaguer and P. Veillet, *J. Chem. Soc.*, *Chem. Commun*., 1995, 61.
25. S. Ferlay, T. Mallah, J. Vaissermann, F. Bartolomé, P. Veillet and M. Vergaguer, *Chem. Commun*., 1996, 2481.
26. H. Oshio, O. Tamada, H. Onodera, T. Ito, T. Ikoma and S Tero- Kubota, *Inorg. Chem.*, 1999, **38**, 5686.
27. R. E. P. Winpenny, *J. Chem.* Soc., *Dalton Trans.*, 2002, 1.
28. G. Aromi and E. K. Brechin, *Struc. Bond*., 2009, **122**, 1-69.
29. T. Lis, *Acta Crystallogr*., 1980, **36**, 2042.
30. A. Caneschi, D. Gatteschi, R. Sessoli, A.-L. Barra, L. C. Brunel and M. Guillot, *J. Am. Chem. Soc.*, 1991, **113**, 5873.
31. M. Soler, W. Wernsdorfer, K. Folting, M. Pink and G. Christou, *J. Am. Chem. Soc*, 2004, **126**, 2156.
32. A. J. Tasiopoulos, A. Vinslava, W. Wernsdorfer, K. A. Abboud and G. Christou, *Angew. Chem. Int. Ed.*, 2004, **43**, 2117.
33. M. Murugesu, R. Clérac, C. E. Anson and A. K. Powell, *Chem. Commun*, 2004, 1598.
34. M. Murugesu, R Clérac, C. E. Anson and A. K. Powell, *Inorg. Chem*., 2004, **43**, 7269.
35. G. F. S. Whitehead, F. Moro, G. A. Timco, W. Wernsdorfer, S. J. Teat and R. E. P. Winpenny, *Angew. Chem. Int., Ed.*, 2013, **52**, 9932.
36. G. F. Whitehead, J. Ferrando-Soria, L. G. Christie, N. F. Chilton, G. A. Timco, F. Moro and R. E. P. Winpenny, *Chem. Sci.*, 2014, **5**, 235.
37. M. Charalambous, E. E. Moushi, C. Papatriantafyllopoulou, W. Wernsdorfer, V. Nastopoulos, G. Christou and A. J. Tasiopoulos, *Chem. Commun*., 2012, **48**, 5410.
38. X.-J. Kong, L. S- Long, R.-B. Huang, L-S. Zheng, T. D. Harris and Z. Zheng, *Chem. Commun*., 2009, 4354.
39. W.G. Wang, A.-J. Zhou, W.-X. Zhang, M.-L. Tong, X.-M. Chen, M. Nakano, C. C. Beedle and D. N. Hendrickson, *J. Am. Chem. Soc.,* 2007, **129**, 1014.
40. Z.-M. Zhang, S. Yao, Y.-G. Li, R. Clerac, Y. Lu, Z.-M. Su and E.-B. Wang, *J. Am. Chem. Soc.*, 2009, **131**, 14600.

Chapter 2

Switching the orientation of Jahn-Teller axes in oxime-based Mn^{III} dimers and its effect upon magnetic exchange

2.1 Introduction

Molecular Magnets – molecules containing exchange-coupled paramagnetic metal ions – are an enormously important class of material with potential applications across a diverse range of fields from information storage, quantum computation and molecular spintronics to cryogenic refrigeration and biomedical imaging.[1-5] Such species combine the macroscopic properties of magnets with the quantum mechanical properties of molecules, allowing detailed study of quantum size effects in monodisperse, reproducible, orientable, chemically tuneable molecules.[6] Recent years have witnessed a plethora of important scientific breakthroughs, including: the observation of quantum tunnelling of the magnetization, quantum phase interference, memory effects at T = 14 K, single-molecule magnetic detection, the construction of molecular spintronic devices, molecules and coordination polymers displaying enormously enhanced magneto-caloric effects, and the development of protocols for molecule-based quantum information processing.[7-20] The discovery of such phenomena, and any potential exploitation thereof, is based upon a detailed understanding of and subsequent control over the structure-magnetism relationship. This in turn is derived from a systematic synthetic study of the effects of ligand design, metal identity and reaction conditions upon symmetry and structure, in tandem with detailed physical characterisation and theoretical analysis.[21]

Manganese is often a good choice for constructing such molecules: it commonly exists in the II+, III+ and IV+ oxidation states, resulting in the majority of clusters being mixed-valent. This decreases the likelihood of antiferromagnetically coupled cages possessing diamagnetic spin ground states.[6] The Jahn-Teller (JT) distorted Mn^{III} ion also provides a of source magnetic anisotropy that has often been employed in the construction of Single-Molecule Magnets (SMMs),[6] whilst the isotropic Mn^{II} ion finds application in clusters displaying an enhanced magnetocaloric effect (MCE), a phenomenon that can be exploited for low temperature cooling.[17] Application first requires the development of MSCs,

however this can often be a difficult task due to prohibitively large nuclearities and/or complex exchange interaction patterns. One way to overcome such issues is to construct families of low nuclearity cages (*e.g.* dimers, trimers, tetramers) which mimic the building blocks of the bigger cages, and investigate how small structural perturbations affect magnetic exchange. Detailed studies on Mn^{III} dimers, however, remain relatively scarce.[22] A recent experimental and theoretical study of alkoxide-bridged $[Mn^{III}(OR)]_2$ dimers revealed that the dominant structural feature controlling magnetic exchange (*J*) was the relative orientations of the JT axes.[22] A parallel orientation, perpendicular to the bridging plane of the molecule (Type I, Figure 2.1) resulted in weak antiferromagnetic exchange; a parallel orientation within the bridging plane (Type II, Figure 2.1) led to borderline cases in which the exchange could be either weakly ferromagnetic or weakly antiferromagnetic; whilst a perpendicular orientation (Type III, Figure 2.1) produced ferromagnetic exchange. For the oxime/oxo bridged species $[Mn^{III}{}_2(O)(NO)]$ (Figure 2.1, A) the Mn-N-O-Mn torsion angle dominates, with a linear correlation found between the magnitude of *J* and the torsion angle.[22] DFT studies on double-oxime bridged dimers $[Mn^{III}(NO)]_2$ (Figure 2.1, B) also revealed a pronounced dependence of the exchange coupling on the relative twisting of the oxime moiety, as proposed previously in more complicated $[Mn^{III}{}_3]$ and $[Mn^{III}{}_6]$ clusters,[23] resulting from an accidental orthogonality between the Mn–N–O plane of the first Mn^{III} ion and the JT axis of the second Mn^{III} ion.[22]

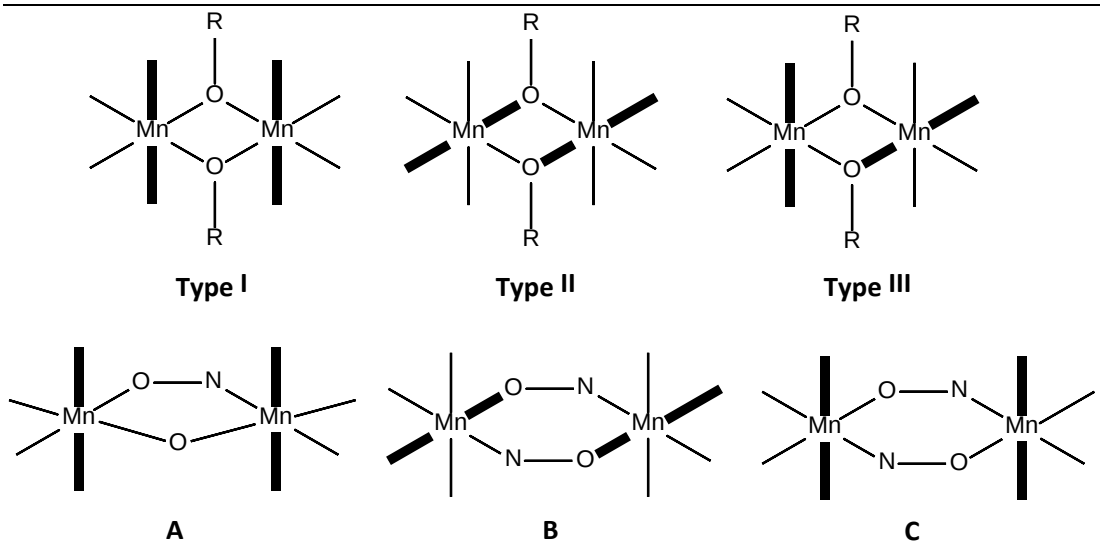

Figure 2.1. Top: alkoxide bridged dimers $[MnII(OR)]_2$ with Type I-III structures differing in the relative orientation of the JT axes, which are highlighted in bold. Bottom: oxime/ oxo dimers $[Mn^{III}_2(O)(NO)]$ (A), and the double oxime bridged dimers $[Mn^{III}(NO)]_2$ in which the JT axes in the bridging plane (B), and perpendicular to the bridging plane (C).

In order to extend the family of double-oxime bridged Mn^{III} dimers – which has just two members – we herein report a series of double-oxime bridged $[Mn^{III}(NO)]_2$ species in which employment of the chelating ligand di-(2-picolyl)-amine, dpa (Figure 2.2), switches the orientation of the JT axes from being in the bridging plane (structure type **B**, Figure 2.1) to being perpendicular to the bridging plane (structure type **C**, Figure 2.1) and present a combined experimental and theoretical analyses of the effect of JT switching upon the magnetic exchange between the two Mn^{III} ions.

2.2 Experimental

Materials and Physical Measurements

All synthetic procedures were performed under aerobic conditions, using chemicals as received (reagent grade). **Caution!** Although no problems were encountered here, care should be taken when handling the potentially explosive perchlorate anion. The substituted phenolic oximes were synthesised using the

appropriate precursor ketones, hydroxylamine hydrochloride and sodium acetate in EtOH.[24] Variable temperature, solid state magnetic susceptibility data down to 5 K were collected on a Quantum Design MPMS XL SQUID magnetometer equipped with a 7 T dc magnet. Diamagnetic corrections were applied to the observed paramagnetic susceptibilities using Pascal's constants.

$[Mn^{III}_2(Et\text{-}sao)_2(dpa)_2](ClO_4)_2$ (1): $Mn(ClO_4)_2{\cdot}6H_2O$ (0.145 g, 0.4 mmol) and Et-saoH_2 (0.066 g, 0.4 mmol) were dissolved in MeOH (10 mL). NH_4OH (61.6 µL, 1.6 mmol) was then added to the solution and the reaction was left to stir for 40 minutes at room temperature. Dpa (74.1 µL, 0.4 mmol) in EtOH (10 mL) was added to the reaction mixture, which was then filtered after a further 5 minutes of stirring. The black mother liquor was left to crystallise by slow evaporation for 4 days, producing black block crystals. Elemental analysis (%) calculated (found) C: (48.39) 48.26, H: (4.32) 4.45, N: (10.75) 10.82.

$[Mn^{III}_2(Me\text{-}sao)_2(dpa)_2](ClO_4)_2$ (2): $Mn(ClO_4)_2{\cdot}6H_2O$ (0.145g, 0.4 mmol) and Me-saoH_2 (0.06 g, 0.4 mmol) were dissolved in MeOH (10 mL). NH_4OH (61.6 µL, 1.6 mmol) was then added to the solution and the reaction was left to stir for 40 minutes at room temperature. Dpa (142.32 µL, 0.8 mmol) in EtOH (10 mL) was added to the reaction mixture, which was then filtered after 5 minutes. The black mother liquor was left to crystallise by slow evaporation for 4 days, producing black block crystals. Elemental analysis (%) calculated (found) C: (44.96) 44.84, H: (3.56) 4.34, N: (10.49) 10.92.

$[Mn^{III}_2(Me_2\text{-}sao)_2(dpa)_2](ClO_4)_2$ (3): $Mn(ClO_4)_2{\cdot}6H_2O$ (0.145 g, 0.4 mmol) and Me_2-saoH_2 (0.066g, 0.4 mmol) were dissolved in MeOH (10 mL). NH_4OH (61.6 µL, 1.6 mmol) was then added to the solution and the reaction was left to stir for 40 minutes at room temperature. Dpa (74.1 µL, 0.4 mmol) in EtOH (10 mL) was added to the reaction mixture, which was then filtered after 5 minutes. The black mother liquor was left to crystallise by slow evaporation for 2-4 days, producing black block crystals. Elemental analysis (%) calculated (found) C: (47.56) 47.32, H: (5.17) 5.93, N: (9.64) 9.87.

$[Mn^{III}_2(sao)_2(dpa)_2](ClO_4)_2$ (4): $Mn(ClO_4)_2 \cdot 6H_2O$ (0.145 g, 0.4 mmol) and $saoH_2$ (0.055 g, 0.4 mmol) were dissolved in MeOH (10 mL). Benzyl trimethyl ammonium hydroxide (280 µL, 1.6 mmol) was then added to the solution and the reaction was left to stir for 40 minutes at room temperature. Dpa (74.1 µL, 0.4 mmol) in EtOH (10 mL) was added to the reaction mixture, which was then filtered after 5 minutes. The black mother liquor was left to crystallise by slow evaporation for 4 days, producing black block crystals. Only a very small amount of **4** could be made, precluding calculation of a yield and CHN analysis.

$[Mn^{III}_2(Ph\text{-}sao)_2(dpa)_2](ClO_4)_2$ (5): $Mn(ClO_4)_2 \cdot 6H_2O$ (0.145 g, 0.4 mmol) and $Ph\text{-}saoH_2$ (0.085 g, 0.4 mmol) were dissolved in a THF/MeOH mixture (6 mL / 4 mL). NH_4OH (61.6 µL, 1.6 mmol) was then added to the solution and the reaction was left to stir for 40 minutes at room temperature. Dpa (74.1 µL, 0.4 mmol) in EtOH (10 mL) was added to the reaction mixture, which was then filtered after 5 minutes. The black mother liquor was left to crystallise by slow evaporation for 4 days, producing black block crystals. Elemental analysis (%) calculated (found) C: (54.37) 54.62, H: (4.57) 4.13, N: (8.99) 9.66.

X- Ray Crystallography

Diffraction data for samples **1** and **3**-**5** were collected on an Oxford Diffraction SuperNova diffractometer using Mo or Cu Kα radiation. The crystal temperature was maintained at 120 K using an Oxford Cryosystems Cryostream 700+ low temperature device. The structures were solved by direct methods and refined by full-matrix least-squares techniques on F^2 using the programs SHELXL[25a] and Olex2.[25b] X-ray data for complex **2** were collected at 100 K (Oxford Cryosystems Cobra) on a Rigaku AFC12 goniometer equipped with an enhanced sensitivity (HG) Saturn724+ detector mounted at the window of an FR-E+ SuperBright molybdenum rotating anode generator with VHF Varimax optics (70m focus). The crystal structure was solved by charge flipping methods in SUPERFLIP[25c] and the full-matrix least-squares refinement on F_o^2 was carried out using SHELXL.[25a] All non-hydrogen

atoms were refined with anisotropic displacement parameters. All H-atoms were added at calculated positions and refined using a riding model with isotropic displacement parameters based on the equivalent isotropic displacement parameter (U_{eq}) of the parent atom.

Table 2.1. Crystallographic information for complexes **1**-**5**.

Identification code	**1**	**2**	**3**	**4**	**5**
Empirical formula	$C_{42}H_{52}Cl_2Mn_2N_8O_{12.44}$	$C_{42}H_{46}Cl_2Mn_2N_8O_{14}$	$C_{46}H_{60}Cl_2Mn_2N_8O_{16}$	$C_{56.44}H_{56.87}Cl_2Mn_2N_8O_{13.61}$	$C_{40}H_{44}Cl_2Mn_2N_8O_{14}$
Formula weight	1041.5	1067.65	1161.8	1245.74	1041.61
Temperature	120.0 K	100.0 K	120.0 K	120.0 K	120.0 K
Wavelength (Å)	1.5418	0.71073	0.71073	1.54184	1.54184
Crystal system	Monoclinic	Triclinic	Monoclinic	Triclinic	Monoclinic
Space group	*C*2/*c*	*P*-1	*C*2/*c*	*P*-1	$P2_1/c$
a (Å)	21.1082(7)	13.1019(7)	25.9020(12)	8.4822(4)	14.2526(7)
b (Å)	10.3582(3)	14.5141(7)	10.4638(4)	13.2500(4)	22.2504(12)
c (Å)	22.8139(7)	14.8351(10)	21.9889(11)	13.6070(5)	15.7127(11)
α (°)	90°	105.116(7)	90	110.595(3)	90
β (°)	115.866(4)°	110.267(8)	103.471(5)	103.803(4)	116.936(8)
γ (°)	90°	108.665(8)	90°	92.048(3)	90°
Volume (Å^3)	4488.4(3)	2277.5(3)	5795.8(5)	1378.12(10)	4442.3(5)
Z	4	2	4	1	4
Theta range for data collection	4.307 to 76.096°.	3.037 to 25.027°	2.965 to 26.372°.	3.595 to 76.336°.	3.478 to 52.004°.
Reflections collected	34109	20147	28756	21371	19662
Independent reflections	4658 [R(int) = 0.0397]	7870 [R_{int} = 0.0996]	5895 [R(int) = 0.0473]	5662 [R(int) = 0.0353]	4819 [R(int) = 0.0692]
Data / restraints / parameters	4658 / 0 / 318	7870 / 2 / 597	5895 / 0 / 304	5662 / 151 / 383	4819 / 47 / 605

Goodness-of-fit on F^2	1.057	1.05	1.084	1.051	1.033
Final R indices [I>2sigma(I)]	R1 = 0.0369, wR2 = 0.0913	R1 = 0.0914, wR2 = 0.2472	R1 = 0.0492, wR2 = 0.1306	R1 = 0.0572, wR2 = 0.1539	R1 = 0.0692, wR2 = 0.1739
R indices (all data)	R1 = 0.0399, wR2 = 0.0928	R1 = 0.1205, wR2 = 0.2747	R1 = 0.0592, wR2 = 0.1359	R1 = 0.0632, wR2 = 0.1590	R1 = 0.1036, wR2 = 0.2073
Largest diff. peak and hole	0.331 and -0.719 e.Å^{-3}	1.331 and -0.803 e Å^{-3}	0.806 and -0.467 e.Å^{-3}	0.953 and -0.696 e.Å^{-3}	0.461 and -0.503 e.Å^{-3}

Table 2.2. Selected bond distances for complexes **1**-**5** (Å).

Bond	1	2	3	4	5
Mn1…Mn1	4.924	3.819	3.787	3.806	-
Mn1…Mn2	-	-	-	-	3.826
Mn1-N1	2.2727(18)	2.264(4)	2.238(2)	2.203(3)	2.207(6)
Mn1-N2	2.0971(18)	2.160(5)	2.110(2)	2.141(3)	2.116(6)
Mn1-N3	2.2979(18)	2.197(5)	2.258(2)	2.267(3)	2.245(6)
Mn1-N4	2.0081(17)	2.024(5)	2.009(2)	2.039(2)	2.002(6)
Mn1-O1	1.8590(14)	1.869(4)	1.8596(18)	1.867(2)	1.856(5)
Mn1-O2	1.9035(14)	1.895(4)	1.9080(18)	1.902(2)	1.886(5)
Mn2-N1'	-	-	-	-	2.213(6)
Mn2-N2'	-	-	-	-	2.148(6)
Mn2-N3'	-	-	-	-	2.162(6)
Mn2-N4'	-	-	-	-	2.026(6)
Mn2-O1'	-	-	-	-	1.847(5)
Mn2-O2'	-	-	-	-	1.884(5)

Computational details

Calculations were performed on the full crystal structures of **1**-**6,** by Dr Gopalan Rajaraman at the Indian Institute of Technology in Mumbai. A hybrid B3LYP[26] functional with TZV basis set[27] was employed for calculating the exchange constants as implemented in the G09[28] suite of programs. The high spin states (E-HS) and low spin states (E-BS) were estimated using single determinant wave functions and the broken symmetry approach,[29] respectively, and the corresponding *J* values were computed from the difference between E-HS and E-BS. Further details about the computational methodology are discussed elsewhere.[30]

2.3 Results and Discussion

Reacting $Mn(ClO_4)_2 \cdot 6H_2O$ with the appropriate phenolic oxime (R-saoH_2, Figure 2) and the tridentate ligand dpa in alcohol and in the presence of an appropriate base, produces black crystals of the complexes $[Mn^{III}_2$(Et-sao$)_2$(dpa$)_2](ClO_4)_2$ (**1**), $[Mn^{III}_2$(Me-sao$)_2$(dpa$)_2](ClO_4)_2$ (**2**), $[Mn^{III}_2$(Me$_2$-sao$)_2$(dpa$)_2](ClO_4)_2$ (**3**), $[Mn^{III}_2$(sao$)_2$(dpa$)_2](ClO_4)_2$ (**4**), and $[Mn^{III}_2$(Ph-sao$)_2$(dpa$)_2](ClO_4)_2$ (**5**) in varying yields over 4 days.

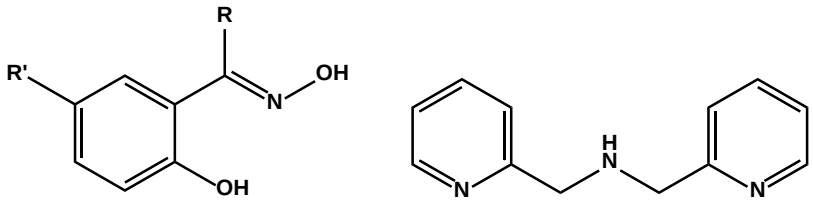

Figure 2.2. Structures of left: phenolic oxime, R-saoH_2 where R = H, Me, Et, Ph and R' = Me; right: di-(2-picolyl)amine, dpa.

Complexes **1**-**5** (Figure 2.3 and Table 2.1) describe simple, double-oxime bridged $[Mn^{III}(NO)]_2$ dimers with Mn-O-N-Mn torsion angles of approximately 79˚ (**1**) , 62˚ (**2**), 75˚ (**3**), 51˚ (**4**) and 63˚(**5**). The remaining coordination sites on each Mn ion are occupied the three N-atoms of the chelating dpa ligand, and a terminally bonded phenolic O-atom. The metal is thus six coordinate and in a distorted octahedral geometry with the JT axis being the N(pyridine)-Mn-N(pyridine) vector, which lies approximately perpendicular to the bridging $[Mn(NO)]_2$ plane (structure type **C**, Figure 1). The two JT axes are not strictly co-parallel but lie at dihedral angles (JT-Mn-Mn-JT) of approximately 26° (**1**), 24° (**2**), 21° (**3**), 23° (**4**) and 16° (**5**). The cluster is a 2+ cation with charge balance being maintained through the presence of two ClO_4^- anions (the packing of the molecules in **1**-**5** is shown below in Figures 2.4-2.8). Complexes **1**-**5** therefore represent an extension to the family of two previously reported $[Mn(NO)]_2$ dimers, namely the complexes $[Mn^{III}_2Zn^{II}_2$(Ph-sao$)_2$(Ph-saoH$)_4$(hmp$)_2$] (**6**) and $[Mn^{III}_2$(Naphth-sao$)_2$(Naphth-saoH$)_2$(MeOH$)_2$] (**7**) which are also shown in Figure 2.3 for comparison.[22] Although the bridging

$[Mn(NO)]_2$ moiety remains the same in all seven complexes, complexes **6** and **7** differ in that they have their Mn^{III} JT axes co-parallel and in the bridging plane (structure type **B**, Figure 2.1).

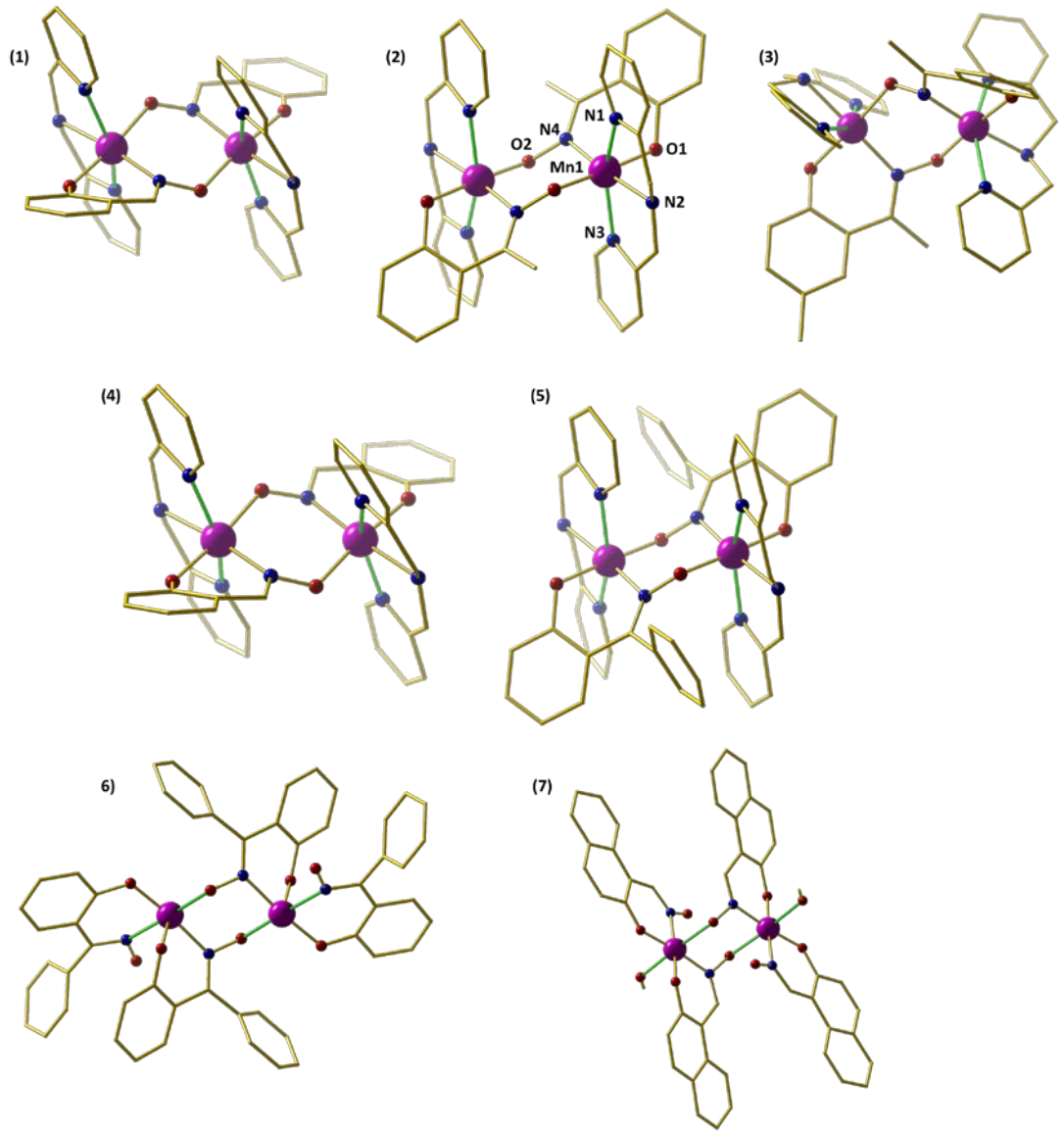

Figure 2.3. Molecular structures **1**-**5**. Mn = pink, C = gold, N = blue, O = red. H-atoms and counter-ions omitted for clarity.

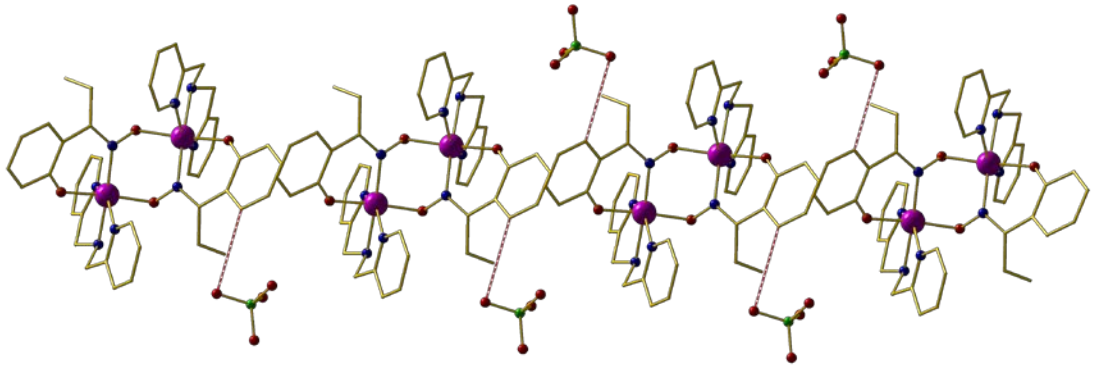

Figure 2.4. Packing of molecules in complex **1** as viewed down the *b*-axis. H-atoms omitted for clarity. H-bonding can be seen between ClO_4^- ions and phenol rings. Mn = pink, C = gold, N = blue, O = red, Cl = green.

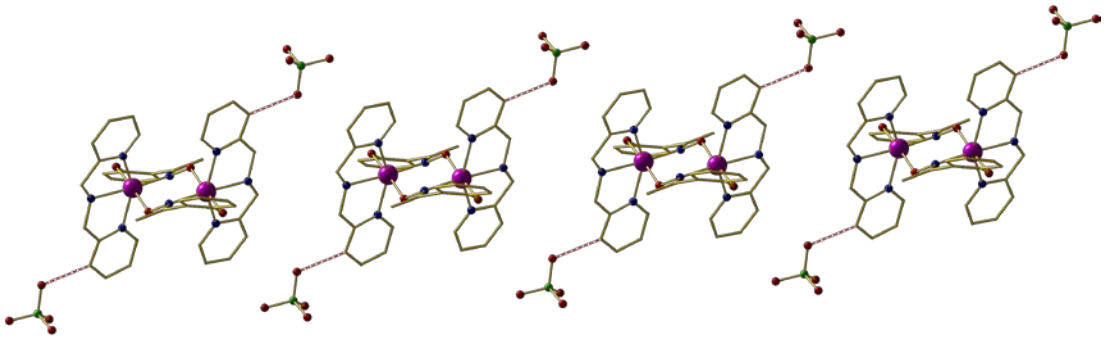

Figure 2.5. Packing of molecules in complex **2** as viewed along the *c*-axis. H-atoms omitted for clarity. H-bonding can be seen between ClO_4^- ions and pyridyl rings. Mn = pink, C = gold, N = blue, O = red, Cl = green.

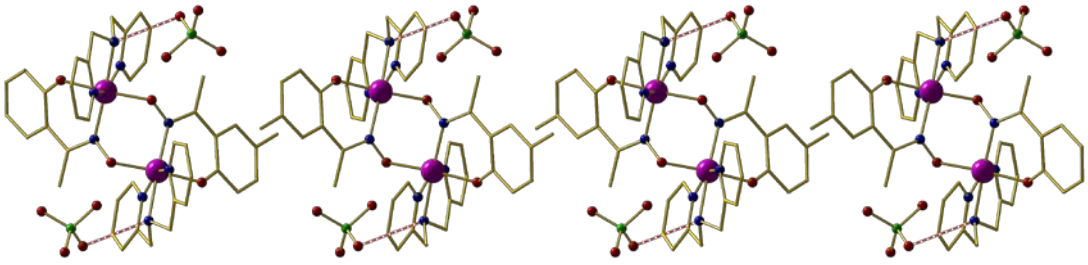

Figure 2.6. Packing of molecules in complex **3** as viewed along the *b*-axis. H-atoms omitted for clarity. H-bonding can be seen between H-atom on N2 and ClO_4^- ion. Mn = pink, C = gold, N = blue, O = red, Cl = green.

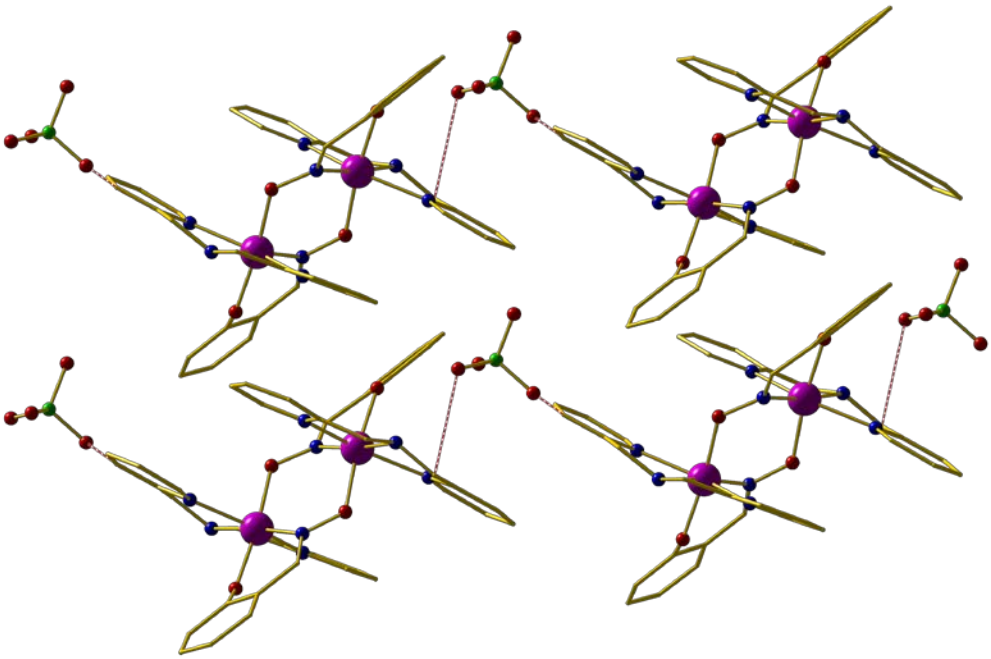

Figure 2.7. Packing of molecules in complex **4** as viewed along the *b*-axis. H-atoms omitted for clarity. H-bonding can be seen between H-atoms on N2 and ClO_4^- ion.

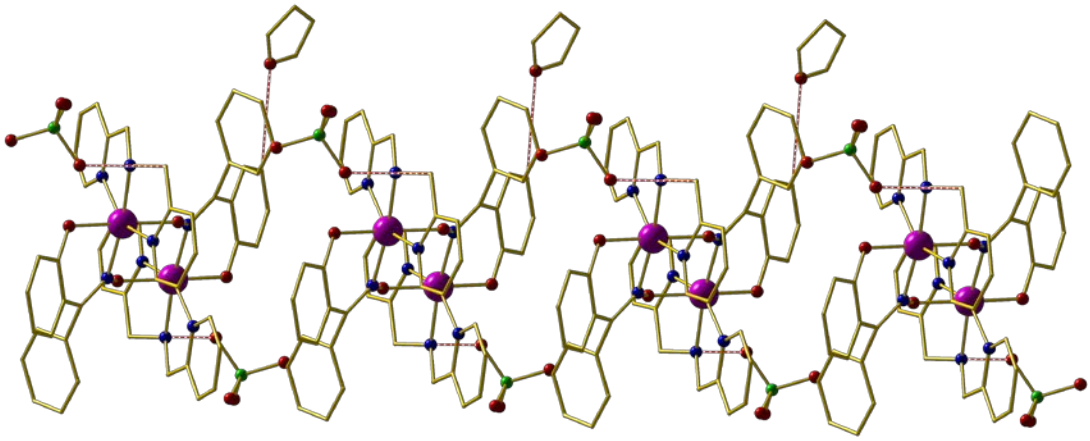

Figure 2.8. Packing of molecules in complex **5** as viewed along the *b*-axis. H-atoms omitted for clarity. H-atoms can be seen between ClO_4^- ion and C25, and also between THF solvent and C4. Mn = pink, C = gold, N = blue, O = red, Cl = green.

SQUID Magnetometry

Dc magnetic susceptibility measurements were performed on polycrystalline samples of **1**-**3** and **5** in the temperature range T = 5 - 300 K in an applied magnetic field of B = 0.1 T. The poor yield of complex **4** precluded measurement. The experimental results are shown in the form of $\chi_M T$ products *vs* T, where χ_M is the molar magnetic susceptibility, along with the data for complexes **6** and **7**.[22] At the highest temperatures measured the $\chi_M T$ values for **1**-**3** and **5** are ~4.1, 4.7, 4.8 and 5.0 cm^3 K mol^{-1}, respectively, all somewhat lower than that expected for two non-interacting, high spin d^4 ions with g = 2 (6 cm^3 K mol^{-1}). Upon cooling the $\chi_M T$ products of each sample behave very similarly, slowly decreasing with decreasing temperature reaching values of ~0.2 (**1**), 0.7 (**2**), 0.2 (**3**) and 1.1 cm^3 K mol^{-1} (**5**) at T = 5 K, indicative of the presence **o**f weak antiferromagnetic exchange between the two Mn^{III} ions. This is in stark contrast to observations for complexes **6** and **7** which displayed weak ferromagnetic exchange, as discussed in the articles highlighted in reference 22.

$$\hat{H} = \mu_B B \sum_i g_i \hat{S}_i - 2 \sum_{i,j<i} J_{ij} \hat{S}_i \cdot \hat{S}_j \quad (1)$$

The data can be fitted (Figure 2.9 and Table 2.3) to the model described by the isotropic spin-Hamiltonian (1), where the indices i and j refer to the two Mn^{III} centres, J is the isotropic exchange interaction parameter, $\hat{S}$ is a spin operator, μ_B is the Bohr magneton, B is the applied magnetic field vector and g =1.98 is the g-factor of the Mn^{III} ions. The best-fit parameters are J = -5.73 cm^{-1} (**1**), -3.63 cm^{-1} (**2**), -5.63 cm^{-1} (**3**) and -2.05 cm^{-1} (**5**). The ground spin-state of all four complexes is a spin singlet (S = 0; energy versus spin state plots are shown in Figures 2.10-2.13). This can be compared to the S = 4 ground states observed for complexes **6** and **7** resulting from exchange interactions of +2.20 and +1.24 cm^{-1}, respectively. The difference between the magnetic behaviour of **1**-**3, 5** and **6**-**7** is intriguing, particularly given they have the same $[Mn(NO)]_2$ magnetic core, and thus it would

appear that the orientation of the JT axes is an important structural parameter. In order to examine this in more detail we have therefore turned to DFT.

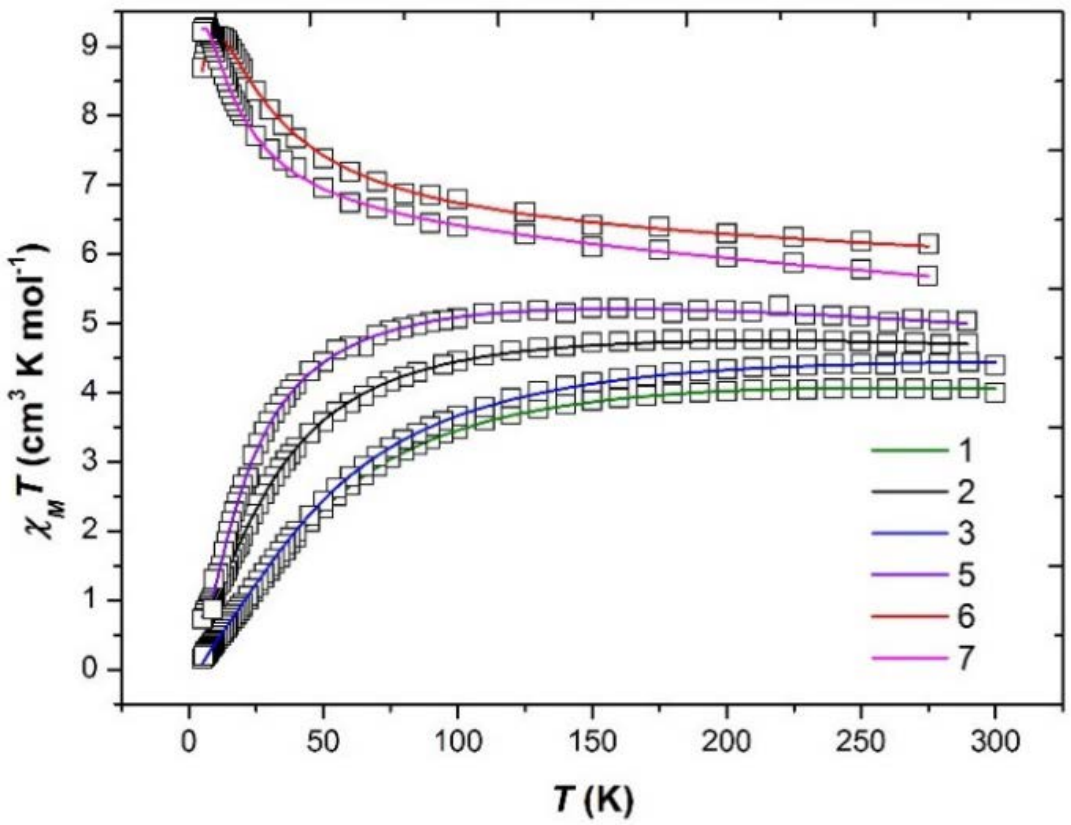

Figure 2.9. Plot of $\chi_M T$ product versus T for complexes 1-3, 5-7. The solid lines are a fit of the experimental data to isotropic spin-Hamiltonian (1). See text for details of the best fit parameters. Green = **1**, black = **2**, blue = **3**, purple = **5**, red = **6** and pink = **7**.

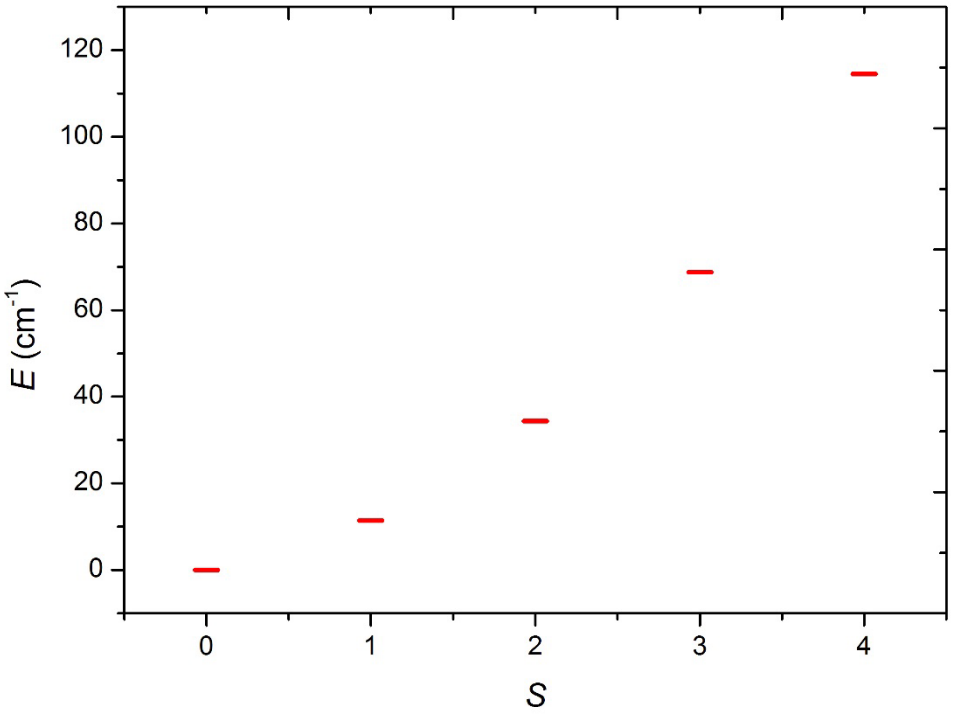

Figure 2.10. Energy spectrum of **1** at zero magnetic field for the isotropic spin-Hamiltonian (1) with the determined best fit parameters as described in the main text.

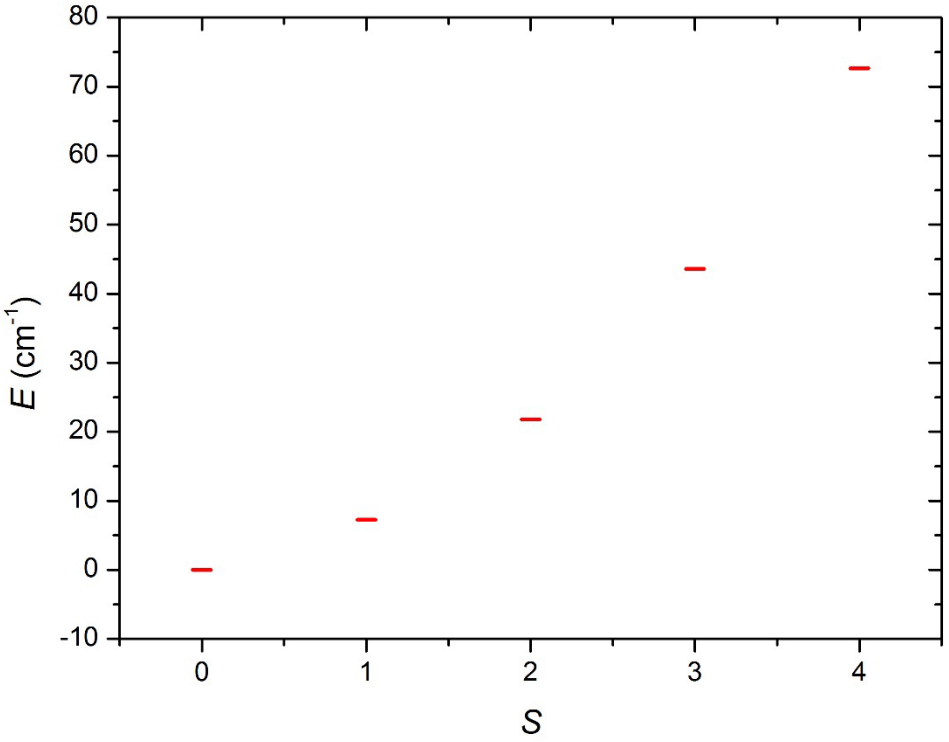

Figure 2.11. Energy spectrum of **2** at zero magnetic field for the isotropic spin-Hamiltonian (1) with the determined best fit parameters as described in the main text.

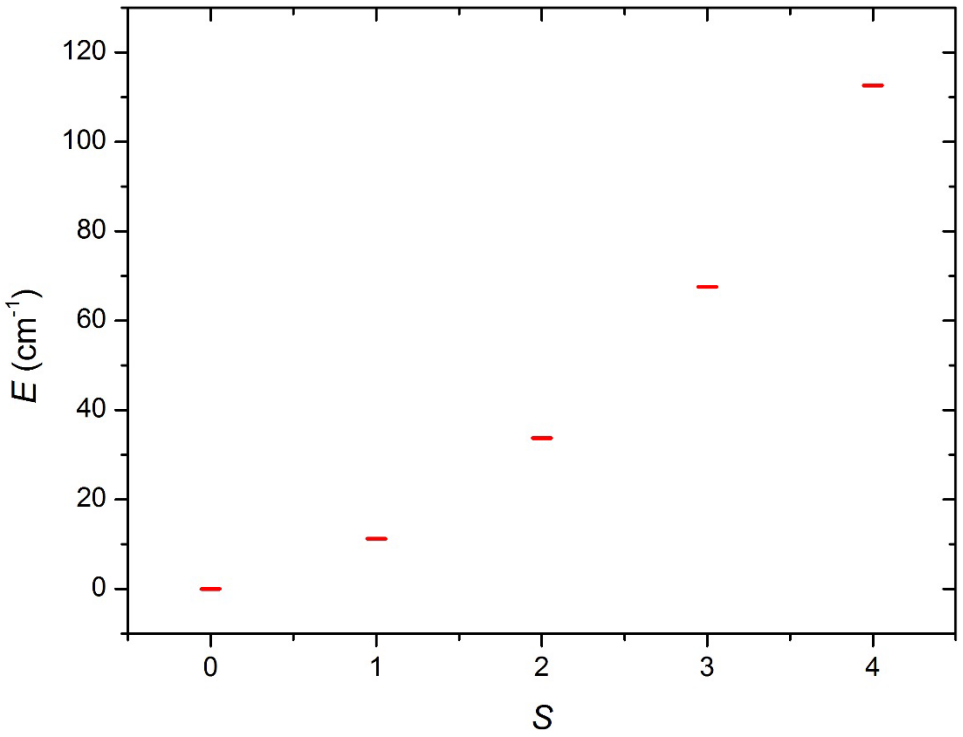

Figure 2.1. Energy spectrum of **3** at zero magnetic field for the isotropic spin-Hamiltonian (1) with the determined best fit parameters as described in the main text.

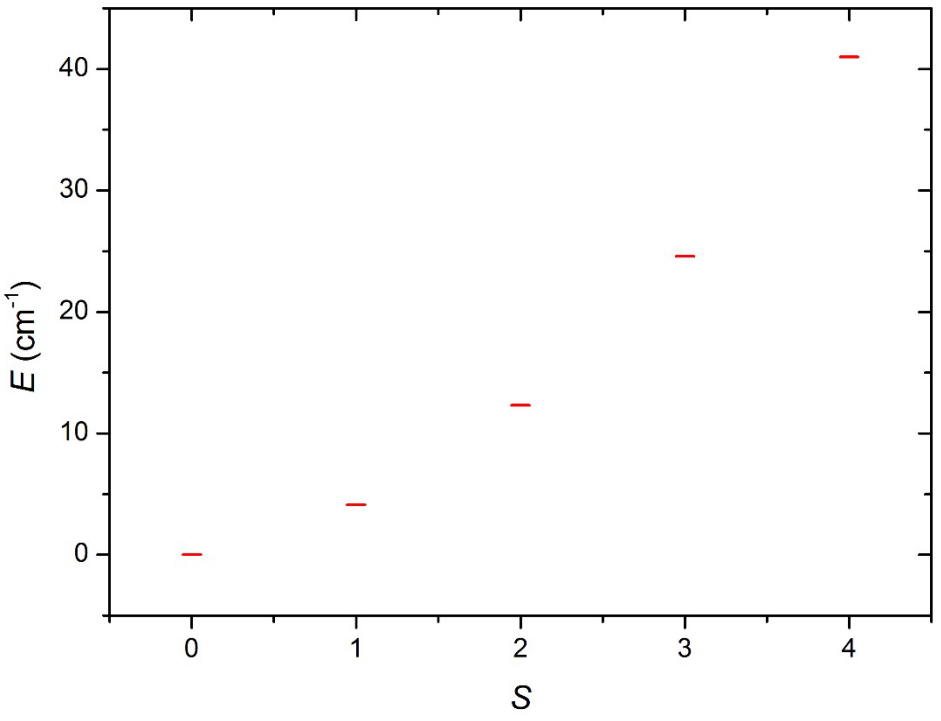

Figure 2.13. Energy spectrum of **5** at zero magnetic field for the isotropic spin-Hamiltonian (1) with the determined best fit parameters as described in the main text.

Table 2.3. Summary of pertinent experimentally derived magneto-structural parameters for the $[Mn(NO)]_2$ family of complexes. Theoretically calculated J values for **1**-**6** are given in parentheses.

Structure	Type	Mn-N-O-Mn torsion angle (°)	J (cm^{-1})
1	C	78.75	-5.73
			(-5.76)
2	C	64.59	-3.63
			(-2.16)
3	C	74.90	-5.63
			(-5.15)
5	C	63.00	-2.05
			(-2.99)
6	B	75.21	+2.20
7	B	80.28	+1.24

Theoretical Studies

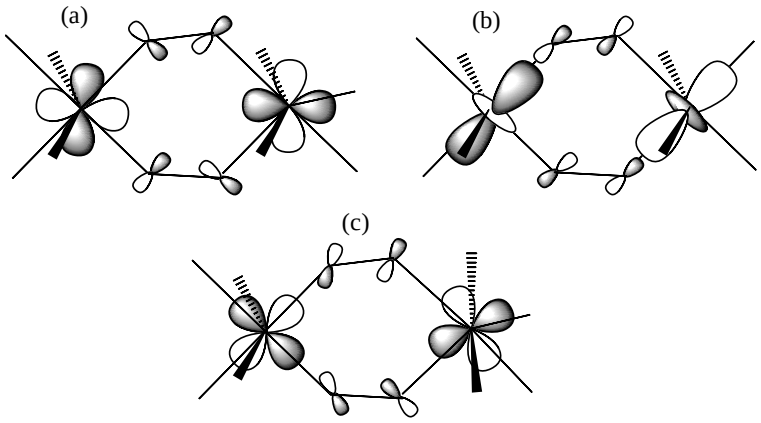

Figure 2.2. Schematic representation of the (a) d_{xy}-d_{xy} overlap in complexes 1-5, (b) d_z^2-d_z^2 overlap in complex **6**, (c) cross-interaction between d_x^2-$_y^2$ and d_{xz} in complexes **1**-**6**.

Theoretical studies have been carried out on complexes **1**-**6** in order to evaluate the exchange parameters and to reveal the mechanism of exchange. The

DFT computed J values for complexes **1**-**6** are -5.76 cm^{-1}, -2.16 cm^{-1}, -5.15 cm^{-1}, -3.66 cm^{-1}, -2.99 cm^{-1} and +2.65 cm^{-1}, respectively. Complexes **1**-**5** are found to exhibit weak antiferromagnetic exchange interactions, while complex **6** exhibits ferromagnetic exchange. Calculations reproduce not only the sign of J accurately but also their magnitude and the trend in magnitudes compared to that observed experimentally. To understand the electronic reasons behind the variation in the nature and magnitude of exchange, and to analyse the effect of the relative orientation of the JT axis (structure types **B** and **C**), molecular orbitals (MO) and overlap integrals have been analysed for complexes **1**-**6**. The net exchange interaction in the dinuclear Mn^{III} moiety has two contributions: (i) an antiferromagnetic J_{AF} contribution arising solely from overlap between the singly occupied MOs (SOMOs) of the Mn^{III} ions, and (ii) a ferromagnetic J_F contribution arising from the orthogonality of the SOMOs (negligible overlap) and from the cross-interaction[22b,c] between the empty and the occupied *d*-orbitals (here between the $d_{x^2-y^2}$ and all the other Mn^{III} *d*-orbitals). Amongst the structures studied, the major contributor to the J_{AF} term is the overlap between the d_{xy} orbitals *via* the oxime bridge. This contribution is significant for complexes **1**-**5** possessing type **C** structures, as indicated in Figure 2.1 and Figure 2.14a. The second dominant contribution to the J_{AF} term is the d_{xz}-d_{xz} overlap, also routed through the Mn-N-O-Mn bridge. Thus for complexes **1**-**5** the Mn-N-O-Mn torsion angle clearly dictates the strength of orbital overlap and the J value. These two overlaps are expected to be minimal in complex **6**, resulting in a very small J_{AF} term. However as the JT axes are now oriented along the oxime bridges, this allows for efficient d_{z^2}-d_{z^2} overlap (see Figure 2.14b). In this scenario the latter overlap is dominant and this contributes to the J_{AF} term. As shown in Figure 2.14b, this overlap is also strongly dependent upon the Mn-N-O-Mn torsion angle, with negligible overlap expected when the torsion angle approaches zero. Apart from these three prominent interactions, other orbital overlap values are small suggesting orthogonality between the SOMOs and a contribution to the J_F term. Along with moderate cross-interactions ($d_{x^2-y^2}$-d_{xz}) this leads to a significant J_F term for all complexes **1**-**6**. The

sign of *J* in each case is dictated by the dominant factor; for **1**-**5** the two strong overlaps overwhelmingly dominate leading to net antiferromagnetic exchange, while the prominent d_z^2-d_z^2 overlap observed in complex **6** is overshadowed by the J_F contributions leading to a net ferromagnetic interaction.

Spin density plots were computed in order to understand the origin of the electronic differences in complexes **1**-**6**. Unpaired electrons in t_{2g} orbitals usually favour a spin polarisation mechanism, whereas those in the e_g orbitals tend to facilitate a spin delocalisation mechanism. In the case of the Mn^{III} ion therefore a mixture of these two mechanisms is found to operate since the ion possesses three unpaired electrons in the t_{2g} orbitals and one unpaired electron in the e_g orbital. The spin density of the Mn^{III} ions in **1**-**6** is found to be < 3.8 which shows that it is centred on the metal ion with a dominant spin delocalisation mechanism. The bridging N and O spin densities are different for the two structure types studied; for complex **1** all the bridging N and O atoms possess negative spin density indicating spin polarization, while complex **6** possesses positive spin density on the O atom due to spin delocalisation as it lies along the JT axis (see Figure **2.14**) and negative spin density on the N atom due to spin polarization.

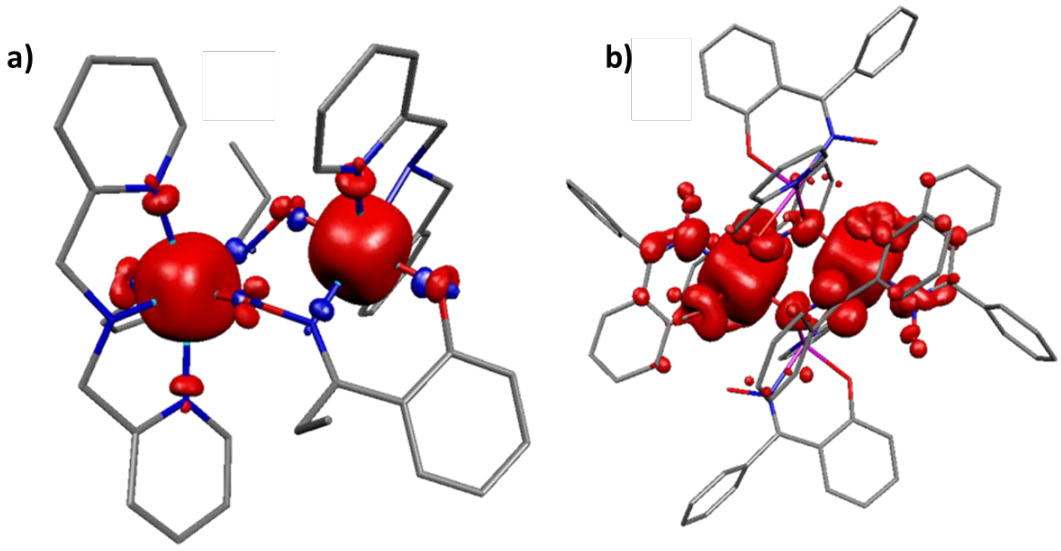

Figure 2.3. Computer spin density HS plot for complex **1** (a) and complex **6** (b).

Apart from the orientation of the JT axis, the Mn-N-O-Mn torsion angle also plays a role in dictating the sign and magnitude of the *J* values. To see if it is possible to obtain ferromagnetic coupling in type **C** structures, we have developed MSCs by varying the Mn-N-O-Mn torsion angle from 18.5 to 92.8° in complex **1**. A plot of *J* versus Mn-N-O-Mn torsion angle is shown in Figure 2.16. Our correlation reveals that *J* switches its sign from antiferromagnetic to ferromagnetic with decreasing torsion angle. As the torsion angle decreases, the cross-interaction between $d_{x^2-y^2}$ and d_{xz}/d_{xy} strengthens, leading to a larger J_F contribution, which in turn results in ferromagnetic exchange. Our calculations predict that a more planar Mn-N-O-Mn moiety of structure type **C** will exhibit ferromagnetic exchange coupling. Synthetic efforts to produce such a molecule are underway in our laboratory.

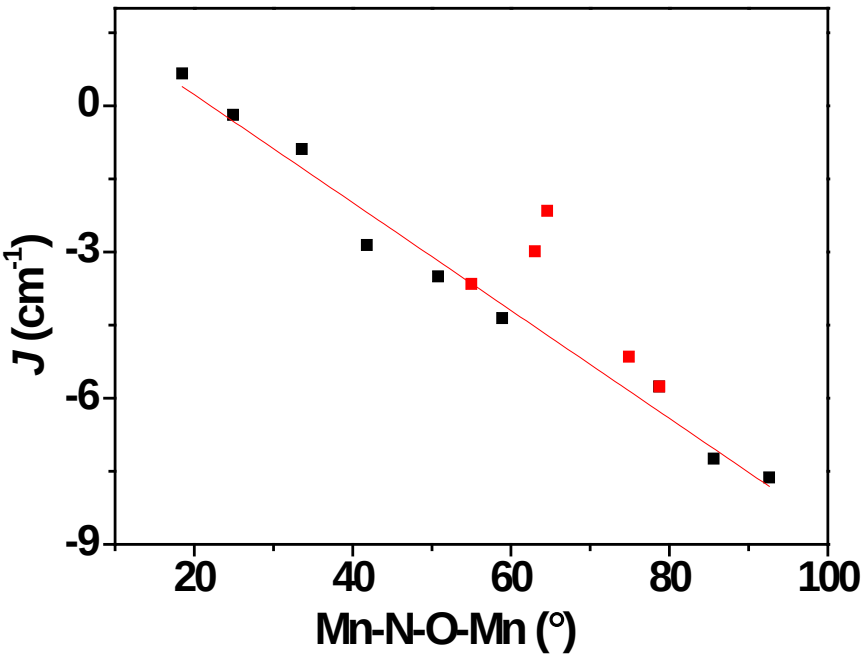

Figure 2.4. MSCs developed by varying the Mn-N-O-Mn torsion angle in **1**. The red squares are experimental *J* values obtained for complexes **1**-**5**.

2.4 Conclusions

The simple reaction between a Mn salt, a phenolic oxime and the tridentate chelate dpa affords a small family of double-oxime bridged Mn^{III} dimers, whose structures differ from previous examples in the orientation of their JT axes. Previous family members conform to structure type **B** with the JT axes co-parallel and in the bridging plane between the Mn^{III} ions, resulting in ferromagnetic exchange. The addition of a chelating ligand results in the novel complexes **1**-**3**, **5** whose JT axes have now switched orientation giving structure type **C**, where they lie perpendicular to the $[Mn(ON)]_2$ bridging plane. The result is that the magnetic exchange between the metal centres becomes weakly antiferromagnetic. The employed DFT methodology is able to reproduce both the sign and magnitude of the exchange interaction in complexes **1**-**6**. MO analysis reveals two dominant overlaps between the d_{xy}-d_{xy} and d_{xz}-d_{xz} orbitals, which are found to control the sign and magnitude of exchange in complexes **1**-**5**. In the case of complex **6**, strong d_z^2-d_z^2 overlap is overcome by cross-interactions and orbital orthogonality resulting in a weak ferromagnetic interaction. The general mechanism of exchange proposed can, in principle, be extended to any double oxime bridged Mn^{III} dimer. Our developed MSC suggests a switch in the sign of the exchange interaction from antiferromagnetic to ferromagnetic upon decreasing the Mn-N-O-Mn torsion angle to approximately 20**°.**

2.5 References

1. D. Gatteschi, R. Sessoli and J. Villain, *Molecular Nanomagnets*, Oxford University Press: Oxford, U.K., 2006.
2. J. M. Clemente-Juan, E. Coronado and A. Gaita-Ariño, *Chem. Soc. Rev*., 2012, **41**, 7464.
3. L. Bogani and W. Wernsdorfer, *Nature Materials*, 2008, **7**, 179.
4. M. N. Leuenberger and D. Loss, *Nature,* 2001, **410**, 789.
5. M. Evangelisti, in *Molecular Magnets*, NanoScience and Technology, J. Bartolomé, F. Luis, J. F. Fernández, Springer-Verlag; Berlin, Heidelberg, 2014, pp. 365.
6. G. Aromí and E. K. Brechin, *Struct. Bond*., 2006, **122**, 1; C. J. Milios and R. E. P. Winpenny, *Struct. Bond*., 2015, **164**, 1.
7. W. Wernsdorfer and R. Sessoli, Science, 1999*,* **284***,*133.
8. S. Thiele, F. Balestro, R. Ballou, S. Klyatskaya, M. Ruben and W. Wernsdorfer, *Science*, 2014, **344**, 1135.
9. M. Ganzhorn, S. Klyatskaya, M. Ruben and W. Wernsdorfer, *Nature Nanotechnology*, 2013, 8, 165.
10. M. Urdampilleta, S. Klyatskaya, J-P. Cleuziou, M. Ruben and W. Wernsdorfer, *Nature Materials*, 2011, **10**, 502.
11. J.-P. Cleuziou, W. Wernsdorfer, V. Bouchiat, T. Ondarçuhu and M. Monthioux, *Nature Nanotechnology*, 2006, **1**, 53.
12. M. Baker, T. Guidi, S. Carretta, J. Ollivier, H. Mutka, H.-U Güdel, G. A. Timco, E. J. L. McInnes, G. Amoretti and R. E. P. Winpenny, *Nature Phys*., 2012, **8**, 906.
13. S. Hill, R. S. Edwards, N. Aliaga-Alcalde and G. Christou, *Science*, 2003, **302**, 1015.
14. W. Wernsdorfer, N. Aliaga-Alcalde, D. N. Hendrickson and G. Christou, *Nature*, 2002, **416**, 406.
15. J. D. Rinehart, M. Fang, W. J. Evans and J. R. Long, *J. Am. Chem. Soc.,* 2011, **133**, 14236.
16. S. Loth, S. Baumann, C.P. Lutz, D.M. Eigler and A. J. Heinrich, *Science,* 2012, **335**, 196.
17. M. Evangelisti, A. Candini, A. Ghirri, M. Affronte, E. K. Brechin and E. J. L. McInnes, *Appl. Phys. Lett.,* 2005, **87**, 072504; M. Evangelisti and E. K. Brechin, *Dalton Trans*., 2010, **39**, 4672.
18. M. Mannini, F. Pineider, C. Danielli, F. Totti, L. Sorace, P. Sainctavit, M-A. Arrio, E. Otero, L. Joly, J. C. Cezar, A. Cornia and R. Sessoli, *Nature*, 2010, **468**, 417.

19. J. Lehmann, A. Gaita-Ariño, E. Coronado and D. Loss, *Nature Nanotechnology*, 2007, **2**, 312.
20. (a) J. Liu and S. Hill, *Polyhedron*, 2013, **66**, 147; (b) S. Hill, S. Datta, J. Liu, R. Inglis, C. J. Milios, P. L. Feng, J. J. Henderson, E. del Barco, E. K. Brechin and D. N. Hendrickson, *Dalton Trans*., 2010, **39**, 4693.
21. D. Gatteschi, O. Kahn and R. D. Willet, ed. *Magneto-Structural Correlations in Exchange-Coupled Systems*; D. Reidel: Dordrecht, 1985.
22. (a) D. A. Pantazis, V. Krewald, M. Orio and F. Neese, *Dalton Trans*., 2010, **39**, 4959; (b) N. Berg, T. Rajeshkumar, S. M. Taylor, E. K. Brechin, G. Rajaraman and L. F. Jones, *Chem. Eur. J*., 2012, **18**, 5906; (c) W. P. Barros, R. Inglis, G. S. Nichol, T. Rajeshkumar, G. Rajaraman, S. Piligkos, H. O. Stumpf and E. K. Brechin, *Dalton Trans*., 2013, **42**, 16510; (d) R. Inglis, E. Houton, J. Liu, A. Prescimone, J. Cano, S. Piligkos, S. Hill, L. F. Jones and E. K. Brechin*, Dalton Trans*., 2011, **40**, 9999; (e) E. Houton, S. M. Taylor, C. C. Beedle, J. Cano, S. Piligkos, S. Hill, A. G. Ryder, E. K. Brechin and L. F. Jones, *Dalton Trans*., 2012, **41**, 8340.
23. C. J. Milios, R. Inglis, L. F. Jones, S. Piligkos and E. K. Brechin, *Chem. Commun*., 2012, **48**, 181; C. J. Milios, S. Piligkos and E. K. Brechin, *Dalton Trans*., 2008, 1809.
24. W. R. Dunstan and T. A. Henry, *J. Chem Soc. Trans*., 1899, **75**, 66.
25. (a) P. W. Betteridge, J. R. Carruthers, R. I. Cooper, K. Prout and D. J. Watkin, *J. Appl Crystallogr*., 2003, **36**, 1487; (b) O. V. Dolomanov, L. J. Bourhis, R. J. Gildea, J. A. K. Howard, H. Puschmann, *J. Appl. Cryst*., 2009, **42**, 339.
26. A. D. Becke, *J. Chem. Phys*., 1993, **98**, 5648
27. (a) A. Schafer, H. Horn and R. Ahlrichs, *J. Chem. Phys.,* 1992, **97**, 2571; (b) A. Schafer, C. Huber and R. Ahlrichs, *J. Chem. Phys*., 1994, **100**, 5829.
28. M. J. Frisch, G. W. Trucks, H. B. Schlegel, G. E. Scuseria, M. A. Robb, J. R. Cheeseman, G. Scalmani, V. Barone, B. Mennucci, G. A. Petersson, H. Nakatsuji, M. Caricato, X. Li, H. P. Hratchian, A. F. Izmaylov, Bloino, G. Zheng, J. L. Sonnenberg, M. Hada, M. Ehara, K. Toyota, Fukuda, J. Hasegawa, M. Ishida, T. Nakajima, Y. Honda, O. Kitao, H. Nakai, T. Vreven, J. A. Montgomery Jr., J. E. Peralta, F. Ogliaro, M. Bearpark, J. J. Heyd, E. Brothers, K. N. Kudin, V. N. Staroverov, R. Kobayashi, J. Normand, K. Raghavachari, A. Rendell, J. C. Burant, S. S. Iyengar, J. Tomasi, M. Cossi, N. Rega, J. M. Millam, M. Klene, J. E. Knox, J. B. Cross, V. Bakken, C. Adamo, J. Jaramillo, R. Gomperts, R. E. Stratmann, O. Yazyev, A. J. Austin, R. Cammi, C. Pomelli, J. W. Ochterski, R. L. Martin, K. Morokuma, V. G. Zakrzewski, G. A. Voth, P. Salvador, J. J. Dannenberg, S. Dapprich, A. D. Daniels, O. Farkas, J. B. Foresman, J. V. Ortiz, J. Cioslowski and D. J. Fox, GAUSSIAN 09 (Revision A.02), Gaussian, Inc., Wallingford, CT, 2009.

29. L. Noodleman, *J. Chem. Phys.,* 1981, **74**, 5737.

30. (a) E. Ruiz, S. Alvarez, J. Cano and P. Alemany, *J. Comput. Chem.,* 1999, **20**, 1391; (b) E. Ruiz, A. Rodriguez-Fortea, J. Cano, S. Alvarez and P. Alemany, *J. Comput. Chem.*, 2003, **24**, 982; (c) G. Rajaraman, J. Cano, E. K. Brechin and E. J. L. McInnes, *Chem. Commun.,* 2004, 1476; (d) P. Christian, G. Rajaraman, A. Harrison, J. J. W. McDouall, J. Raftery and R. E. P. Winpenny, *Dalton Trans.,* 2004, 2550; (e) G. Rajaraman, M. Murugesu, E. C. Sanudo, M. Soler, W. Wernsdorfer, M. Helliwell, C. Muryn, J. Raftery, S. J. Teat, G. Christou and E. K. Brechin, *J. Am. Chem. Soc.,* 2004, **126**, 15445; (f) S. Sasmal, S. Hazra, P. Kundu, S. Dutta, G. Rajaraman, E. C. Sañudo and S. Mohanta, *Inorg. Chem.,* 2011, **50**, 7257; (g) L. F. Jones, G. Rajaraman, J. Brockman, M. Murugesu, J. Raftrey, S. J. Teat, W. Wernsdorfer, G. Christou, E. K. Brechin, D. Collison, *Chem. Eur. J.* 2004, **10**, 5180.

Chapter 3

Modular $[Fe^{III}M^{II}_6]^{12+}$and $[M^{III}_2M^{II}_3]^{n+}$ cages

3.1 Introduction

Fe^{III} is relevant in several areas of science, from mineralogy and biology to magnetic materials.[1,2,3,4] In molecular magnetism, although the majority of Fe^{III} complexes exhibit antiferromagnetic exchange, the possibility of a non-zero ground state (a prerequisite for slow relaxation of magnetisation and also enhanced magnetocaloric effect (MCE)) means that its complexes have been explored through the past several decades.[5,6,7] The earliest complexes and also the simplest were dinuclear Fe^{III} systems. Lippard and co-workers reported the first MSCs of Fe^{III} dimers in 1990.[8] The development of these studies of oxo-bridged dimers reported several determining factors in the nature of the exchange interaction, the most important being the shortest Fe-O distance. However, as published a few years later, this was not the only important parameter which would determine the exchange interactions of Fe^{III} dimers. Weihe and Güdel also showed the importance of the Fe-O-Fe bridging angle as well as the Fe-O bond distances.[9] Lippard also reported the interesting stepped magnetisation data of a molecular ferric wheel in 1994.[10] It was not until 2 years later that the first Fe^{III} complex, an [Fe_8] system exhibiting slow relaxation of magnetisation (SMM) was reported.[11,12] As with the first ever reported SMM, [Mn_{12}OAc], the magnetic properties were only reported 10 years after the original structure of [Fe_8]. Shortly after this, A family of propeller shaped [Fe_4] SMMs were reported, exhibiting antiferromagnetic behaviour and an S = 5 ground state.[13] Furthermore, the synthesis of the [Fe_{17}]/[Fe_{19}] structures that crystallised in the same unit cell, whose core represented a mineral-like iron oxy/ hydroxide structure. This suggested that molecular version of magnetically interesting natural materials could be developed in the lab.[14] The same can also be said for another [Fe_{17}] structure, synthesised by Brechin and co-workers, which contains a portion of the magnetite lattice and can act as a magnetic refrigerant.[15,16,17] Similar behaviour was also observed for an [Fe_{14}] system which showed the largest MCE for any material below 10 K at the time of publication.[18] The complex exhibited spin frustration due to competing antiferromagnetic interactions dictated by the high symmetry hexacapped, hexagonal bipyramidal

structure. Another heavily studied cage is the $\{Mo_{72}Fe_{30}\}$ polyoxometalate (POM). The geometrically frustrated icosidodecahedron is a molecular version of a kagome lattice and displays several fascinating properties, including spin freezing and slow dynamins suggestive of spin glass behaviour.[19]

The advantages of mixed-metal frameworks in molecular magnetism stem from the goals of building systems with large spin-ground states.[20,21],[22] A CCDC search shows that the literature contains over 3000 Fe- based heterometallic cages. Strategies for building such systems can take the so-called "bottom-up" approach and often involve using building blocks.[23,24,25] Rigid metalloligands, acting as donor units, can offer an efficient and selective method towards the formation of predetermined heterometallic systems.[26,27,28,29,30]. This, in turn, can be used to control and tune the magnetic properties. Herein we present the construction of seven novel heterometallic- Fe^{III} cages, using a pre-made metalloligand.

The novel heterometallic cages $[Fe^{III}_8Pd^{II}_6L_{24}](OTf)_{12}$ (**1**), $[Fe^{III}_8Cu^{II}_6L_{24}Br_6]Br_6$ (**2**), $[Fe^{III}_8Cu^{II}_6L_{24}](NO_3)_{12}$ (**3**), $[Fe^{III}_8Ni^{II}_6L_{24}(SCN)_{11}Cl]$ (**4**), $[Fe^{III}_8Co^{II}_6L_{24}(SCN)_{10}(H_2O)_2](SCN)_2$ (**5**), $[Fe_2Co_3L_6Cl_6]$ **(6)** and $[Fe_2Zn_3L_6Br_6]$ **(7)** are constructed from $[Fe^{III}L_3]$ (where HL = 1-(4-pyridyl)butane-1,3-dione) and simple palladium, copper, nickel, cobalt and zinc salts. Complexes **1**-**5** take the shape of cubes whilst **6** and **7** are of trigonal bipyramidal geometry. The synthesis, structural and magnetic characterisation of the novel complexes are discussed below.

3.2 Experimental

Materials and physical measurements

All synthetic procedures were performed under aerobic conditions using chemicals as received (reagent grade). 1-(4-pyridyl)butane-1,3-dione (HL) was prepared by published procedures.[31] Variable temperature, solid state magnetic susceptibility data down to 2 K were collected on a Quantum Design MPMS XL SQUID magnetometer equipped with a 7 T dc magnet (compound **6** was measured using a 5 T dc magnet). Diamagnetic corrections were applied to the observed paramagnetic susceptibilities using Pascal's constants. X band (9 GHz) and Q band

(35 GHz) EPR measurements were carried out in their entirety by Professor Eric McInnes and Dr. Nicholas Chilton, at the University of Manchester.

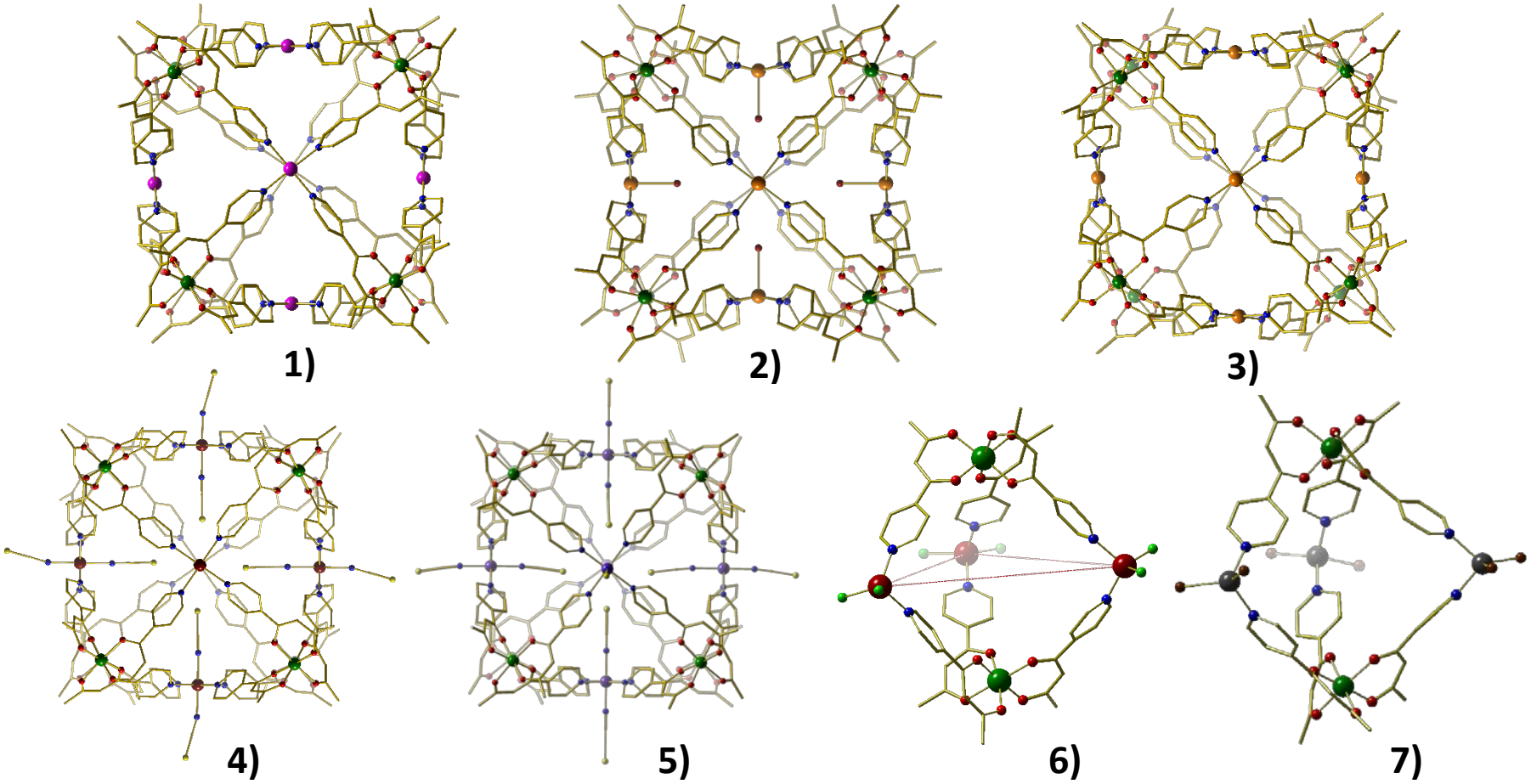

Figure 3.1. Molecular structures of complexes **1**-**7**. Fe = dark green, Pd = pink, Cu = orange, Ni = purple, Co = dark red, Zn = grey, C = gold, N = blue, O = bright red, S = yellow, Br = dark brown, Cl = bright green. H atoms removed for clarity.

Synthesis

$[Fe^{III}L_3]$: $FeCl_3$ (0.162 g, 1 mmol), 1-(4-pyridyl)butane-1,3-dione (0.57 g, 3.5 mmol) and NaOMe (0.189 g, 3.5 mmol) were dissolved in 100 mL of MeOH/H_2O (1:1, 25 mL) and left to stir until a red product precipitated (~24 h). The resultant red precipitate was filtered and washed with water. The crude product was extracted with $CHCl_3$ and dried over anhydrous $MgSO_4$. The $CHCl_3$ was removed under reduced pressure to afford the product as a red solid. Elemental analysis (%) calculated (found): C 59.79 (59.53), H 4.46 (4.39), N 7.75 (7.67).

$[Fe^{III}_8Pd^{II}_6L_{24}](OTf)_{12}$ (1): A solution of AgOTf (0.042 g, 0.166 mmol) and [Pd(benzonitrile)$_2$Cl$_2$] (0.032 g, 0.083 mmol) in DCM (10 mL) was stirred for 30 minutes. The solution was then filtered, and added to a solution of $[Fe^{III}L_3]$ (0.030 g, 0.055 mmol) in MeOH/ DCM (1:1, 10 mL). Red rod-like X-ray quality crystals were obtained by slow evaporation of the mother liquor. Elemental analysis (%) calculated (found): C 40.47 (40.31), H 2.86 (2.71), N 4.97 (5.12).

$[Fe^{III}_8Cu^{II}_6L_{24}Br_6]Br_6$ (2): $[Fe^{III}L_3]$ (0.108 g, 0.2 mmol) in DCM (10 mL) was added to a solution of $CuBr_2$ (0.045 g, 0.2 mmol) in MeOH (10 mL). The mixture was stirred for 3 hours before being filtered. Black block-shaped crystals formed from slow evaporation of the mother liquor after two days. Elemental analysis (%) calculated (found): C 47.29 (47.01), H 3.50 (3.24) N 6.13 (6.04).

$[Fe^{III}_8Cu^{II}_6L_{24}](NO_3)_{12}$ (3): $[Fe^{III}L_3]$ (0.1 mmol, 0.054 g), $Cu(NO_3)_2.3H_2O$ (0.024 g, 0.1 mmol) and pyrazine (0.032 g, 0.1 mmol) were dissolved in a solution of DCM and EtOH (1:1, 10 mL). The reaction mixture was stirred for 3 hours, before being filtered. Red prism-shaped crystals were obtained from slow evaporation of the mother liquor after 2 days. Elemental analysis (%) calculated (found) for: C 51.07 (51.86), H 3.80 (3.78), N 9.92 (9.84).

$[Fe^{III}_8Ni^{II}_6L_{24}(SCN_{11})Cl]$ (4): $NiCl_2$ (0.2 mmol) and $[Fe^{III}L_3]$ (0.108 g, 0.2 mmol) were stirred in a mixture of DCM and MeOH (1:1, 10 mL). After 20 minutes, KSCN (0.019 g, 0.2 mmol), dissolved in H_2O (2 mL) was added to the reaction mixture. The reaction was filtered after 30 minutes. Red prism- shaped crystals were obtained by

slow evaporation of the mother liquor after 4 days. Elemental analysis (%) calculated (found): C 50.82 (50.13), H 3.61 (3.70), N 9.14 (9.27).

$[Fe^{III}_8Co^{II}_6L_{24}(SCN_{10})(H_2O)_2](SCN)_2$ (5): $[Fe^{III}L_3]$ (0.108 g, 0.2 mmol) in DCM (10 mL) was added to a solution of $Co(SCN)_2$ (0.045 g, 0.2 mmol) in MeOH (10 mL). The mixture was stirred for 2 hours before being filtered. Black block-shaped crystals formed from slow evaporation of the mother liquor after three days. Elemental analysis (%) calculated (found): C 50.35 (50.41), H 3.63 (3.70), N 9.27 (9.01).

$[Fe_2Co_3L_6Cl_6]$ (6): To a solution of the metalloligand $[Fe^{III}L_3]$ (0.108 g, 0.2 mmol) in acetone (35 mL), was added $CoCl_2$ (0.039 g, 0.3 mmol). The resultant mixture was stirred for 30 minutes, before being filtered and layered with Et_2O. Orange, plate-shaped X-ray quality crystals were obtained after 20 days. Elemental analysis (%) calculated (found) C: 44.00 (44.12), H: 3.28 (3.39), N: 5.70 (5.77).

$[Fe_2Zn_3L_6Br_6]$ (7): To a solution of the metalloligand $[Fe^{III}L_3]$ (0.108 g, 0.2 mmol) in a mixture of DCM and acetone (1:1, 17 mL), $ZnBr_2$ (0.067 g, 0.3 mmol) was added. The solution was stirred for 30 minutes, before being evaporated to dryness. The dark-red product was re-dissolved in $MeNO_2$, filtered and allowed to stand. Dark-red, prism-shaped X-ray quality crystals were obtained after room temperature evaporation of the mother liquor for 10 days. Elemental analysis (%) for calculated (found) C: 36.85 (36.97), H: 2.75 (2.87), N: 4.77 (4.91).

X-Ray Crystallography

For compounds **1**, **2**, **4** and **5**-**7** single-crystal X-ray diffraction data were collected at *T* = 100 K on a Rigaku AFC12 goniometer equipped with an enhanced sensitivity (HG) Saturn 724+ detector mounted at the window of an FR-E+ Superbright MoKα rotating anode generator with HF Varimax optics (70 μm focus)[32] using Rigaku Crystal Clear and CrysalisPro software[33,34] for data collection and reduction. For **3**, single-crystal X-ray diffraction data were collected at T = 30.15 K using a synchrotron source at Diamond Light Source I-19 beam line, however the same software as above was used for data refinement. Unit cell parameters in all

cases were refined against all data. Crystal structures were solved using the charge flipping method implemented in SUPERFLIP[35] or by direct methods with ShelXS. All structures were refined on F_o^2 by full-matrix least-squares refinements using ShelXL[36] within the OLEX2 suite.[37] All non-hydrogen atoms were refined with anisotropic displacement parameters, and all hydrogen atoms were added at calculated positions and refined using a riding model with isotropic displacement parameters based on the equivalent isotropic displacement parameter (U_{eq}) of the parent atom. All five structures contain accessible voids and channels that are filled with diffuse electron density belonging to uncoordinated solvent. The SQUEEZE routine of PLATON was used to remove remaining electron density corresponding to solvent and anions not reported in the calculated formula.

Table 3.1a. Selected crystallographic information for complexes [FeL_3], **1** and **2**.

Identification code	**[FeL_3]**	**1**	**2**
Empirical Formula	$C_{27}H_{24}FeN_3O_{10}$	$C_{216}H_{194}Cl_4Fe_8N_{24}O_{54}Pd_6$	$C_{216}H_{192}Br_4Cu_6Fe_8N_{24}O_{52}$
Temperature	100(2) K	100(2) K	293(2) K
Wavelength	0.71075 Å	0.71075 Å	0.71075 Å
Crystal system	Trigonal	Orthorhombic	Tetragonal
Space group	*P*–3	*Pcca*	P4/nnc
***a* (Å)**	14.8322(3)	30.4249(5) Å	20.076(3)
***b* (Å)**	14.8322(3)	31.3338(4) Å	20.076(3)
***c* (Å)**	7.5892(3)	38.6462(5) Å	37.225(3)
α (°)	90	90	90
β (°)	90	90	90
γ (°)	120	90	90
Volume (Å^3)	1445.89(9)	36842.5(9)	15003(5)
Z	2	4	2
Density (calculated)	1.393 Mg / m^3	0.941 Mg / m^3	1.130
Absorption coefficient	0.581 mm^{-1}	0.669 mm^{-1}	1.383
F(000)	626	10568	5188
Crystal	Column; red	Prism; dark red	red block
Crystal size (mm^3)	0.5 × 0.05 × 0.05	0.09 × 0.08 ×0.06	0.09 x 0.08 x 0.03
θ range for data collection	1.585 – 29.957°	1.554 – 27.511°	2.985 – 27.482°
Index ranges	$-20 \le h \le 20$, $-20 \le k \le 20$, $-9 \le l \le 10$	$-18 \le h \le 39$, $-27 \le k \le 40$, $-50 \le l \le 50$	$-21 \le h \le 26$, $-26 \le k \le 21$, $-27 \le l \le 48$
Reflections collected	27017	197847	95000
Independent reflections	2666 [R_{int} = 0.0626]	42278 [R_{int} = 0.0780]	8612 [R_{int} = 0.1407]
Completeness to θ = 25.121°	100.0 %	100.0 %	99.8 %
Absorption correction	Semi–empirical from equivalents	Semi–empirical from equivalents	Semi-empirical from equivalents
Max. and min. transmission	1.00000 and 0.63936	1.00000 and 0.75019	1.000 and 0.233
Refinement method	Full-matrix least-squares on F^2	Full-matrix least-squares on F^2	Full-matrix least-squares on F^2

Data / restraints / parameters	2666 / 0 / 125	42278 / 2736 / 1418	8612 / 0 / 353
Goodness-of-fit on F^2	1.072	1.077	1.123
Final *R* indices [$F^2 > 2\sigma(F^2)$]	*R1* = 0.0655, *wR2* = 0.1855	*R1* = 0.0790, *wR2* = 0.2685	R1 = 0.0998, wR2 = 0.3260
***R* indices (all data)**	*R1* = 0.0748, *wR2* = 0.1989	*R1* = 0.1236, *wR2* = 0.2846	R1 = 0.1453, wR2 = 0.3483
Extinction coefficient	n/a	n/a	n/a
Largest diff. peak and hole	1.505 and −0.773 e Å^{-3}	1.038 and −0.685 e Å^{-3}	2.745 and −3.195 e Å^{-3}

Table 3.2b. Selected crystallographic information for complexes **3**-**5**.

Identification code	3	4	5
Empirical Formula	$C_{216}H_{192}Cu_6Fe_8N_{24}O_{58}$	$C_{227}H_{192}ClFe_8N_{35}Ni_6O_{48}S_{11}$	$C_{230}H_{200}Cl_{16}Co_6Fe_8N_{34}O_{50}S_{10}$
Temperature	30.15 K	100(2) K	293(2) K
Wavelength	0.6889 Å	0.71075 Å	0.71073 Å
Crystal system	Orthorhombic	Tetragonal	Tetragonal
Space group	*Pcca*	*P*4/*n*	*P*4/*n*
a **(Å)**	29.6051(6)	29.644(12)	29.5218(3)
b **(Å)**	31.3962(4)	29.644(12)	29.5218(3)
c **(Å)**	38.0783(6)	26.851(10)	26.6262(5)
α **(°)**	90	90	90
β **(°)**	90	90	90
γ **(°)**	90	90	90
Volume (Å^3)	35393.3(10)	23596(21)	23205.8(7)
Z	4	2	2
Density (calculated)	0.916 Mg / m^3	0.755 Mg / m^3	0.848 Mg / m^3
Absorption coefficient	0.667 mm^{-1}	0.567 mm^{-1}	0.631 mm^{-1}
F(000)	10008	5504	6040
Crystal	Prism; red	Prism; red	Prism; red
Crystal size (mm^3)	0.15 × 0.15 × 0.1	0.12x0.07x0.3	0.27 × 0.12 × 0.1
θ **range for data collection**	2.829 – 24.208°	2.474 – 25.121°	1.577 – 29.889°
Index ranges	$-43 \le h \le 45$, $-47 \le k \le 45$, $-56 \le l \le 55$	$-35 \le h \le 35$, $-35 \le k \le 35$, $-19 \le l \le 32$	$-38 \le h \le 35$, $-41 \le k \le 39$, $-36 \le l \le 36$
Reflections collected	463483	91153	152412
Independent reflections	31234 [R_{int} = 0.2527]	21002 [R_{int} = 0.0862]	31165 [R_{int} = 0.0460]
Completeness to θ = 25.121°	97.5 %	99.5 %	100.0 %
Absorption correction	Semi–empirical from equivalents	Semi–empirical from equivalents	Semi–empirical from equivalents
Max. and min. transmission	1.00000 and 0.73782	1.000 and 0.784	1.00000 and 0.63704
Refinement	Full-matrix least-	Full-matrix least-squares	Full-matrix least-squares

method	squares on F^2	on F^2	on F^2
Data / restraints / parameters	31234 / 99 / 1425	21002 / 1661 / 791	31165 / 1590 / 820
Goodness-of-fit on F^2	1.085	1.107	1.257
Final *R* indices [$F^2 > 2\sigma(F^2)$]	*R1* = 0.1122, *wR2* = 0.3358	*R1* = 0.1010, *wR2* = 0.3280	*R1* = 0.1041, *wR2* = 0.3552
***R* indices (all data)**	*R1* = 0.1523, *wR2* = 0.3645	*R1* = 0.1386, *wR2* = 0.3513	*R1* = 0.1450, *wR2* = 0.3752
Extinction coefficient	n/a	n/a	n/a
Largest diff. peak and hole	1.616 and −0.732 e Å^{-3}	0.816 and −0.835 e Å^{-3}	1.143 and −1.031 e Å^{-3}

Table 3.3. Selected crystallographic information for complexes **6** and **7**.

Identification code	**6**	**7**
Formula weight	1474.20	1882.34
Temperature	100(2) K	100(2) K
Wavelength	0.71075 Å	0.71075 Å
Crystal system	Trigonal	Trigonal
Space group	$P322_1$	$P322_1$
a (Å)	12.7708(5)	12.8153(16)
b (Å)	12.7708(5)	12.8153(16)
c (Å)	39.0709(12)	38.817(5)
α (°)	90	90
β (°)	90°	90
γ (°)	120°	120
Volume (Å^3)	5518.5(5)	5520.9(16) Å^3
Z	3	3
Density (calculated)	1.333 Mg / m^3	1.698 Mg / m^3
Absorption coefficient	1.318 mm^{-1}	4.669 mm^{-1}
F(000)	2241	2778
Crystal	Plate; orange	Prism; deep red
Crystal size (mm^3)	0.05 × 0.02 × 0.01 mm^3	0.080 × 0.050 × 0.040
θ range for data collection	1.564 – 27.474°	2.114 – 27.510°
Index ranges	$-15 \le h \le 12$, $-7 \le k \le 16$, $-49 \le l \le 50$	$-16 \le h \le 16$, $-15 \le k \le 16$, $-43 \le l \le 50$
Reflections collected	21858	37756
Independent reflections	8331 [R_{int} = 0.1233]	8454 [R_{int} = 0.0641]
Completeness to θ = 25.121°	100.0 %	99.6 %
Absorption correction	Semi–empirical from equivalents	Semi–empirical from equivalents
Max. and min. transmission	1.00000 and 0.54446	1.000 and 0.523
Refinement method	Full-matrix least-squares on F^2	Full-matrix least-squares on F^2
Data / restraints /	8331 / 324 / 378	8454 / 32 / 403

parameters		
Goodness-of-fit on F^2	1.006	0.990
Final *R* indices [$F^2 > 2\sigma(F^2)$]	*R1* = 0.0647, *wR2* = 0.1692	*R1* = 0.0321, *wR2* = 0.0791
***R* indices (all data)**	*R1* = 0.0752, *wR2* = 0.1773	*R1* = 0.0366, *wR2* = 0.0804
Extinction coefficient	n/a	n/a
Largest diff. peak and hole	1.029 and −0.636 e Å^{-3}	0.698 d −0.598 e Å^{-3}

3.3 Results and Discussion

The metalloligand [$Fe^{III}L_3$] is formed through the reaction of $FeCl_3$, NaOMe and HL. The structure forms a regular octahedral geometry consisting of an {FeO_6} unit, where the facial angles range between 87° and 94° and the Fe-O bond distances are approximately 1.98 Å. Through coordination in the cages, the Fe^{III} ions maintain their octahedral geometry and formula of {FeO_6}, where Fe-O distances are approximately 2.0 Å and the *cis*/*trans* angles range from 85.5° to 103°.

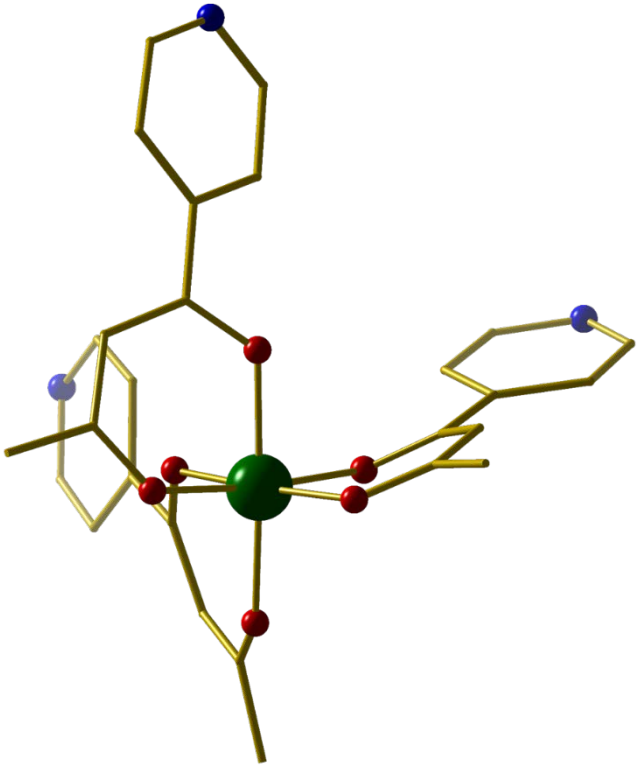

Figure 3.2. Molecular structure of [$Fe^{III}L_3$]. Fe = green, C = gold, N= blue, O = red. H-atoms omitted for clarity.

Structures **1**-**5** possess similar structural features to each other, as do **6** and **7**. For simplicity, both structural types will be discussed separately. The novel heterometallic cages **1**-**5** (see Figure 3.1) form through the general reaction of the relevant metal (II) salt with $[Fe^{III}L_3]$ in a mixed solvent system of DCM and MeOH/ EtOH. In each case, the metallic skeleton forms a $[Fe^{III}{}_8M^{II}{}_6]^{12+}$ cube, where the Fe^{III} ions of $[Fe^{III}L_3]$ occupy the corners and the M^{II} are located at the centre of the square faces and coordinate to the N atoms (M^{II}-N, 1.98-2.1 Å) to form bridges between the corners and faces. Each face of the cube is defined by four Fe^{III} ions and one M^{II} ion which sits at the centre of the face. All anions present in the cages originate from the M^{II} salts used in the syntheses. The overall positive charges of complexes **1**, **2** and **5** are balanced by counter-ions on the outside of the cages (complex **2** also possesses $6Br^-$ ions coordinated and pointing inside the cavity). NO_3^- ions in cube **3** and SCN^- and Cl^- ions in cube **4**, all coordinated on the apical positions, charge balance the structures to give overall neutral cages. The presence of H_2O molecules in complex **5** arise from either hydrated metal salt or non-dried solvents used. In **1**, the Pd^{II} ions are four coordinate and square planar as expected (Pd-N, ~2 Å). Whilst in 2 the Cu^{II} ions are square-based pyramidal $\{CuN_4Br\}$ with the Br- ions situated within the cavity of the cage (Cu-Br, 2.53-2.64 Å). For four of these Cu^{II} ions there is also a close contact to a Br^- counter ion outside the cage (Cu···Br, 3.03 Å). The Cu-Br and Br···Cu-Br moieties represent the elongated JT axis (d_z^2) of the Cu^{II} ion, perpendicular to the equatorial CuN_4 plane ($d_{x^2-y^2}$) in the face of the cube (Cu-N, ~2 Å). The Ni^{II} and Co^{II} centres in **4** and **5** all possess an octahedral geometry with the apical positions being occupied by SCN^- ions pointing inside and outside the cavity. Structure **4** also contains a Cl^- ion disordered between Ni1 and Ni13 (50 % occupancy for each site). The S atom from the SCN^- anion pointing into the cavity on Ni1 is disordered in 3 positions. This can be clearly seen in Figure 3.1. The edges of the square faces are approximately 12.5 Å in length whilst the diagonal lengths between the Fe^{III} ions are approximately 17.7 Å. The cubes have an accessible void space of approximately between 817 $Å^3$ and 1317 $Å^3$ (Figure 3.3).

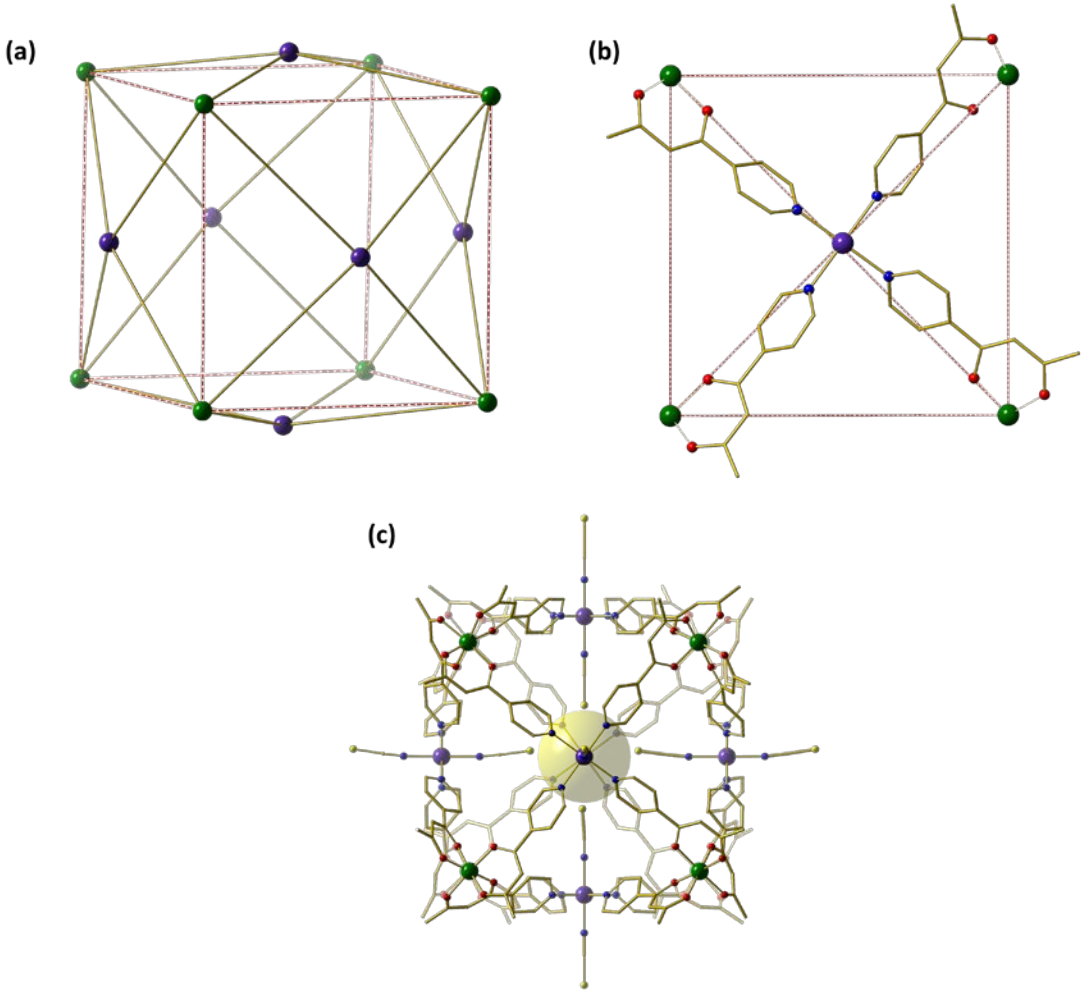

Figure 3.3. Representation of a) the metallic skeleton of **4**, b) one of the six faces of the cube, highlighting the coordination geometry of the Ni^{II} ion on the equatorial positions and c) the accessible internal cavity, represented by a yellow sphere, of **4**, calculated using the Van Der Waal's radii. Fe = green, Ni = purple, C = gold, N = blue, O = red, S = yellow. H-atoms omitted for clarity.

The heterometallic, neutral trigonal bipyramidal cages $[Fe_2Co_3L_6Cl_6]$ (**6**) and $[Fe_2Zn_3L_6Br_6]$ (**7**), were synthesised in a similar manner, by addition of tetrahedral M^{II} salts to the metalloligand $[Fe^{III}L_3]$ in acetone, or in a mixed solvent system of DCM and acetone, with crystals isolated from slow evaporation of the mother liquor (see the experimental section for full details). The metallic skeletons of the cages describe a trigonal bipyramid with the Fe^{III} ions situated on the axial positions and the M^{II} ions on the equatorial sites. The approximate dimensions of the $[M^{III}_2M^{II}_3]^{n+}$ metallic skeleton are $M^{III}\cdots M^{II}$ (8.77-8.99 Å), $M^{II}\cdots M^{II}$ (11.84-12.31 Å) and $M^{III}\cdots M^{III}$

(11.06-11.10 Å). Each of the three M^{II} metal ions is coordinated by two N donors from the pyridyl groups of $[Fe^{III}L_3]$. The N-M^{II}-N angle of the tetrahedral CoN_2Cl_2/ZnN_2Br_2 moiety for the compounds lies in the range 90.63-103.57°. The Co^{II} and Zn^{II} ions lie in distorted tetrahedral environments with bond distances in the range 2.05-2.35 Å (Co-Cl ~2.23 Å, Co-N ~2.05 Å, Zn-Br ~2.35 Å and Zn-N ~2.06 Å) and bond angles around the metal centres ranging from 90.62° to 120.08°.

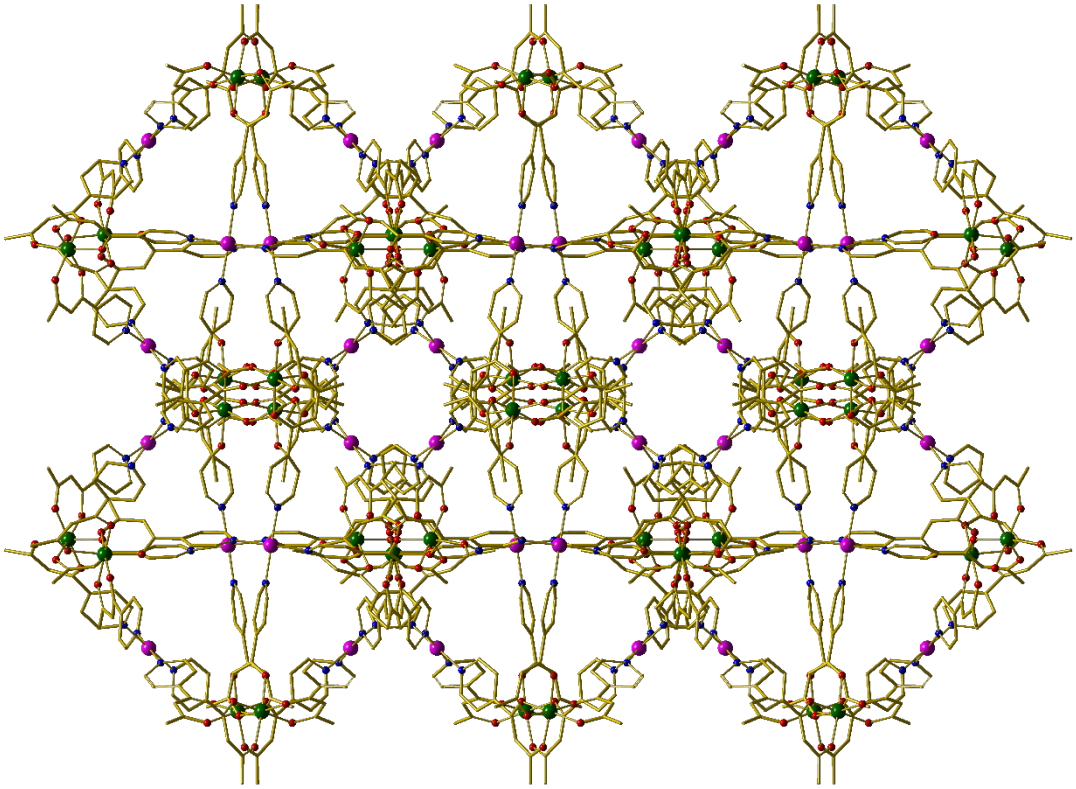

Figure 3.4. The packing of molecules of **1** in the crystal, as viewed along the *b*-axis. Fe = green, Pd = pink, C = gold, N = blue, O = red, S = yellow. Counter-ions and H-atoms have been removed for clarity.

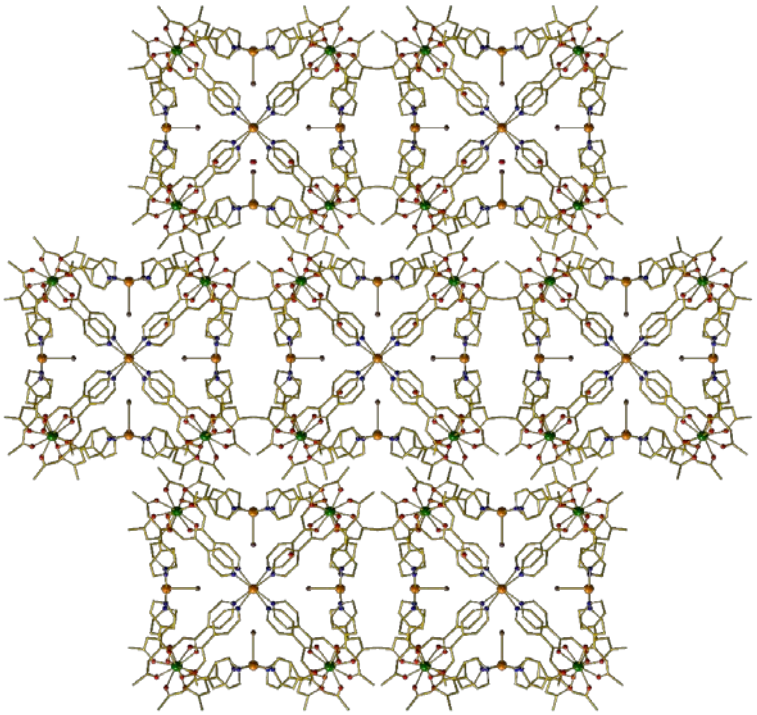

Figure 3.5. The packing of molecules of **2** in the crystal, as viewed along the *b*-axis. Fe = green, Cu = orange, C = gold, N = blue, O = red, Br = brown. Counter-ions and H-atoms omitted for clarity.

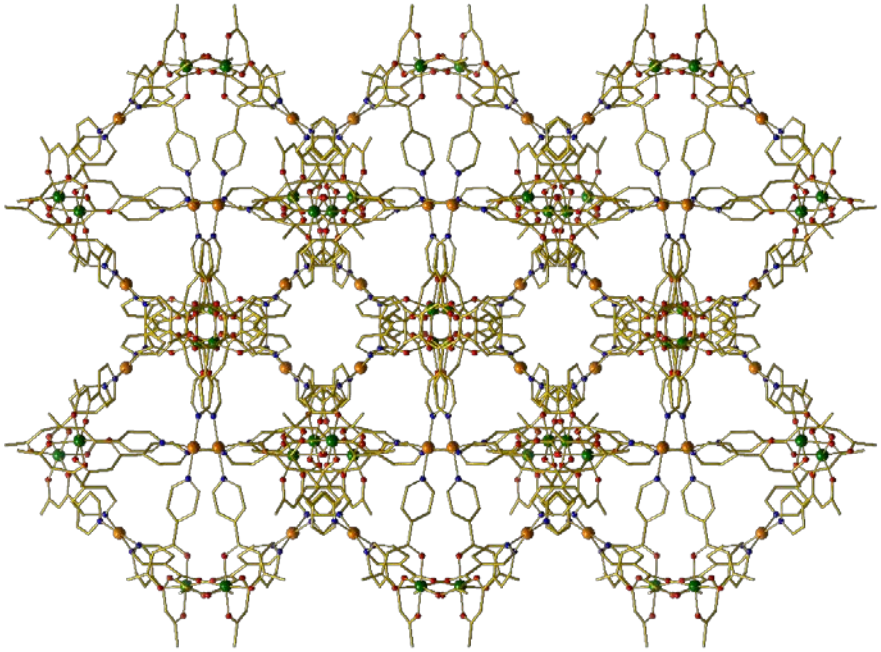

Figure 3.6. The packing of molecules of **3** in the crystal, as viewed along the *c*-axis. Fe = green, Cu = orange, C = gold N = blue, O = red. Counter-ions and H-atoms omitted for clarity.

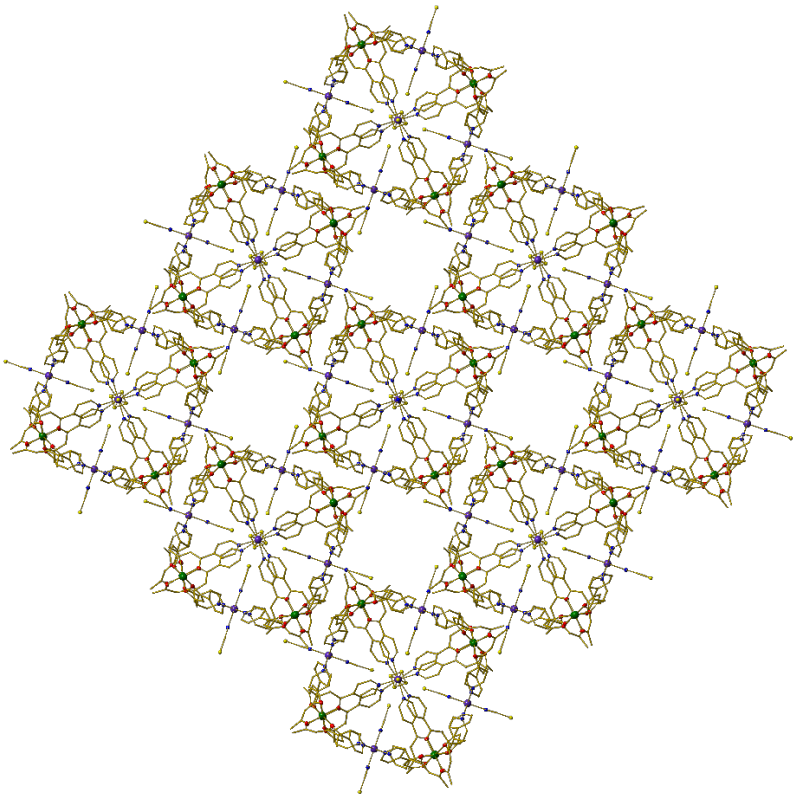

Figure 3.7. The packing of molecules in **4** in the crystal, as viewed along the *c*-axis. Fe = green, Ni = purple, C = gold, N = blue, O = red, S = yellow, Cl = green. H-atoms omitted for clarity.

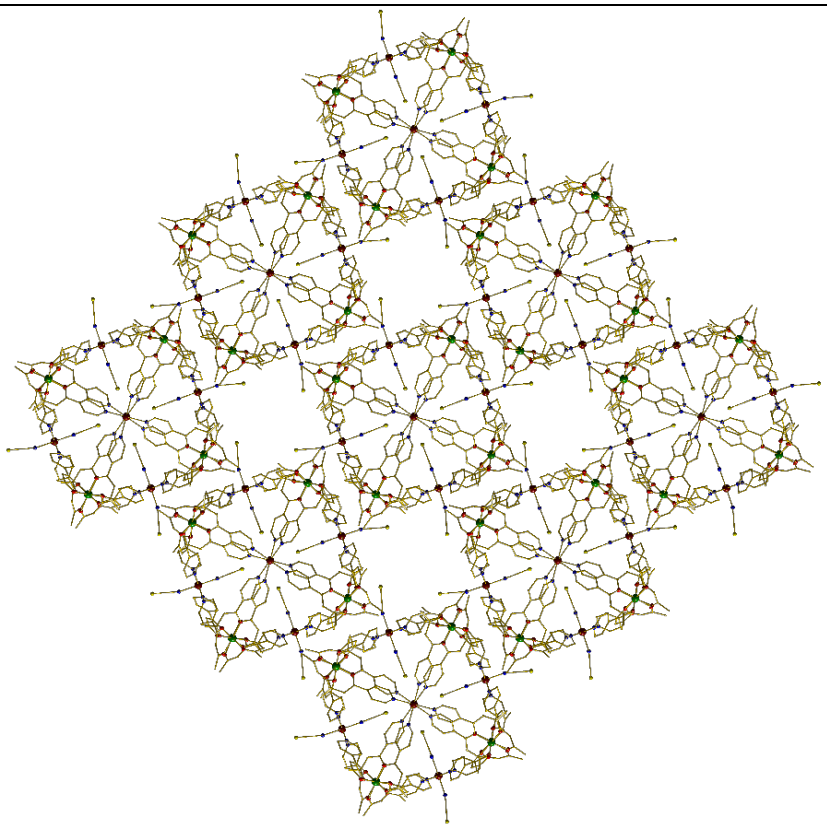

Figure 3.8. The packing of molecules of **5** in the crystal, as viewed along the *c*-axis. Fe = green, Co = red, C = gold, N = blue, O = red, S = yellow. Counter-ions and H-atoms omitted for clarity.

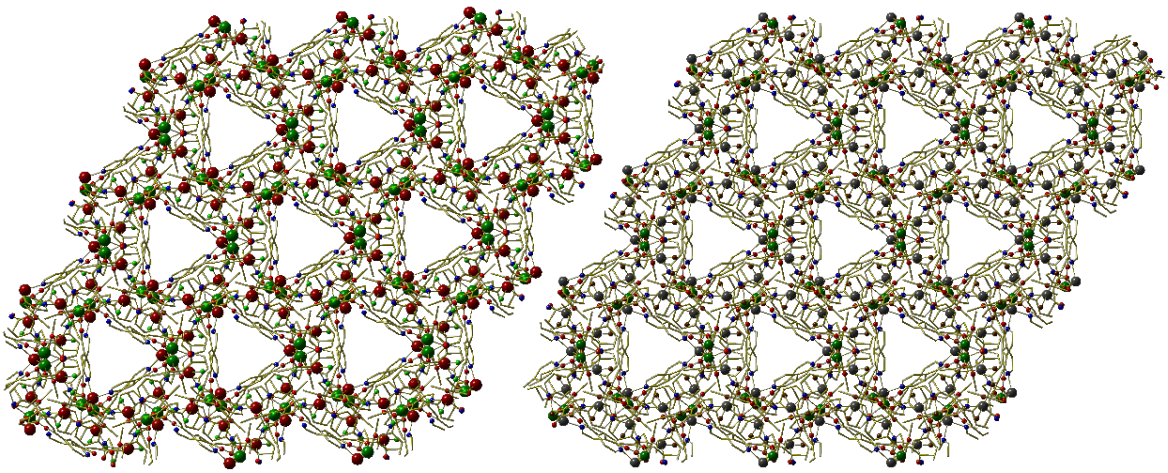

Figure 3.9. The packing of molecules of **6** (left) and **7** (right), as viewed along the *c*-axis. Fe = green, Co = dark red, Zn = grey, C = gold, N = blue, O = bright red, Br = brown, Cl = green. H-atoms omitted for clarity.

SQUID Magnetometry

The DC (direct current) molar magnetic susceptibility, χ_M, of polycrystalline samples of **2** and **4**-**6** were measured under an applied magnetic field, B, of 0.1 T, in a temperature (*T*) range of 2-300 K. The experimental results are shown below in Figures 3.10 and 3.11 in the form of the $\chi_M T$ product *vs T*, where χ = M/B and M is the magnetisation of the sample. As **2**, **4** and **5** are a different structural type to **6** and **7**, the susceptibility and magnetisation data have been plotted and characterised separately.

At 300 K, the $\chi_M T$ values of **2** and **4** are in excellent agreement with the calculated Curie constants for $[Fe^{III}_8Cu^{II}_6]$ and $[Fe^{III}_8Ni^{II}_6]$ units at 37.25 cm^3 K mol^{-1} and 41 cm^3 K mol^{-1}, respectively (Figure 3.10). Complex **5**, however does not follow Curie behaviour, as at the highest temperature the $\chi_M T$ value is 58.86 cm^3 K mol^{-1}, which is much higher than the expected value of 46.25 cm^3 K mol^{-1}. This is due to the first order orbital contribution in octahedral Co^{II}. Upon cooling the $\chi_M T$ products decrease with decreasing temperature, reaching final values of 26.78 cm^3 K mol^{-1}, 30.24 cm^3 K mol^{-1} and 38.86 cm^3 K mol^{-1} for **2**, **4** and **5** respectively. The shapes of the curves are indicative of very weak anti-ferromagnetic behaviour, quantitative analysis is prohibited due to the large Hilbert space associated with a molecular containing eight Fe^{III} and six M^{II} ions, which is beyond current computing ability. Variable-temperature-variable-field (VTVB) magnetisation data *vs* $\mu_B B / kT$, shown in Figure 3.10, are consistent with the expected magnetic saturation for all three structures. This is consistent with the very weak antiferromagnetic exchange interactions between the metal centres being overcome with the applied magnetic field.

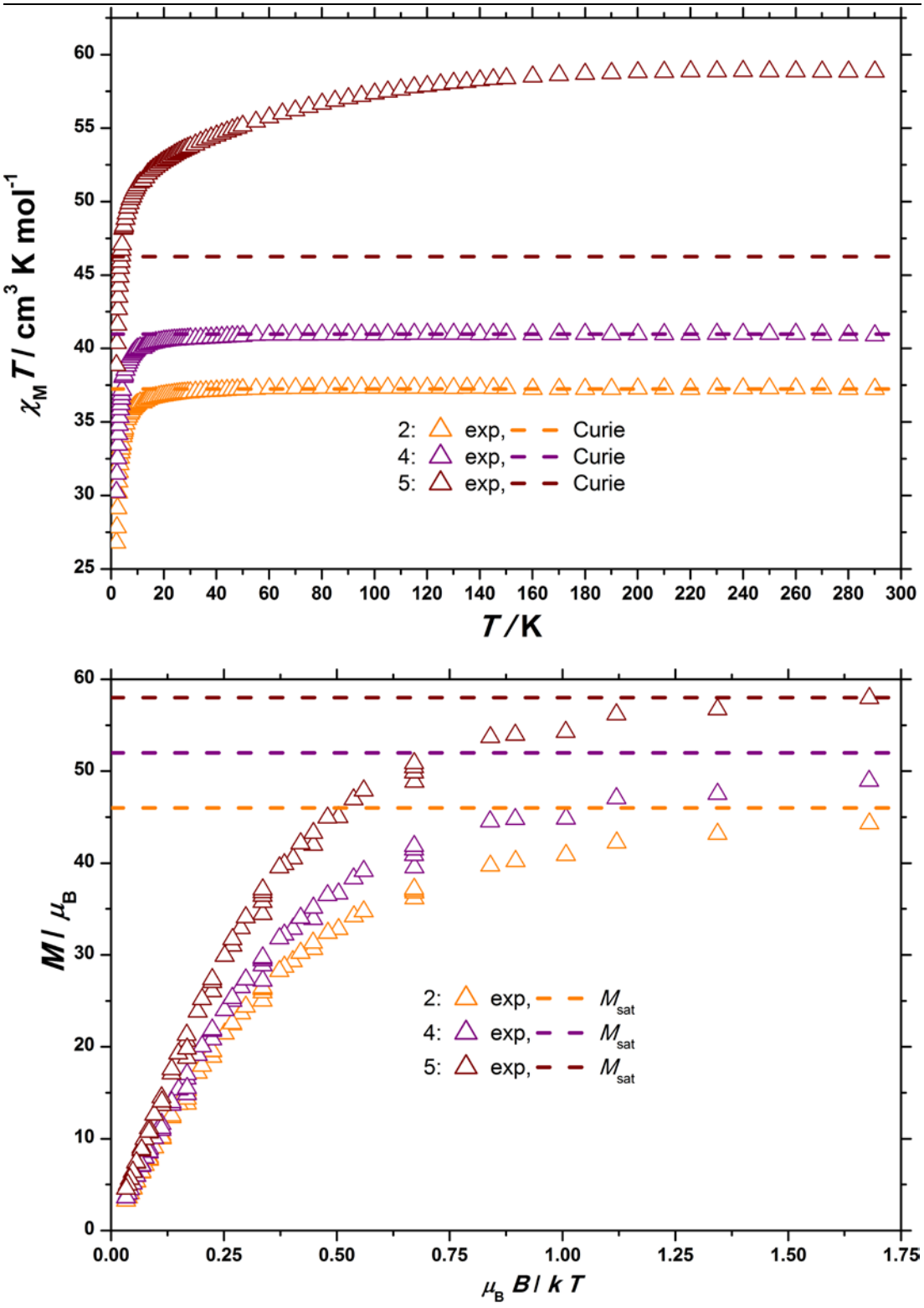

Figure 3.10. Top: Temperature dependence of the $\chi_M T$ product of a polycrystalline sample of **2, 4** and **5** with B = 0.1 T. Bottom: Variable-temperature-and-variable-field (VTVB) magnetisation data.

At room temperature, the $\chi_M T$ product of **6** (Figure 3.11) has the value of 14.4 cm^3 K mol^{-1} which is in good agreement with the sum of Curie constants for a $[Fe^{III}_2Co^{II}_3]$ unit (14.375 cm^3 K mol^{-1}, $g_{Fe} = g_{Co} = 2.0$). Upon cooling, the $\chi_M T$ product of **6** remains essentially constant down to approximately 100 K, wherefrom it decreases upon further cooling to 9.5 cm^3 K mol^{-1} at 2 K. Given that the anisotropy of Fe^{III} is negligible, this behaviour is consistent with a relatively large single-ion magnetic anisotropy for the Co^{II} centres and/or an antiferromagnetic exchange interaction between the Fe^{III} and Co^{II} centres. To better define the low-temperature magnetic properties of **6**, low temperature VTVB magnetisation data were measured in the temperature and magnetic field ranges T = 2 - 12 K and B = 0 - 5 T. The VTVB magnetisation data of **6** are shown in the lower panel of Figure 3.11. At the highest investigated field (5 T) and the lowest investigated temperature (2 K), the magnetisation of **6** is of 13.7 μ_B (μ_B is the Bohr magneton), thus, an intermediate spin state is stabilised under these conditions. Furthermore, when the VTVB data of **6** are plotted against the reduced quantity $\mu_B B / kT$ little nesting of the VTVB data is observed. This observation indicates that the part of the energy spectrum (discussed later and shown in Figure 3.12) of **6** probed under these experimental conditions does not present significant anisotropy splitting with respect to the temperature of measurement at zero magnetic field.

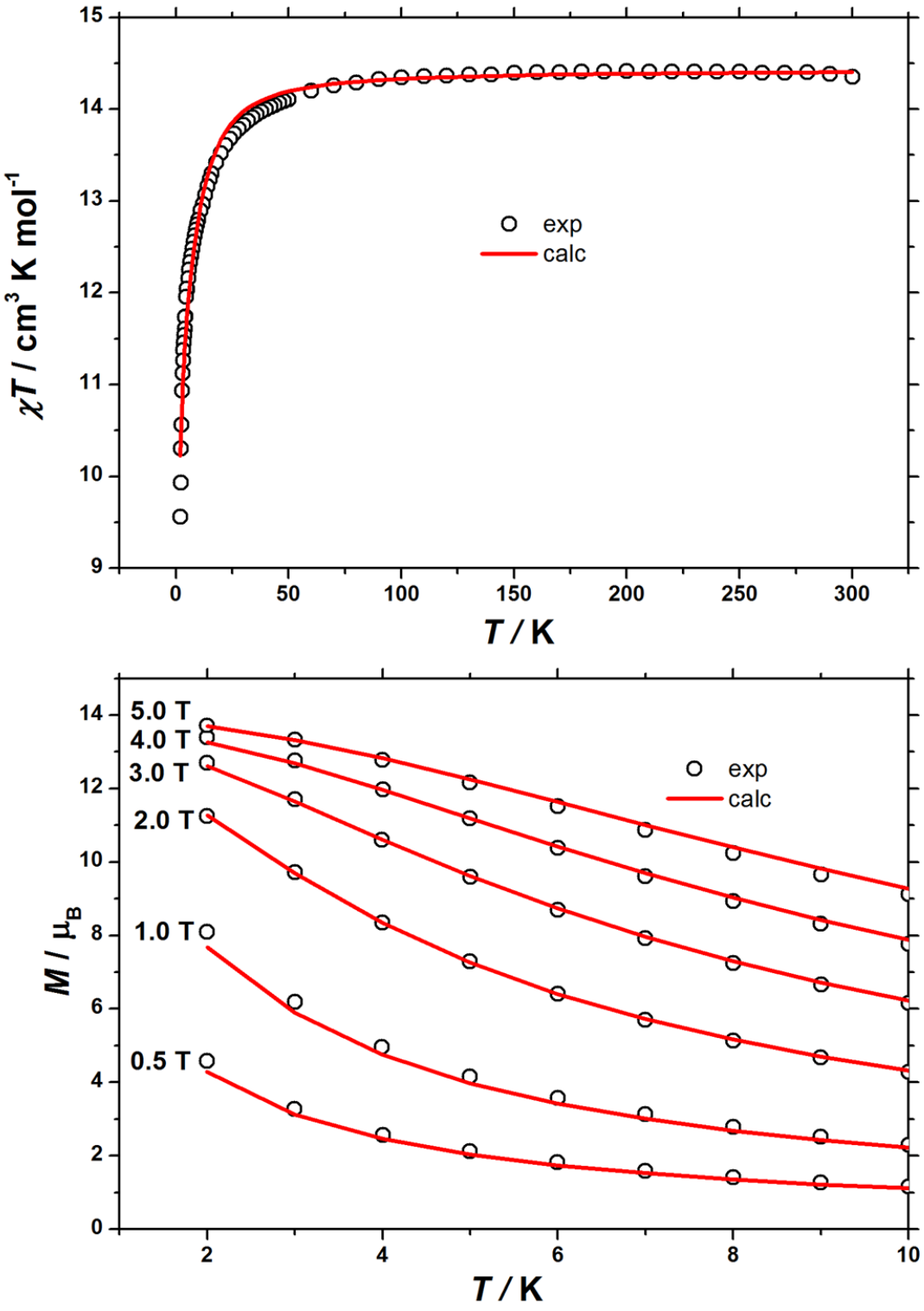

Figure 3.11. Top: Temperature dependence of the $\chi_M T$ product of a polycrystalline sample of **6** with B = 0.1 T. Bottom: VTVB magnetisation data of **6** in the field and temperature ranges 0.5 to 5 T and 2 to 10 K, respectively.

For the quantitative interpretation of the magnetisation data, we used spin-Hamiltonian (1)

$$\hat{H} = \mu_B B \sum_i g_i \hat{S}_i - 2 \sum_{i,j<i} J_{ij} \hat{S}_i \cdot \hat{S}_j + \sum_i D_i \left[\hat{S}_{i,z}^2 - S_i (S_i + 1)/3 \right] \qquad (1)$$

where the summation indexes *i*, *j* run through the constitutive metal centres, g_i is the *g*-factor of the ith centre, $\hat{S}$ is a spin operator, *J* is the isotropic exchange interaction parameter, *D* is the uniaxial anisotropy parameter and *S* is the total spin. In our spin-Hamiltonian model we assume for simplicity that all *g*-factors are equal to 2, we only consider exchange interactions between Co^{II} and Fe^{III} centres, and neglect the single-ion anisotropy of Fe^{III}. Thus our model contains only two free parameters, namely, $J_{Fe\text{-}Co}$ and D_{Co}. The $\chi_M T$ product of **6** was independently fitted to the isotropic part of spin-Hamiltonian (1) by numerical diagonalization and by use of the Levenberg-Marquardt algorithm.[38] This resulted in the best-fit parameter $J_{Fe\text{-}Co}$ = -0.043 cm^{-1}. Thereafter, $J_{Fe\text{-}Co}$ was fixed to the determined best-fit value and the VTVB data of **6** were independently fitted to the full spin-Hamiltonian (1). This fit resulted in the best-fit parameter D_{Co} = -11.3 cm^{-1}. The best-fit curves are shown as solid red lines in Figure 3.11. With these parameters, the energy spectrum of **6** consists of four groups of densely packed states, each separated by approximately $2D_{Co}$ (Figure 3.12). It is interesting to note that multiple ground level crossings occur simultaneously at approximately 0.47 T when the magnetic field is applied parallel to the quantisation axis.

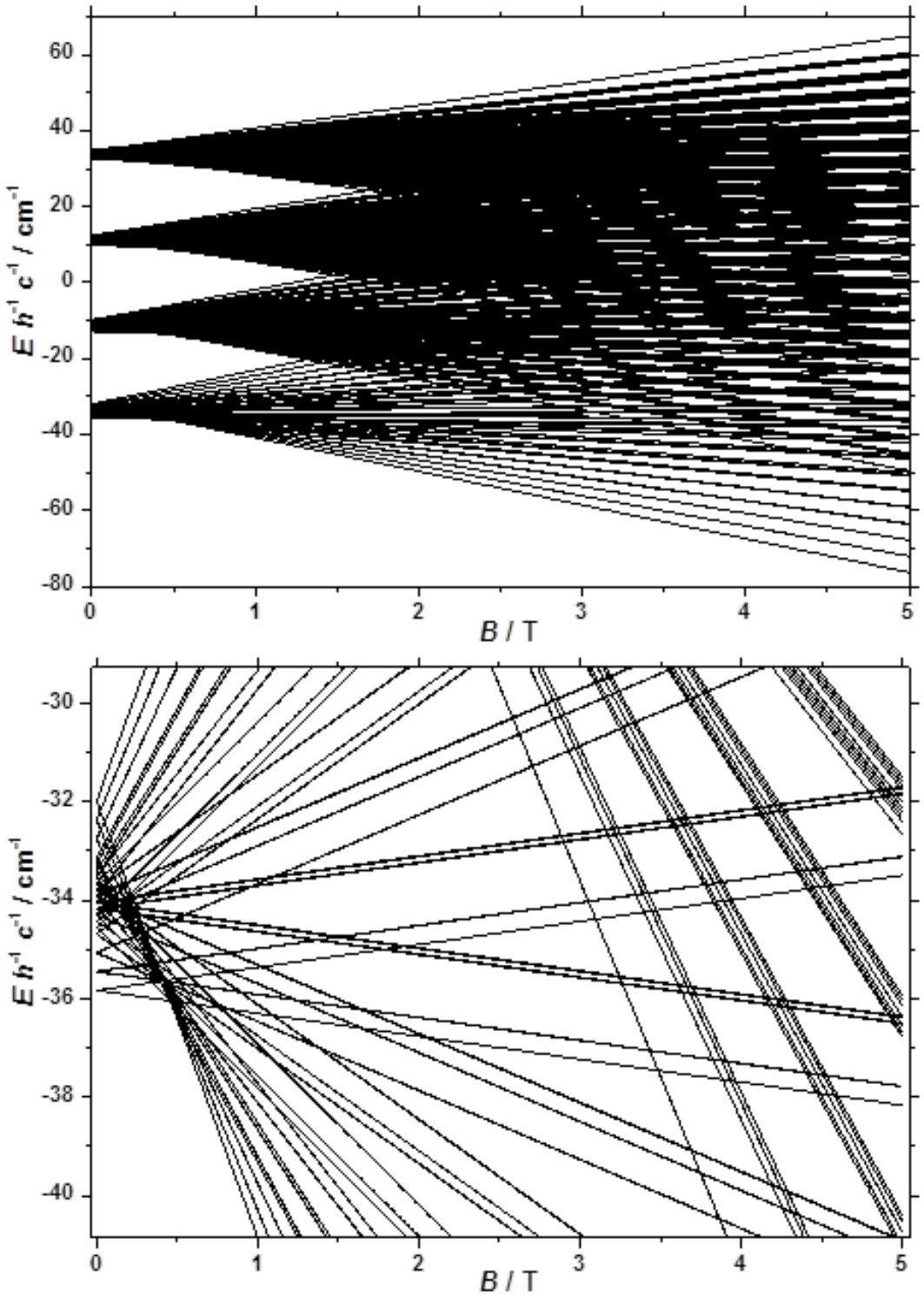

Figure 3.12. Top: Energy spectrum of **6** determined with the best-fit parameters (see text) and the magnetic field applied along the quantisation axis. Bottom: low-lying states of the energy spectrum of **6**, determined as above.

EPR Spectroscopy

X- and Q-band EPR spectra (Figure 3.13) of $[Fe^{III}L_3]$ reveal a rather small ZFS of D = 0.08 cm^{-1} with $|E/D|$ = 1/3 (note the sign of D has no significance with a fully rhombic ***D***-tensor). These values are similar to those reported for $[Fe(acac)_3]$ ($|D|$ = 0.16 cm^{-1}, E/D = 0.3)[39] and $[Fe(dpm)_3]$ (dpm = dipivaloylmethane; D = -0.20 cm^{-1}, $|E/D|$ = 0.25).[40] On incorporation into the $\{Fe^{III}{}_2Zn^{II}{}_3\}$ complex **7**, a much richer spectrum is observed (Figure 3.13), giving D = 0.20 cm^{-1} (E/D = 1/3).

The $\{Fe^{III}{}_2Co^{II}{}_3\}$ complex **6** gives Q-band EPR spectra with very broad features at approximately 5, 9 and 12 kG that line up with the main features of the spectrum of the $\{Fe^{III}{}_2Zn^{II}{}_3\}$ complex **7**. Hence, the ZFS at Fe^{III} must be similar. The very large ZFS at Co^{II} means that only transitions within the ground Kramers doublet of this ion are observed (the microwave energy, hv << $|D|$), and there must be a significant rhombicity in order for these transitions to fall within the observed features. The spectra also show that the $J_{Fe\text{-}Co}$ exchange interaction must be very weak, resulting only in severe broadening of the peaks. Test calculations on a simple $\{Fe^{III}Co^{II}\}$ model, with fixed ZFS at the s = 5/2 and 3/2 spins (the latter taking D = -14 cm^{-1} with E/D = 0.1; averaging the results of CASSCF calculations) suggest that if $|J_{Fe\text{-}Co}|$ > *ca*. 0.02 cm^{-1} then additional features would be observed in the Q-band EPR spectrum. Note that the limit for the full, five-spin system would be different.

The D_{Fe} values obtained from EPR would have a negligible effect on the calculated $\chi_M T$ *vs* T curves for **6**, and a negligible effect on the global level structure in Figure 3.12, because both $|D_{Fe}|$ and $|J_{FeCo}|$ are << $|D_{Co}|$. However, it would affect the detail of the states within each of the densely packed mulitplets of Figure 3.12, because $|D_{Fe}|$ and $|J_{FeCo}|$ are of similar magnitude.

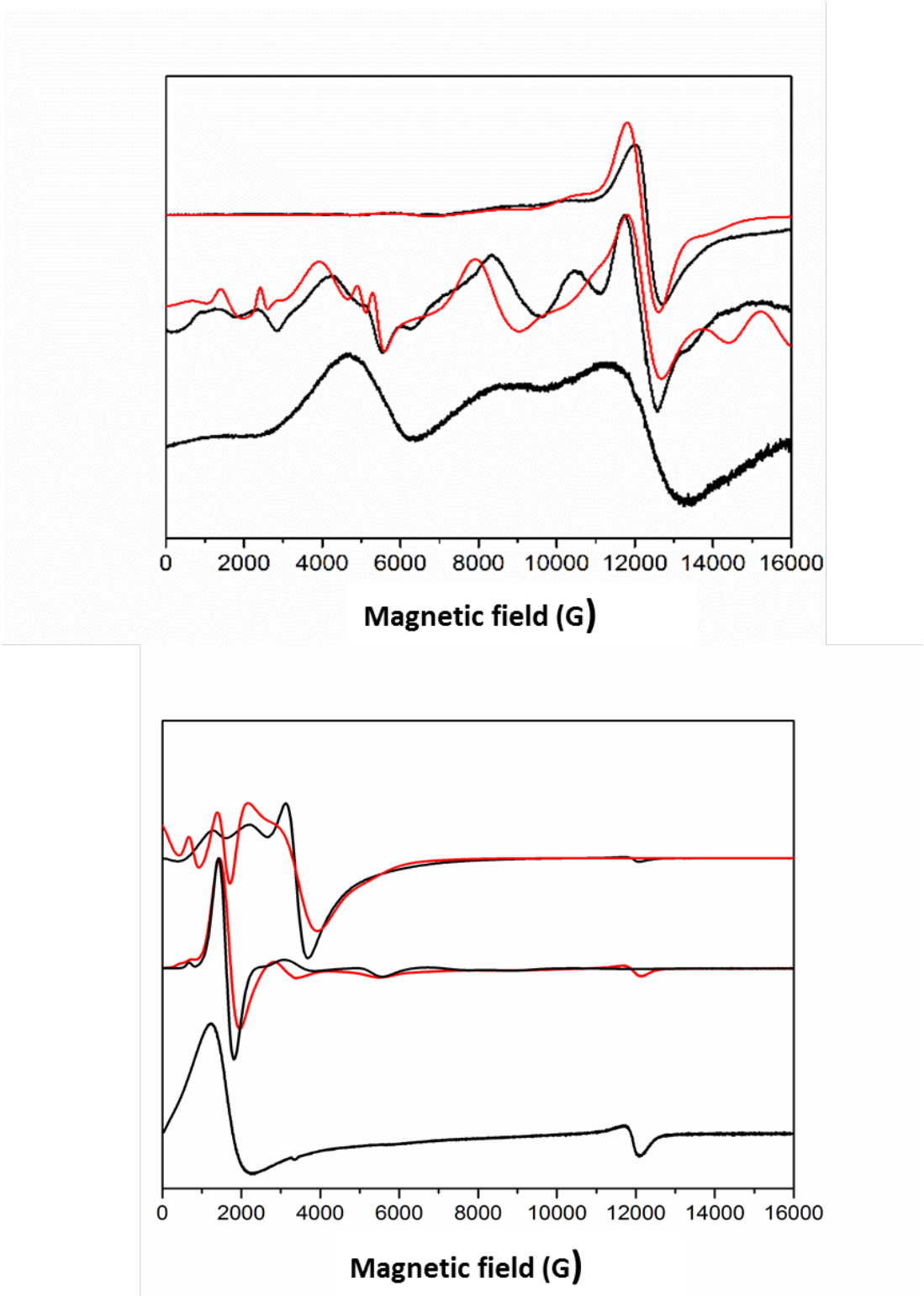

Figure 3.13. Q-band (top) and X-band (bottom) EPR spectra of powdered samples of (from top to bottom) [FeL_3], **7** and **6** at 5 K (black), and calculated spectra (red). D = 0.08 cm^{-1} ($|E/D|$ = 1/3) for [FeL_3], and D = 0.20 cm^{-1} ($|E/D|$ = 1/3) for **7** (with 400 G Gaussian linewidths and 10-20% D-strain).

3.4 Conclusion

The reaction of the metalloligand $[FeL^{III}_3]$ (where HL = 1-(4-pyridyl)butane-1,3-dione) with various M^{II} ions produces two new families of compounds, according to the ratio and geometry of the M^{II} used. 5 novel $[Fe^{III}_8M^{II}_6]$ cubes have been synthesised, using Cu, Co, Ni and Pd salts. The structures all consist of $[FeL^{III}_3]$ situated at the vertices of the cube, whilst the M^{II} centres bridge between. The structural stability of these has been emphasised by the ability to switch the M^{II} centre however maintaining the coordination motifs throughout the structures. This also demonstrates the possibility to also tune the magnetic properties, using further work. The large cavities within these structures open them up to potential applications, such as host-guest chemistry.

The second family of structures consists of heterometallic-Fe^{III} trigonal bipyramidal cages. The metallic skeleton of all cages describes a trigonal bipyramid with the M^{III} ions occupying the two axial sites and the M^{II} ions sitting in the three equitorial sites. Direct current (DC) magnetic susceptibility and magnetisation measurements on **6** reveal weak antiferromagnetic exchange between the Fe^{III} and Co^{II} ions, with $|D_{Co}| = 11.3\ cm^{-1}$. EPR measurements on $[FeL^{III}_3]$, **6** and **7** reveal that the distortion imposed on the $\{MO_6\}$ coordination sphere of $[M^{III}L_3]$ by complexation in the $\{M^{III}_2M^{II}_3\}$ supramolecules results in a small, but measurable, increase of the zero field splitting (ZFS) at M^{III}.

3.5 References

1. D. M. Kurtz, *Chem. Rev.*, 1990, **90**, 585.
2. G. Bunker, L. Petersson, B.-M. Sjöberg, M. Sahlin, M. Chance and A. Ehrenberg, *Biochemistry,* 1987, **26**, 4708.
3. B. A. Averill, J. C. Davis, S. Burman, T. Zirino, J. Sanders-Loehr, T. M. Loehr, J. T. Sage and P. G. Debrunner, *J. Am. Chem. Soc*., 1987, **109**, 3760.
4. K. L. Taft, G. C. Papaefthymiou and S. J. Lippard, *Science*, 1993, **259**, 1302.
5. L. F. Jones, E. K. Brechin, D. Collison, M. Helliwell, T. Mallah, S. Piligkos, G. Rajaraman and W. Wernsdorfer, *Inorg. Chem.*, 2003, **42**, 6601.
6. O. Kahn, *Chem. Phys. Lett*., 1997, **265**, 109.
7. G. Christou, D. Gatteschi, D. N. Hendrickson and R. Sessoli, *MRS Bull.*, 2000, **25**, 66.
8. S. M.Gorun and S. J. Lippard, *Inorg. Chem*., 1991, **30**, 1625.
9. H. Weihe and H. U. Güdel, *J. Am. Chem. Soc.*, 1997, **119**, 6539.
10. K. L. Taft, C. D. Selfs, G. C. Papaefthymiou, S. Foner, D. Gatteschi and S. L. Lippard, *J. Am. Chem. Soc.*, 1994, **116**, 824.
11. A.-L. Barra, P. Debrunner, D. Gatteschi, C. E. Schulz and R. Sessoli, *Europhys. Lett*., 1996, **35**, 133.
12. D. Gatteschi, A. Caneschi and R. Sessoli, *Chem. Soc. Rev*., 1996, 101.
13. S. Accorsi, A.-L. Barra, A. Caneschi, G. Chastanet, A. Cornea, A. C. Fabretti, D. Gatteschi, C. Mortalò, E. Olivieri, F. Parenti, P. Rosa, R. Sessoli, L. Sorace, W. Wensdorfer and L. Zobbi, *J. Am. Chem. Soc.*, 2006, **128**, 4742.
14. A. K. Powell, S. L. Heath, D. Gatteschi, K. Pardi, R. Sessoli, G. Spina, F. Del Giallo and F. Pieralli, *J. Am. Chem. Soc*., 1005, **117**, 2491.
15. I. A. Gass, C. J. Milios, M. Evangelisti, S. L. Heath, D. Collison, S. Parsons and E. K. Brechin, *Polyhedron*, 2007, **26**, 1835.
16. G. W. Powell, H. N. Lancashire, E. K. Brechin, D. Collison, S. L. Heath, T. Mallah and W. Wernsdorfer, *Angew. Chem., Int. Ed.*, 2004, **43**, 5772.
17. I. A. Gass, E. K. Brechin and M. Evangelisti, *Polyhedron*, 2013, **52**, 1177.
18. R. Shaw, R. H. Laye, L. F. Jones, D. M. Low, C. Talbot-Eechelaers, Q. Wei, C. J. Milios, S. Teat, M. Helliwell, J. Raftery, M. Evangelisti, M. Affronte, D. Collison, E. K. Brechin and E. J. L. McInnes, *Inorg. Chem*., 2007, **46**, 4968.
19. C. Schröder, X. Fang, Y. Furukawa, M. Luban, R. Prozorov, F. Borsa and K. Kumagai, *J. Phys.: Condens. Matter,* 2010, **22**, 216007.
20. L. P. Engelhardt C. A. Muryn, R. G. Pritchard, G. A. Timco, F. Tuna and R. E. P. Winpenny, *Angew. Chem., Int. Ed.*, 2008, **47**, 924.

21. G. F. S. Whitehead, F. Moro, G. A. Timco, W. Wernsdorfer, S. J. Teat and R. E. P. Winpenny, *Angew. Chem., Int. Ed.*, 2013, **52**, 9932.
22. S. Wang, J.-L. Zuo, H.-C. Zhou, H. J. Choi, Y. Ke, J. R. Long and Z.-Z. You, *Angew. Chem. Int., Ed.*, 2004, **43**, 5940.
23. G. Aromí and E. K. Brechin, *Struct. Bond*., 2006, **122**, 1.
24. R. Lescouëzec, F. Lloret, M. Julve, J. Vaissermann and M. Verdaguer, *Inorg. Chem.,* 2002, **41**, 818.
25. G. Christou, *Polyhedron*, 2005, **24**, 2065.
26. F. Reichel, J. K. Clegg, K. Gloe, K. Gloe, J. J. Weigand, J. K. Reynolds. C.-G. Li, J. R. Aldrich-Wright, C. J. Kepert, L. F. Lindoy, H.-C. Yao and F. Li, *Inorg. Chem*., 2014, **53**, 688.
27. J. Y. Yang, M. P. Shores, J. J. Sokol and J. R. Long, *Inorg. Chem*., 2003, **42**, 1403.
28. M. P. Shores, J. J. Sokol and J. R. Long, *J. Am. Chem. Soc*., 2002, **124**, 2279.
29. P. A. Berseth, K. J. Sokol, M. P. Shores, J. L. Heinrich and J. R. Long, *J. Am. Chem. Soc*., 2000, **122**, 9655.
30. G. Kumar and R. Gupta, *Chem. Soc. Rev*., 2013, **42**, 9403.
31. B. Singh, G. Y. Lesher,K. C. Pluncket, E. D. Pagani, D. C. Bode, R. G. Bentley, M. K. Connell, L. T. Hamel and P. J Silver, *J. Med. Chem.*, 1992, **35**, 4858.
32. S. J. Coles and P. A. Gale, *Chem. Sci*., 2012, **3**, 683.
33. *CrystalClear-SM Expert 3.1 b27* (Rigaku, 2012)
34. CrysAlisPro 1.171.38.41 (RigakuOxfordDiffraction, 2015).
35. L. Palatinus and G. Chapuis, *J. Appl. Crystallogr*, 2007, **40**, 786.
36. G. M. Sheldrick, *Acta Crystallogr*., 2015, **71**, 3.
37. O. V.Dolomanov, A.J. Blake, N. R. Champness and M. Schröder, *J. Appl. Crystallogr*. 2003, **36**, 1283.
38. W. H. Press, S. A. Teukolsky, W. T. Vetterling and B. P. Flannery, Numerical recipes in C: The Art of Scientific Computing, Cambridge University Press, Cambridge, 2nd edn, 1992.
39. D. Collison and A. K. Powell, *Inorg. Chem*., 1990, **29**, 4735-4746.
40. A-L. Barra, A. Caneschi, A. Cornia, F. Fabrizi de Biani, D. Gatteschi, C. Sangregorio, R. Sessolia and L. Sorace, *J. Am. Chem. Soc.* 1999, **121**, 5302-5310.

Chapter 4

Pressure-induced phase transitions, NLC behaviour and pressure controlled Jahn-Teller switching in a one-dimensional Cu-based framework

4.1 Introduction

High-pressure crystallographic experiments over the last 20 years or so have proved to be a unique tool in probing the mechanical properties of the organic solid state,[1] metal-complexes, and 2D/3D coordination compounds.[2] In particular, high-pressure techniques have been used to study a vast array of mechanical and chemical properties, such as monitoring changes in electrical conductivity,[3] amorphisation,[4] post-synthetic modification [5] and chemical reactions such as polymerisation[6] and cycloaddition chemistry,[7] where reaction rates can be increased substantially. Previous high-pressure experiments on porous metal-organic framework (MOF) materials have shown that on loading a diamond anvil cell (DAC) with a single-crystal or polycrystalline powder, the hydrostatic media which surrounds the sample (to ensure hydrostatic conditions) can actually be forced inside the pores on increasing pressure, causing the pore and sample volume to increase on increasing pressure.[8] More recently, this technique has also been used to determine the position of CH_4 and CO_2 molecules inside the pores of a small pore Sc-based MOF at room temperature using a laboratory X-ray diffractometer, and has proved useful in experimentally determining the maximum size of guest molecules which can penetrate into a pore.[9] On direct compression of more dense frameworks, negative linear compressibility (NLC) has also been observed, which results in an expansion of one or more of the unit cell dimensions, but an overall contraction in volume. Such changes in the compressibility behaviour of metal-containing framework materials is usually as a result of common structural motifs which rotate or bend in order to accommodate increases in length along particular crystallographic directions.[10] Changes in coordination environment can also be induced at pressure, as metal-ligand bonds are more susceptible to compression than covalent bonds.[2] In previous high pressure studies on metal complexes or coordination compounds in which the metal ion has an asymmetric octahedral environment caused by JT distortions for example (such as those observed in Cu^{II} and Mn^{III} complexes), the application of pressure can result in compression of the JT axis, and can even be switched to lie along another bonding direction within the octahedron.[11,12] Herein we present a

high-pressure crystallographic study on the novel and unreported Cu-framework bis[1-(4-pyridyl)butane-1,3-dione]copper(II) (hereafter referred to as CuPyr-I). On application of pressure, CuPyr-I is unusual in that it demonstrates several of these interesting phenomena within the same framework, including a single-crystal to single-crystal phase transition, a switching of the JT axis which is dependent on the hydrostatic media, piezochroism and NLC behaviour.

4.2 Experimental

Materials and Physical Measurements

High-Pressure Single-Crystal X-ray Diffraction Experiments

High pressure experiments were performed using a Merrill-Bassett diamond anvil cell (DAC) with a half opening angle of 40° equipped with 600 µm culet Boehler-Almax cut diamonds, tungsten-carbide backing discs and a tungsten gasket.[13,14] A single crystal of the sample with a small chip of ruby (as the pressure calibrate) were loaded into the DAC using either MeOH or Fluorinert (FC-70) as a hydrostatic media. The ruby fluorescence method was used to measure the pressure throughout the experiment.[15]

High-Pressure Laboratory and Synchrotron Data Collection, Reduction and Refinement

Initially an ambient pressure and temperature dataset was collected in order to have a comparison for the high pressure data, which were also collected at room temperature. A single crystal was mounted on to a three-circle Bruker SMART APEXII diffractometer with graphite monochromated MoK_α radiation (λ = 0.71073 Å) on which a hemisphere of data was collected. Integration was performed using SAINT and the absorption correction was carried out using SADABS.[16,17]

High pressure measurements were also collected on a Bruker SMART APEXII diffractometer with graphite monochromated MoK_α radiation (λ = 0.71073 Å) using FC-70 as a hydrostatic medium. Data collection strategies were as described by Dawson *et al*., with a step size of 0.5° and exposure time of 40 s (60 s for the last pressure point).[18] The data were collected from 0.07 to 1.56 GPa. Cell indexing and data processing were carried out using the Bruker APEX II software. Integration was

performed using SAINT using dynamic masks created to remove regions of the detector which were shaded by the pressure cell. The absorption corrections were carried out using SADABS.[16,17,19]

High-pressure single-crystal diffraction experiments using MeOH as a hydrostatic medium were collected at the DIAMOND Light Source on beamline I19-EH1 using synchrotron radiation (λ = 0.48590 Å) on a four-circle Crystal Logic diffractometer equipped with a Rigaku Saturn 724+ CCD detector. Data collection strategies were based on those described by Dawson *et al*., with a step size of 0.5° and exposure time of 1 s.[18]

Cell indexing and data processing were carried out using the Bruker APEX II software.[7] Integrations were performed using SAINT and absorption corrections were carried out using SADABS.[16,17] The data were integrated using dynamic masks to not only remove regions of the detector which were shaded by the pressure cell, but also to mask intense powder rings from the tungsten gasket. Data were collected in MeOH from 0.80 to 5.40 GPa. On increasing pressure from 2.78 GPa to 3.34 GPa, a single-crystal to single-crystal phase transition took place. The new phase, hereafter referred to as CuPyr-II, results in a doubling of the *a* and *b*-axes, though the symmetry (space group *R*-3) is maintained.

All structures from high pressure data were solved by direct methods using ShelXT.[20] All 1,2 and 1,3 distances for the ligand were restrained to the values obtained from the ambient-pressure structure determination. All metal-ligand distances and angles were allowed to refine freely, as were all torsion angles. Merging and refinement of the data were performed using CRYSTALS.[21] The pores contain disordered solvent of crystallisation. This could not be modelled due to the data being collected at room temperature therefore the SQUEEZE routine in PLATON was used to model the disordered solvent, which equated the solvent to 6 Et_2O molecules per unit cell (the squeeze output as a function of pressure has been tabulated in Table 4.5).

Synthesis

Bis[1-(4-pyridyl)butane-1,3-dione]copper(II) [$Cu(C_9H_8NO_2)_2$] (hereafter referred to as CuPry-I), was synthesised from $CuSO_4$ (0.2 mmol) dissolved in DCM (10 mL) and added to a solution of [$Gd^{III}L_3$] (0.2 mmol, where HL = 1-(4-pyridyl)butane-1,3-dione) in MeOH (10 mL). Although no Gd is in the crystal structure, this precursor is essential for the synthesis. The reaction mixture was stirred for 1 hr before being filtered and diffused from diethyl ether. Green rod-like crystals formed after 4 days suitable for single crystal X-ray diffraction.

4.3 Results and Discussion

Under ambient temperature and pressure CuPyr-I crystallises in the rhombohedral space group *R*-3 (*a/b* = 26.5936(31) Å, *c* = 7.7475(9) Å). Each Cu-centre is coordinated to four 1-(4-pyridyl)butane-1,3-dione linkers, two of these ligands are bound through the dione O-atoms, with the final two binding through the N-atom of the pyridine ring to form a 3D polymer (Figure 4.1). The crystal structure of CuPyr-I is composed of an interpenetration of these 3D polymers to form one-dimensional porous channels (≈ 2 Å in diameter) that run along the *c*-axis direction, shown below in Figure 4.1.

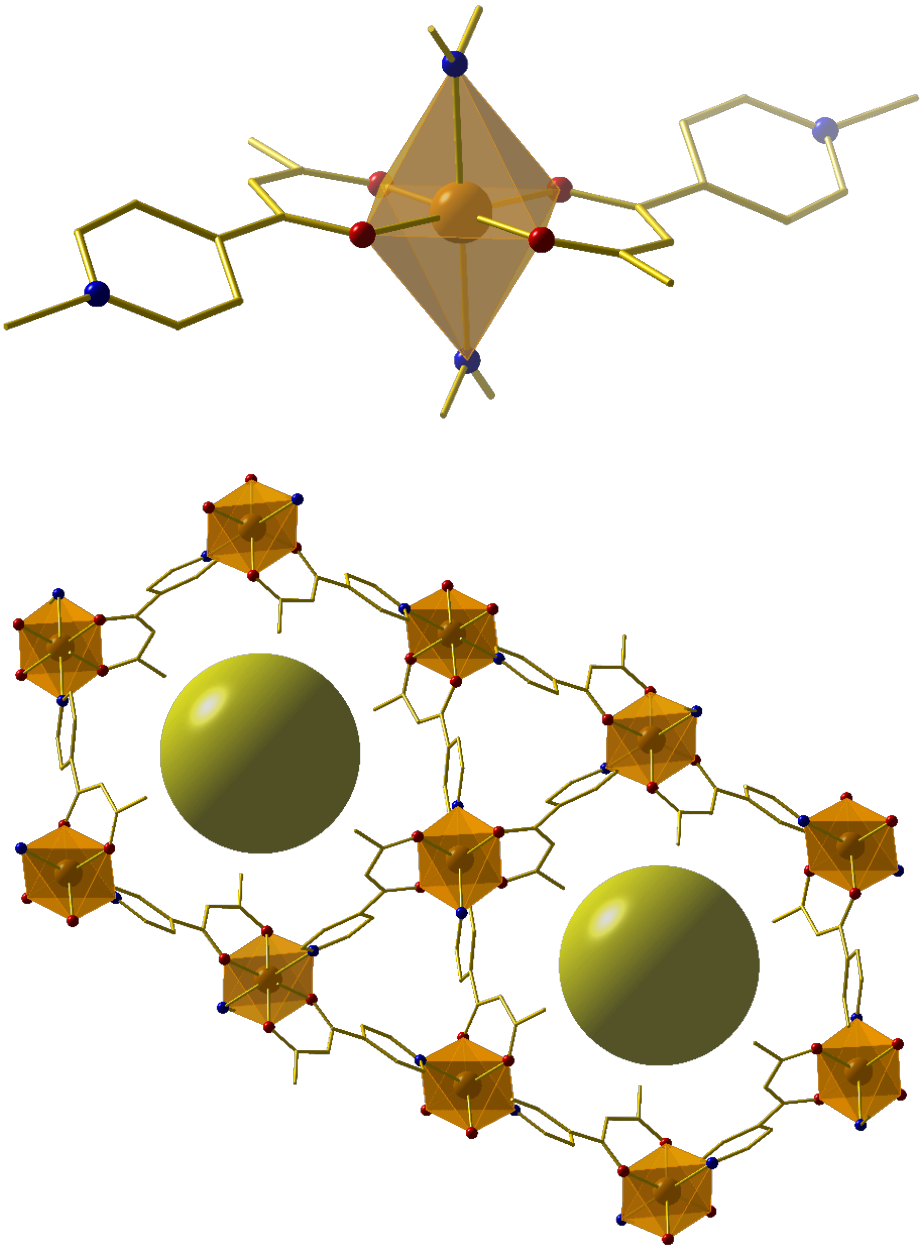

Figure 4.1. Top: Coordination around Cu^{II} centres in CuPyr-I, Bottom: porous channels running along the *c*-axis. Cu = orange, C = gold, N = blue and O = red. H-atoms omitted for clarity. The octahedra demonstrate the geometry around each Cu^{II} centre.

On increasing pressure using FC-70 (a mixture of large perfluorinated hydrocarbons) as a hydrostatic medium, direct compression of the framework occurs, though compression is anisotropic, with the *a/b* and *c*-axes compressing by 4.46 % and 1.29 % to 1.56 GPa respectively, while the volume reduces steadily by 9.89 % to 1.56 GPa (see Table 4.1). On increasing pressure further to 1.84 GPa, the framework

becomes amorphous, though this is unsurprising as the hydrostatic limit for FC-70 is ≈ 2 GPa, and anisotropic compression of frameworks usually results in amorphisation.[22,23]

Table 4.1. Unit cell dimensions with respect to pressure in both MeOH and FC-70.

Pressure (GPa)	a (Å)	b (Å)	c (Å)
MeOH			
0	26.594(3)	26.594(3)	7.7475(9)
0.52	26.447(2)	26.447(2)	7.7509(6)
0.96	26.012(2)	26.012(2)	7.7439(7)
1.57	25.445(2)	25.445(2)	7.7311(5)
2.15	25.173(2)	25.173(2)	7.7336(5)
2.78	24.891(2)	24.891(2)	7.7570(5)
3.34	49.1579(3)	49.1579(3)	7.7889(5)
3.77	48.849(3)	48.849(3)	7.8059(5)
4.20	48.546(3)	48.546(3)	7.8242(5)
4.55	48.280(4)	48.280(4)	7.8324(6)
4.90	48.055(4)	48.055(4)	7.8469(6)
5.28	46.95(1)	46.95(1)	7.714(2)
FC-70			
0	26.5934(3)	26.5934(3)	7.7475(9)
0.07	26.4400(6)	26.4400(6)	7.8045(2)
0.14	26.3304(7)	26.3304(7)	7.7955(2)
0.33	26.0239(7)	26.0239(7)	7.7617(2)
0.88	25.469(2)	25.469(2)	7.7069(6)
1.27	25.356(1)	25.356(1)	7.7006(6)
1.56	25.262(2)	25.262(2)	7.7036(6)

On increasing pressure to 1.56 GPa, the three symmetry independent Cu-O/N bond lengths to the ligand were monitored (Table 4.2). Under ambient pressure conditions, the two Cu-N1 pyridine bonds are longer than the four Cu-O dione bonds, typical for a JT distorted Cu^{II} complex. However, with increasing pressure the direction of the JT axis gradually changes from the Cu-N1 bond to the Cu-O1 bond (the dione oxygen in the 3-position), becoming almost equidistant at ≈ 0.64 GPa. By 1.56 GPa the lengths of the Cu-N1 and Cu-O1 bonds steadily reduce and increase by 11 and 8% respectively. Throughout this the Cu-O2 bond length remains essentially unchanged.

Table 4.2. Changes in Cu-N and Cu-O bond lengths in FC-70

Pressure (GPa)	Cu-N1 (Å)	Cu-O1 (Å)	Cu-O2 (Å)
0.07	2.332(5)	2.022(5)	1.960(5)
0.14	2.297(6)	2.040(6)	1.972(5)
0.33	2.198(6)	2.114(6)	1.969(5)
0.88	2.057(9)	2.164(11)	1.978(9)
1.27	2.051(8)	2.200(9)	1.977(7)
1.56	2.046(8)	2.201(10)	1.966(8)

Pressure induced JT switching has been observed in other systems, including a Mn_{12} single-molecule magnet cluster that re-orientates the JT axis on one of the Mn centres at 2.5 GPa.[11] A similar transition is also observed in $[CuF_2(H_2O)_2(pyz)]$ (pyz=pyrazine), where the JT axis is reoriented from the Cu-N bond to the perpendicular Cu-O bond, though this occurs during a crystallographic phase transition at 1.8 GPa. Here, in CuPyr-I, no phase transition takes place, and unusually the JT switching appears to occur progressively on increasing pressure in FC-70, unlike other materials possessing a JT switch. [12]

In a separate high-pressure experiment, MeOH was used as a hydrostatic medium and a sample of CuPyr-I was compressed from 0.52 to 5.28 GPa. On

increasing pressure to 1.57 GPa, the *a/b* and *c*-axes compress by 3.79 % and 0.26 % respectively (see Figure 4.2 and Table 4.1 for unit cell dimensions). On increasing pressure further, the *a/b*-axes continue to be compressed, however the *c*-axis actually increases in length. Above 2.78 GPa, CuPyr-I undergoes a single-crystal to single-crystal isosymmetric phase transition to a previously unobserved phase (hereafter referred to as CuPyr-II). The data were of sufficient quality to allow the structure of CuPyr-II to be solved and refined, however above 3.34 GPa only unit cell dimensions could be extracted. The transition to CuPyr-II resultes in a doubling of the *a* and *b*-axes, while the *c*-axis increases slightly. On increasing pressure on CuPyr-II, the *c*-axis continues to increase until the sample becomes amorphous at 5.28 GPa, only unit cell dimensions are therefore reported from 3.77 to 4.90 GPa. Positive and negative linear compressibility is somewhat rare in framework structures, with previous examples including ammonium oxalate monohydrate, paracetamol, and more recently a Co-citrate framework.[24,25] Here, the *c*-axis compresses between 0.50 and 1.57 GPa by 0.26 %. NLC is observed between 2.15 and 4.90 GPa, with the *c*-axis expanding by 1.47 %. Isothermal compressibility, *K*, is defined as:

$$K = -\frac{1}{l}\left(\frac{\partial l}{\partial p}\right)_T$$

where *l* denotes the axis and *p* is hydrostatic pressure. The calculated *K* values for the regions of positive and negative compressibility give *K* values of 2.45(7) TPa^{-1} (Δp = 0.50-1.57 GPa) and -5.1(4) TPa^{-1} (Δp = 2.15-4.90 GPa) respectively.[26] The value of *K* here is rather small compared to the massive NLC behaviour observed in the low pressure phase of $Ag_3[Co(CN)_6]$ [7] (K_{NLC} = −76(9) TPa^{-1}, Δp = 0-0.19 GPa) or the flexible MOF MIL-53(Al) (K_{NLC} = −28 TPa^{-1}, Δp = 0-3 GPa) for example.[23] However it is much more comparable to the dense Zn formate MOF $[NH_4][Zn(HCOO)_3]$, by Cheetham *et al.*, which showed an NLC of -1.8(8) TPa^{-1} (Δp = 0-0.94 GPa).[27]

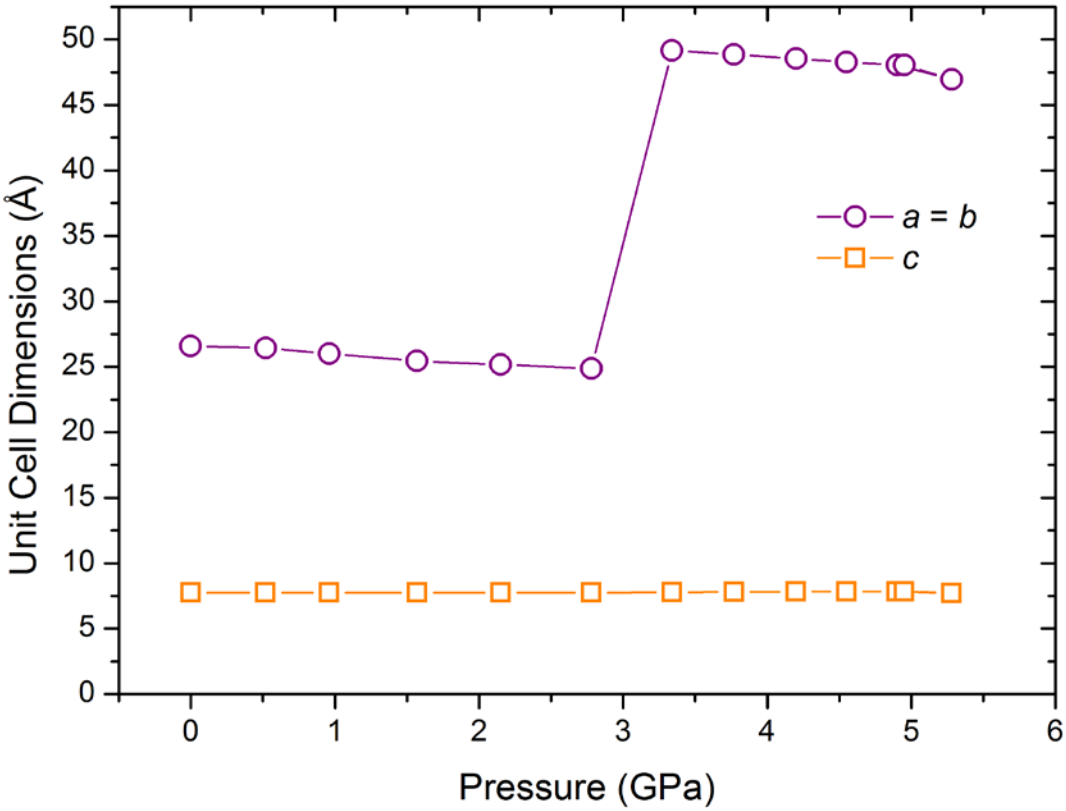

Figure 4.2. The change in unit cell dimensions with pressure in MeOH.

On increasing pressure using MeOH as a hydrostatic medium, the JT axis is again supressed (as in the FC-70 experiment) in CuPyr-I with the Cu-N1 bond reducing in length by 0.270 Å (12%) between 0.52 and 2.78 GPa, while the Cu-O1 bond length increases by 0.236 Å (12%). As a consequence, the Cu-N1 and the Cu-O1 bond lengths become equidistant at ≈ 1.47 GPa, and measure 2.055(5) Å and 2.233(6) Å respectively at 2.78 GPa. Across the entire pressure range, little to no compression or expansion is observed in the Cu-O bond in the 1-positon of the dione in either CuPyr-I or CuPyr-II. The JT switching pressure in MeOH was therefore 0.82 GPa higher (1.47 GPa) than observed by direct compression in FC-70 (0.64 GPa). These observations are indicated in both Table 4.3 and Figure 4.3.

Table 4.1. Changes in Cu-N and Cu-O bond lengths with pressure in MeOH.

Pressure	Cu-N1 (Å)	Cu-O1 (Å)	Cu-O2 (Å)
CuPyr-I			
0.00	2.332(3)	2.025(3)	1.960(3)
0.52	2.322(5)	2.007(5)	1.961(4)
0.96	2.227(6)	2.068(6)	1.966(5)
1.57	2.108(4)	2.161(4)	1.966(4)
2.15	2.073(5)	2.204(6)	1.952(5)
2.78	2.055(5)	2.233(6)	1.945(5)
CuPyr-II			
3.34	Cu1: 2.111(17)	2.147(24)	1.935(19)
3.34	Cu1: 2.108(17)	2.249(23)	1.945(20)
3.34	Cu2: 2.029(16)	2.26(18)	1.893(18)
3.34	Cu2: 2.08(15)	2.308(22)	1.838(18)

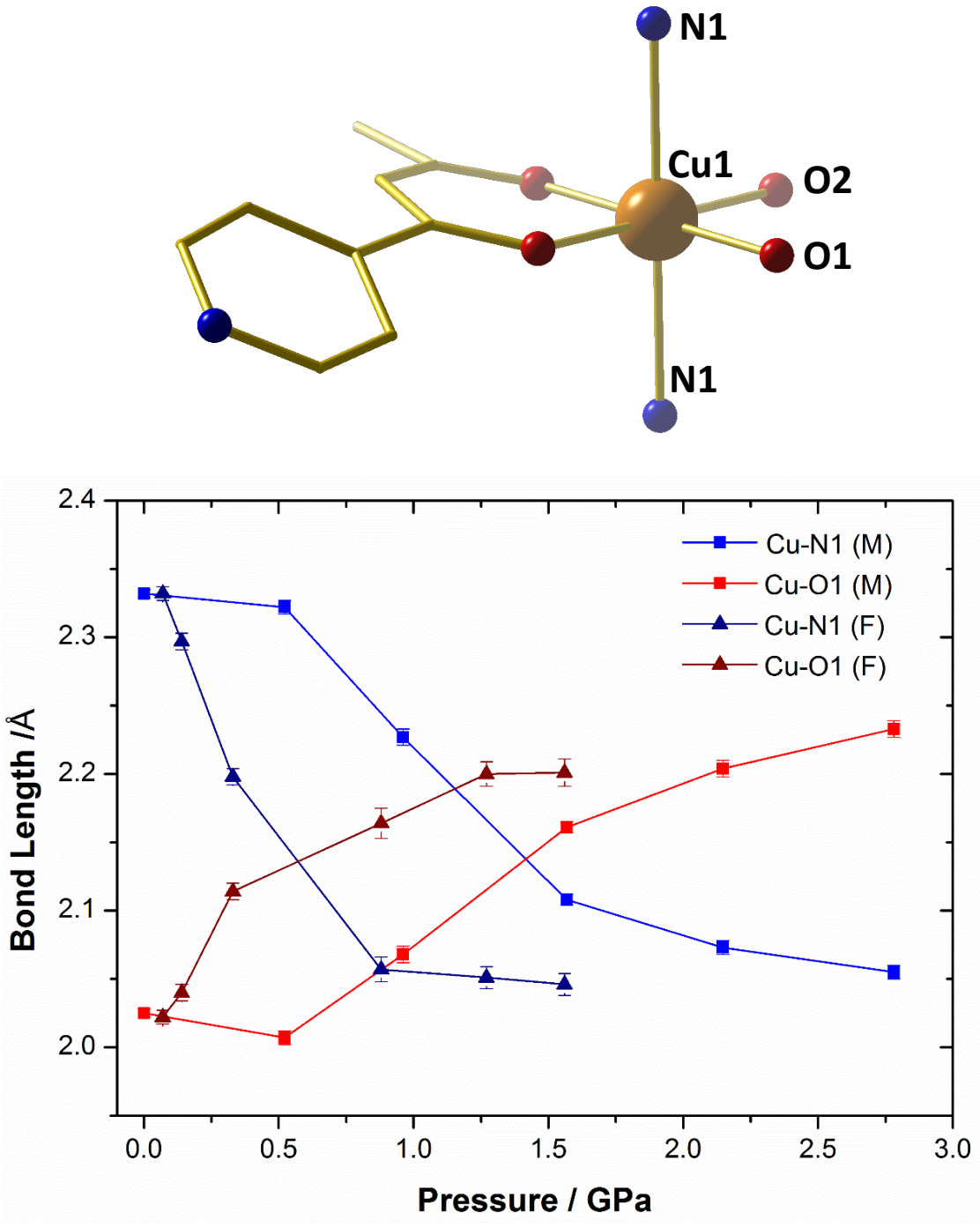

Figure 4.3. Top: Orientation of JT axis in CuPyr-I. Bottom: change in bond lengths of CuPyr-I and CuPyr-II with pressure in both MeOH and FC-70. Cu = orange, C = gold, N = blue and O = red. H-atoms omitted for clarity.

Compression of the coordination bonds is not the only distortion to take place in CuPyr-I, with the Cu-octahedra also twisting with respect to the 1-(4-pyridyl)butane-1,3-dione linkers on increasing pressure. Twisting of the Cu-octahedra

in CuPyr-I with respect to the dione section of the linker can be quantified by measuring both the N1-Cu1-O2-C4 and the N1-Cu1-O1-C2 torsion angles, which in MeOH gradually increase and decrease by 8.5° and 13.4° respectively to 2.78 GPa These changes can be seen below in Table 4.4. In FC-70, N1-Cu1-O2-C4 and N1-Cu1-O1-C2 angles increase and decrease by 1.7° and 5.1° respectively to 1.56 GPa. Compared to compression in MeOH to essentially the same pressure in FC-70 (at 1.57 GPa), this equates to a difference of approximately 5° for both angles. Twisting of the octahedra allows the compression of the channels to take place, in a 'screw' like fashion and has been observed in other porous materials with channel structures.[28] The overall effect is to reduce the pore volume, and decrease the size of the channels (see Table 4.5).

Table 4.2. Change in torsion angles with pressure in both MeOH and FC-70.

MeOH		
Pressure (GPa)	**N1-Cu1-O2-C4 Torsion (°)**	**N1-Cu1-O1-C2 Torsion (°)**
0.00	-75.87	75.99
0.52	-69.99	69.84
0.96	-69.16	67.7
1.57	-68.69	65.4
2.15	-68.53	63.77
2.78	-67.39	62.63
Total change	-8.48	13.36
FC-70		
0.07	-74.74	75.77
0.14	-75.05	74.79
0.33	-74.28	74.63
0.88	-76.08	72.25
1.27	-73.7	71.61
1.56	-73.05	70.65
Total change	-1.69	5.12

Compression of the JT axis in both MeOH and FC-70 also causes the crystals to change colour, from light green to dark red on increasing pressure (shown below

in Figure 4.4). This piezochromic behaviour is consistent with a suppression of the JT axis causing a red-shift. This to be fully reversible in both MeOH and FC-70.

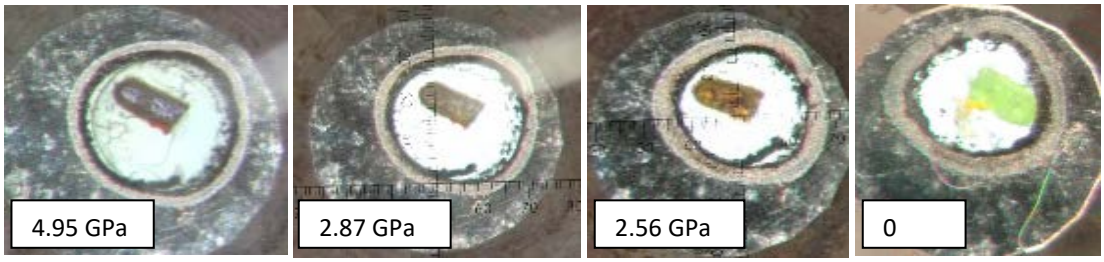

Figure 4.4. Pictures from decreasing the pressure in MeOH, showing the reversibility of the piezochromic effect.

In order to ascertain the origin of this hydrostatic media-induced change in the switching pressure and compressibility, the pore size, shape and content have been monitored as a function of pressure. The pore volume and content were calculated using the SQUEEZE algorithm within PLATON (see Table 4.5).[29] CuPyr-I has three symmetry equivalent channels per unit cell with a volume of ≈ 385 $Å^3$ under ambient pressure conditions, reducing in size to 326 $Å^3$ by 2.78 GPa, a reduction of 22.2 %. Under ambient conditions, CuPyr-I contains Et_2O trapped in the pores during the synthesis of the framework, modelled here using SQUEEZE (see experimental section).

On surrounding the crystal with FC-70, direct compression of the framework take place, with no ingress of the hydrostatic liquid into the pores. This is confirmed by the SQUEEZE output as a function of pressure, which remains almost constant until 0.88 GPa. On increasing pressure further to 1.56 GPa, an increase in the calculated electron density is observed (22% increase), though the data here are of depreciating quality and less reliable. On initially increasing pressure to 0.52 GPa, and further to 0.96 GPa using MeOH as a hydrostatic liquid, the MeOH enters the pores, resulting in an increase in electron density in the channels by 56%, and a subsequent increase in unit cell volume and therefore pore volume by 4.4% (see Table 4.5).

Previous high- pressure experiments on porous MOFs have resulted in similar behaviour on application of pressure, with the uptake of the media significantly decreasing the compressibility of the framework.[30-32] The effect of the ingress of the MeOH molecules here results in an increase in the JT switching pressure. This is to the best of our knowledge the first time compression in a different hydrostatic media has been used to control the JT switching pressure in any material. On increasing pressure above 0.96 GPa, the electron density in the pores decreases, and coincides with a steady reduction in volume of the unit cell. Both an initial increase and then subsequent decrease in uptake of hydrostatic media is common in high-pressure studies of MOFs, and has been seen several times, for example in HKUST-1 [32] and MOF-5.[30] The ingress of MeOH into the pores on initially increasing pressure to 0.52 GPa is also reflected in the twisting of the octahedra, in-particular the N1-Cu1-O2-C4 angle increases by 5.8° in MeOH, then plateaus, whereas on compression in FC-70, little to no change is observed in the N1-Cu1-O2-C4 angle to 1.56 GPa. These angles represent a twisting of the dione backbone, which we speculate must interact with the MeOH molecules which penetrate into the framework. On undergoing the transition to CuPyr-II at 3.34 GPa the unit cell volume quadruples, resulting in three symmetry independent channels (12 per unit cell), with the overall pore volume continuing to decrease (as shown in Figure 4.5- 4.6 and Table 4.5).

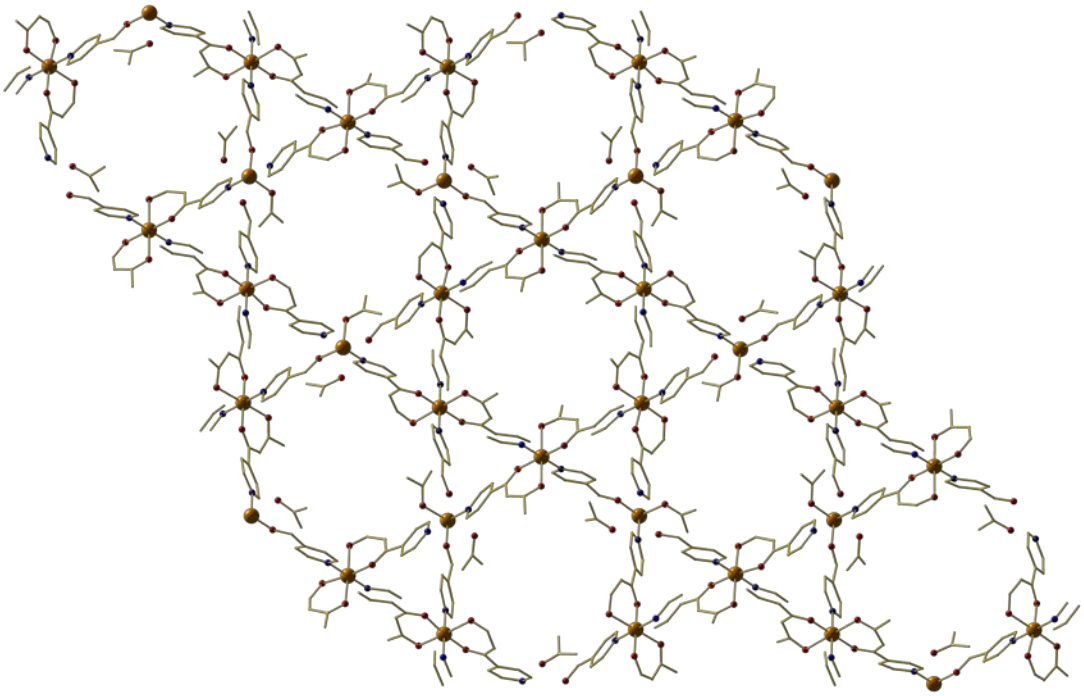

Figure 4.5. Molecular structure of one unit cell of CuPyr-II. Cu = orange, C = gold, N = blue and O = red. H-atoms omitted for clarity.

Table 4.3. Unit cell, volume and electron count data in both MeOH and FC-70.

Pressure (GPa)	Unit Cell volume	Average volume per void	Average electron count per void	%reduction in void volume	%reduction in unit cell volume
MeOH					
0.52	4696.5(8)	401.33	173.00	0.00	0.00
0.96	4537.8(8)	375.00	174.67	6.56	3.35
1.57	4335.0(6)	338.00	141.00	15.78	7.67
2.15	4246.3(6)	339.67	129.00	15.37	9.60
2.78	4161.9(6)	326.33	150.00	18.69	11.35
3.34	16310(2)	310.50	170.25	22.63	13.31
FC-70					
0.07	4725.0(2)	389	112	0.00	0.00
0.14	4680.5(2)	382	112	1.80%	0.94
0.33	4552.3(3)	357	119	8.30%	3.65
0.88	4329.46)	320	110	17.72%	8.37
1.27	4287.7(5)	315	138	19.18%	9.25
1.56	4257.4(5)	315	126	19.09%	9.89

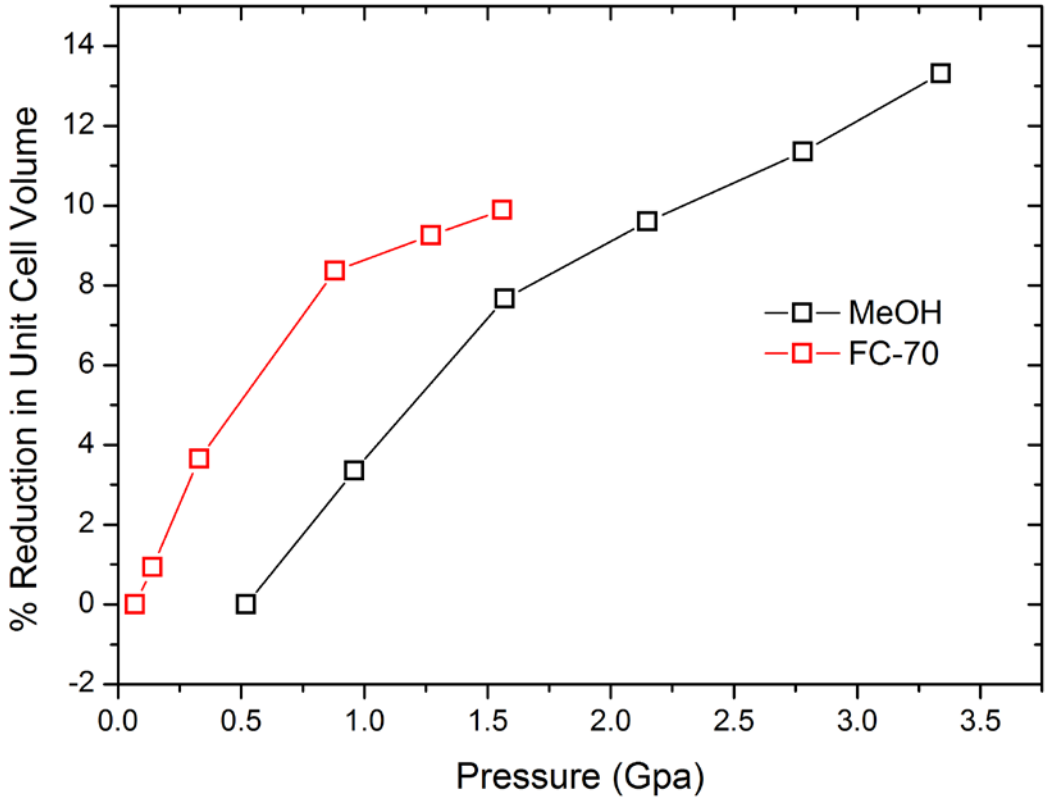

Figure 4.6. Percentage reduction in unit cell volume for both compression studies in MeOH and FC-70.

On undergoing the transition, the reflections become much broader, and as a result the data quality depreciates significantly. Nevertheless, changes in metal-ligand bond lengths can be extracted. The transition to CuPyr-II above 2.28 GPa results in two independent Cu^{II} centres (labelled Cu1 and Cu2 in Figure 4.7), with six independent Cu-N/O bond distances per Cu^{II}. Each exhibits a continuation of the trend seen in CuPyr-I, with the Cu-O bonds (equivalent to the Cu-O1 bond in CuPyr-I) remaining longer than the JT suppressed Cu-N bonds. However, the transition to CuPyr-II results in both an increase and decrease in three of the four Cu-N and Cu-O bonds respectively, compared to CuPyr-I at 2.28 GPa. The net result is a framework which contains a Cu-centre where the coordination bonds are more equidistant (Cu1), while the JT axis becomes much more prominent in the other Cu-centre (Cu2) with the Cu-O dione bond continuing to increase in length.

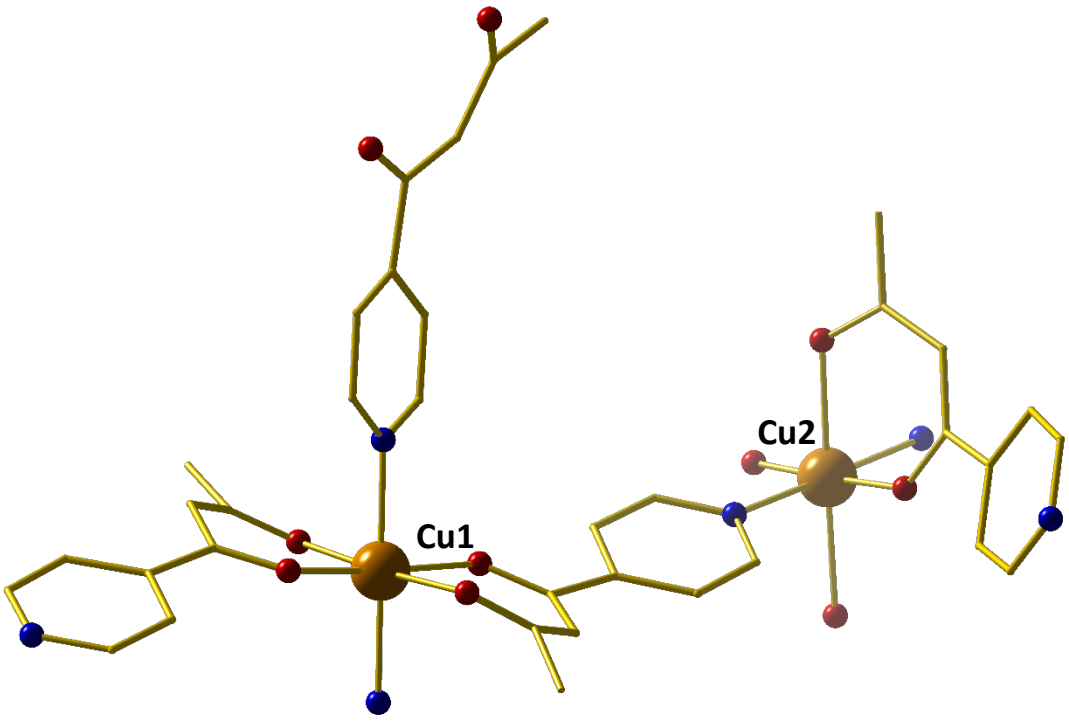

Figure 4.7. Molecular structure of CuPyr-II showing the two independent Cu^{II} centres, Cu1 and Cu2. Cu = orange, C = gold, N = blue and O = red. H-atoms omitted for clarity.

The data for CuPyr-II depreciate rapidly after the phase transition, and more work would be required to study the effect of the anisotropic compression of the JT axis in CuPyr-II on increasing pressure further. Unfortunately, because the phase transition results in a significant reduction in data quality, it is difficult to postulate the mechanism behind the NLC behaviour, as most of the NLC behaviour is observed primarily on compression of CuPyr-II. Further work will be carried out computationally in order to determine this mechanism.

4.3 Conclusion

In conclusion, we have presented a compression study on the newly synthesised Cu-based porous framework bis[1-(4-pyridyl)butane-1,3-dione]copper(II), referred to as CuPyr-I, compressing in FC-70 to 1.56 GPa and MeOH to 4.90 GPa. In both FC-70 and MeOH the JT axis, which extends along the Cu-N pyridyl bond compresses steadily and then switches to lie along one of the Cu-O dione bonds. On increasing pressure in MeOH, MeOH molecules enter the pores, causing the JT switching pressure to increase from 0.64 GPa in FC-70, to 1.47 GPa in MeOH, and a greater degree of distortion to occur within the Cu-octahedra due to the ingress of MeOH molecules into the pores. Suppression of the JT axis is also accompanied by a piezochromic based colour change in the crystals from light green to dark red, consistent with a suppression of the JT axis. On increasing pressure above 1.57 GPa, the framework undergoes an isosymmetric phase transition to a previously unobserved phase, which results in a doubling of the *a/b* axes. On increasing pressure further, NLC behaviour is observed between 2.15 and 4.90 GPa in CuPyr-II. Although each of these phenomena have been reported numerous times in a range of materials, this is to the best of our knowledge the first time a phase transition, NLC, piezochromic and pressure induced JT switching behaviour have been observed within the same material. We have also for the first time reported a JT axis switching under pressure which is hydrostatic media dependant. In further analysis of this system, we intend to study the magnetic properties under ambient and high pressure, as well as further UV/ vis analysis to confirm the piezochromic based colour change.

4.4 References

1. S. A. Moggach, S. Parsons and P. A. Wood, *Crystallogr. Rev.,* 2008, **14**, 143.
2. S. A. Moggach and S. Parsons, *Spectrosc. Prop. Inorg. Organomet. Compd.*, 2009, **40**, 324.
3. K. Ohta, Y. Kuwayama, K. Hirose, K. Shimizu and Y. Ohishi, *Nature*, 2016, **534**, 95.
4. D. Umeyama, S. Horike, S. Tassel, H. Kageyama, Y. Higo, K. Hagi, N. Ogiwara and S. Kitagawa, *APL Mater.*, 2014, **2**, 124401.
5. S. C. McKeller, J. Sotelo, J. P. S. Mowat, P. A. Wright and S. A. Moggach, *Cryst. Eng. Comm*, 2016, **18**, 1273.
6. B. F. Johnston, W. G. Marshal, S. Parsons, A. Urquhart and I. D. H Oswald, *J. Phys. Chem. B.*, 2014,**118**, 4044.
7. V. D. Kiselev, *Int. J. Chem. Kinet*, 2013, **45**, 613.
8. S. C. McKeller and S. A. Moggach, *Acta Cryst.*, 2015, **B71**, 587.
9. J. Sotelo, C. H. Woodall, D. R. Allan, E. Gregoryanz, R. T. Howie, K. V. Kamenev, M. R. Probert, P. A. Wright and S. A. Moggach, *Angew. Chem.*, *Int. Ed*., 2015, **54**, 13332.
10. A. B. Cairns and A. L. Goodwin, *Phys. Chem. Chem. Phys.*, 2015, **17**, 20449.
11. P. Parois, S. A. Moggach, J. Sanchez- Benitez, K. V. Kamenev, A. R. Lennie, J. E. Warren, E. K. Brechin, S. Parsons and M. Murrie, *Chem. Commun.*, 2010, **46**, 1881.
12. A. Prescimone, C. Morien, D. Allan, J. A. Schlueter, S. W. Tozer, J. L. Manson, S. Parsons, E. K. Brechin and S. Hill, *Angew. Chem. Int. Ed.*, 2012, **51**, 7490.
13. L. Merrill and W. A. Bassett, *Rev. Sci. Instrum.*, 1974,**45**, 290.
14. S. A. Moggach, D. R. Allan, S. Parsons and J. E. Warren, *J. Appl. Cryst.*, 2008, **41**, 249.
15. G. J. Piermarini, S. Block, J. D. Barnett and R. A. Forman, *J. Appl. Phys*., 1975, **46**, 2774.
16. SAINT v. 8.34A (Bruker AXS Inc., Madison, Wisconsin, USA, 2014)
17. SADABS v. 2008-1 ed. (Bruker AXS Inc., Madison, Wisconsin, USA, 2008).
18. A. Dawson, D. R. Allan, S. Parsons and M. Ruf, *J. Appl. Cryst*., 2004, **37**,410.
19. APEX2 v. v2014.11-0 (Bruker AXS Inc., Madison, Wisconsin, USA, 2014).
20. G. Sheldrick, *Acta Cryst.*, 2015, **A71**, 3.
21. P. W. Betteridge, J. R. Carruthers, R. I. Coopers, K. Prout and D. J. Watkin, *J. Appl. Cryst*., 2003, **36**, 1487.
22. A. U. Ortiz, A. Bourtin, A. H. Fuchs, F.-X. Voudert, *J. Phys. Chem. Lett.*, 2013, **4**, 1861.
23. T. D. Bennett, P. J. Saines, D. A. Keen, J.-C. Tan and A. K. Cheetham, *Chem. Eur. J*., 2013, **19**, 7049.

24. J. Binns, K. V. Kamenev, K. E. R. Marriott, G. J. McIntyre, S. A. Moggach, M. Murrie and S. Parsons, *Chem. Commun*., 2016, **52**, 7486.
25. Y. Qiao, K. Wang, H.Yuan, K. Yang and B. Zou, *J. Phys. Chem. Lett.,* 2015, **6**, 2755.
26. M. J. Cliffe and A. L. Goodwin, *J. Appl. Crystallogr.*, 2012, **45**, 1321.
27. W. Li, M. R. Probert, M. Kosa, T. D. Bennet, A. Thirumurugan, R. P. Burwood, M. Parinello, J. A. K. Howard and A. K. Cheetham, *J. Am. Chem. Soc*., 2012, **134**, 11940.
28. S. A. Moggach, C. H. Gorbitz and J. E. Warren, *Cryst. Eng. Comm.*, 2010,**12**, 2322.
29. A. L. Spek, *Acta Crystallogr.*, 2015, **C71**, 9.
30. A. J. Graham, D. R. Allan, A. Muszkiewicz, C. A. Morrison and S. A. Moggach, *Angew. Chem. Int. Ed*., 2011, **50**, 11138.
31. A. J. Graham, A. M. Banu, T. Duren, A. Greenaway, S. C. McKeller, J. P. S. Mowat, K. Ward, P. A. Wright and S. A. Moggach, *J. Am. Chem. Soc*., 2014,**136**¸8606**.**
32. A. J. Graham, J.-C. Tan, D. R. Allan and S. A. Moggach, *Chem. Commun*., 2012, **48**, 1535.

Chapter 5
Conclusions

Conclusions

The work in this thesis begins with a detailed study of the magneto-structural relationship between a family of newly synthesised double oxime bridged Mn^{III} dimers, whose structures differ from previous examples in the orientation of their JT axis. In previous examples the JT axis has been oriented parallel and along the bridging plane between the Mn^{III} centres which results in ferromagnetic exchange. However, the addition of a different chelating ligand has resulted in the novel synthesis of complexes **1**-**3** and **5**, in which the JT axes have switched orientation, where they lie perpendicular to the bridging plane and co-parallel to each other. This results in a weakly antiferromagnetic interaction between the Mn^{III} centres. DFT studies conducted on both types of dimers confirmed the nature and magnitude of the exchange interactions. The rationale of studying small dimeric structures is to be able to project the findings in these small and relatively magnetically simple structures onto larger structures in which it may be more difficult to understand the exchange interactions. The work here presents the opportunity not only to extend the family of related structures, by for example changing the chelating ligand in order to further confirm our findings.

Chapter 3 describes the synthesis and characterisation of a family of heterometallic Fe^{III} cages, using $[Fe^{III}L_3]$ (where HL = 1-(4-pyridyl)butane-1,3-dione) as a multifunctional metalloligand. Five $[Fe^{III}{}_8M^{II}]^{12+}$ cubes (**1**-**5**) were synthesised, where M^{II} = Cu, Co and Ni. The structures consist of $[Fe^{III}L_3]$ situated at the vertices of the cubes and the M^{II} bridging between the Fe^{III} metal centres. The second family of structures contains two heterometallic-Fe^{III} trigonal bi-pyramidal structures of general formula $[Fe^{III}{}_2M^{II}{}_3]$, where M^{II} = Co and Zn (**6** and **7** respsectively). The structural stability of all these complexes is emphasised by the ability to maintain the structural motifs in both families whilst replacing the M^{II} ion present. Magnetic studies were performed on several of the cages, however the complexity of the cubes meant that it was only possible to quantify the exchange interaction in compound **6**, which exhibits weak antiferromagnetic exchange. Magnetisation and EPR studies confirmed a D_{Co} of 11.3 cm^{-1}. The studies in this work have opened up the

construction of supramolecular magnetic cages, with potential application in other areas of chemistry. The presence of large internal cavities of the synthesised structures suggest that the cages could act as hosts to possibly magnetic or even redox active guest species that can fit in the void spaces. Another avenue for further work lies in the possibility of modifying the design of the ligand used in the preparation of the $[Fe^{III}L_3]$ precursor in order to change the size or even the geometry of the cages. This would extend the family of related structures and would also allow us to continue an in-depth study on the ability to change magnetic properties and possibility the reactivity and stability of the structures.

Chapter 4 comprises of a compression study on the newly synthesised Cu-based porous framework bis[1-4(-pyridyl)butane-1,3-dione]copper(II), referred to as CuPyr-I, compressing in FC-70 to 1.56 GPa and MeOH to 4.90 GPa. In both media the JT axes, which extends along the Cu-N pyridyl bond compresses steadily and then switches to lie along one of the Cu-O dione bonds. The compound also undergoes a phase transition upon increasing the pressure above 1.57 GPa to a previously unobserved phase in which the a/b axes are doubled. On increasing the pressure further, NLC behaviour is observed. Although these phenomena have been reported in different materials, to the best of our knowledge this is the first time that a phase transition, NLC, piezochromic and pressure induced JT switching behaviour have been observed within the same material. This newly synthesised MOF has the potential to be studied further in order to examine its magnetic properties under ambient and high pressures, for example by EPR spectroscopy. Further analysis can also be performed by UV-visible spectroscopy to confirm the piezochromic colour change.